Title
The rotation and fracture history of Europa from modeling of tidal-tectonic processes

Author
Rhoden, Alyssa Rose

Publication Date
2011

Peer reviewed|Thesis/dissertation

The rotation and fracture history of Europa from modeling of tidal-tectonic processes

By

Alyssa Rose Rhoden

A dissertation submitted in partial satisfaction

of the requirements for the degree of

Doctor of Philosophy

in

Earth and Planetary Science

in the

Graduate Division

of the

University of California, Berkeley

Committee in charge:
Dr. Michael Manga, Chair
Dr. Mark A. Richards
Dr. George Johnson

Fall 2011

(This page intentionally left blank.)

Abstract

The rotation and fracture history of Europa from modeling of tidal-tectonic processes

By

Alyssa Rose Rhoden

Doctorate of Philosophy in Earth and Planetary Science

University of California, Berkeley

Dr. Michael Manga, Chair

Europa's surface displays a complex history of tectonic activity, much of which has been linked to tidal stress caused by Europa's eccentric orbit and possibly non-synchronous rotation of the ice shell. Cycloids are arcuate features thought to have formed in response to tidal normal stress while strike-slip motion along preexisting faults has been attributed to tidal shear stress. Tectonic features thus provide constraints on the rotational parameters that govern tidal stress, and can help us develop an understanding of the tidal-tectonic processes operating on ice covered ocean moons.

In the first part of this work (Chapter 3), I test tidal models that include obliquity, fast precession, stress due to non-synchronous rotation (NSR), and physical libration by comparing how well each model reproduces observed cycloids. To do this, I have designed and implemented an automated parameter-searching algorithm that relies on a quantitative measure of fit quality to identify the best fits to observed cycloids. I apply statistical techniques to determine the tidal model best supported by the data and constrain the values of Europa's rotational parameters. Cycloids indicate a time-varying obliquity of about 1° and a physical libration in phase with the eccentricity libration, with amplitude >1°. To obtain good fits, cycloids must be translated in longitude, which implies non-synchronous rotation of the icy shell. However, stress from NSR is not well-supported, indicating that the rotation rate is slow enough that these stresses relax.

I build upon the results of cycloid modeling in the second section by applying calculations of tidal stress that include obliquity to the formation of strike-slip faults. I predict the slip directions of faults with the standard formation model - tidal walking (Chapter 5) - and with a new mechanical model I have developed, called shell tectonics (Chapter 6). The shell tectonics model incorporates linear elasticity to determine slip and stress release on faults and uses a Coulomb failure criterion. Both of these models can be used to predict the direction of net displacement along faults. Until now, the tidal walking model has been the only model that reproduces the observed global pattern of strike-slip displacement; the shell tectonics model incorporates a more physical treatment of fault mechanics and reproduces this global pattern. Both models fit the regional patterns of observed strike-slip faults better when a small obliquity is incorporated into calculations of tidal stresses.

Shell tectonics is also distinct from tidal walking in that it calculates the relative growth rates of displacements in addition to net slip direction. Examining these growth rates, I find that certain azimuths and locations develop offsets more quickly than others. Because faults with larger offsets are easier to identify, this may explain why observed faults cluster in azimuth in many regions. The growth rates also allow for a more sophisticated statistical comparison between the predictions and observations. Although the slip directions of >75% of faults are correctly predicted using shell tectonics and 1° of obliquity, a portion of these faults could be fit equally well with a random model. Examining these faults in more detail has revealed a region of Europa in which strike-slip faults likely formed through local extensional and compressional deformation rather than as a result of tidal shear stress. This approach enables a better understanding of the tectonic record, which has implications on Europa's rotation history.

Dedication

To my mother, for teaching me about atoms and encouraging me to reach for the stars;

To Richard Greenberg, for helping me find my way there;

To my sister for her enthusiasm and pride, for seeing success in me even when I don't;

And,

To my husband, for his infinite patience, partnership, and technical support

For taking on this challenge with me as though it was his own

And for loving me not in spite of what I do, but - in part - because of it

Acknowledgements

I would first like to thank my advisor and the members of my dissertation committee – Michael Manga, Mark Richards, and George Johnson – for enabling me to reach this important goal and helping me become a better scientist. I would also like to thank my collaborators: Terry Hurford, Burkhard Militzer, Eric Huff, and Gilead Wurman. These people sat beside me through some of the most frustrating and challenging moments of the projects described herein. Margie Winn, our student affairs officer, not only helped me navigate the department and University regulations but also offered me an open door and a warm smile. The support of my friends, both in and out of the department, kept me strong. Thank you for always being there to reassure me that this goal was attainable. I must also thank my family for encouraging me to pursue science, supporting me through this long process, and always being proud of my accomplishments. Lastly, I want to thank my undergraduate advisor, Richard Greenberg, for believing in my abilities and giving me the tools to successfully navigate the path I have chose. I could not have done this without all of you.

Much of this research was supported by the NASA Earth and Space Sciences Fellowship Program. Technical resources were provided by Penguin Computing.

Table of Contents

Chapter 1: Introducing Europa, a tidal-tectonic laboratory

1.1 Tidal-tectonic processes on Europa

Europa is a body of great scientific interest due to its subsurface, liquid water ocean, the abundance of tectonic features preserved on its icy lithosphere, and its participation in the only known Laplace resonance – a 2:1 mean motion resonance with neighboring satellites, Io and Ganymede. These characteristics are connected through tidal interaction. The Laplace resonance forces the orbit of Europa to remain eccentric, leading to tidal heating and stress (Greenberg, 1982). Tidal heating is thought to be the mechanism by which the ocean remains liquid (Cassen et al., 1979; Squyres et al., 1983; Ross and Schubert, 1987; Ojakangas and Stevenson, 1989a), and lineaments observed on the surface have been linked to tidal stress patterns (Hoppa et al.,1999a; McEwen, 1986; Helfenstein and Parmentier, 1983). Thus, Europa poses interconnected problems in orbital dynamics, surface processes, and interior structure - all of which have implications for Europa's habitability.

The amount of tidal heating and stress generated in a satellite depends, in large-part, on the orbit and rotation of the satellite. If Europa were not in resonance, it would have quickly been driven by tides into a circular orbit and synchronous rotation, and thus assumed a static shape in which it was elongated in the direction of Jupiter (Peale, 1999). The Laplace resonance acts to keep the satellite orbits from circularizing, forcing them to maintain eccentric orbits (Greenberg, 1982; Greenberg et al., 1998). Europa's eccentricity has been forced to a value of 0.01 by this mechanism, a much larger value than expected for a tidally despun satellite. Eccentricity causes Europa's tidally-forced shape to change throughout each orbit, resulting in friction, heating, and stress.

Because Europa's orbit is eccentric, its rotation rate is not constant throughout an orbit. Hence, its spin rate will at times be slower than the rotation rate (i.e. slower than synchronous) and at other times faster. The result is a tidal torque that continually acts to reduce or increase the spin rate to realign Europa's tidal bulge with the direction of Jupiter. Averaged over an orbit, Europa would spin slightly faster than synchronous, causing a patch of terrain to migrate eastward relative to the direction of Jupiter as the shell rotates over time (Greenberg and Weidenschilling, 1984). Hence, non-synchronous rotation could complicate the tectonic record because features observed at a given longitude on Europa may actually be a combination of features formed at many different locations relative to Jupiter. The present-day period of non-synchronous rotation is at least 12,000 yr, an observational limit set by the lack of evidence of rotation between Voyager and Galileo imagery (Hoppa et al. 1999b). If Europa's surface is slowly reoriented with respect to Jupiter, elastic stresses can build up on its surface. However, given this slow rate, the stress may viscously relax and not contribute to surface stress. Moreover, Goldreich and Mitchell (2010) conclude that, for non-synchronous rotation of the ice shell to occur, the stress induced by rotation must be limited to small values.

Lineaments composed of linked arcuate segments, called cycloids, are thought to form in response to tidal normal stress in the following way. When the tidal stress increases beyond the tensile strength of Europa's ice shell, a crack forms perpendicular to the direction of maximum tension. Then, as Europa continues to move through its orbit, the magnitude and direction of the maximum tensile stress slowly change causing the crack to propagate along a curved path. Eventually, the stress is too low for further

cracking to occur, and the crack remains dormant until the tensile stress again becomes sufficient to cause fracturing. Over the time period that the crack is dormant, the direction of maximum tension changes; when the crack resumes its propagation, it creates a cusp, the last step in the formation process. This cycle repeats throughout each orbit creating the characteristic linked arcs observed on Europa. Hence, the initial cycloidal crack is assumed to form at a rate of one arc per orbit. Flanking ridges, which are observed along many cycloids, are thought to form by a subsequent process that can take between 10 and 10^4 years to develop depending on the assumed formation mechanism (Kattenhorn and Hurford, 2007).

Previous modeling projects have been increasingly successful at fitting observed cycloids by including stress due to Europa's forced eccentricity and a small amount of non-synchronous rotation. In fact, cycloid modeling has produced the most compelling evidence for non-synchronous rotation of Europa (Hoppa et al, 2001). Unfortunately, early models only fit the general trend of the cycloids (Hoppa et al., 1999a; Hoppa et al, 2001), and more recent ones required many additional free parameters to improve fits and still could not reproduce equatorial cycloids.

Strike-slip motion along preexisting faults has been attributed to tidal shear stress (Tufts et al. 1999; Hoppa et al., 2000; Kattenhorn, 2002; Sarid et al., 2002; Rhoden et al, 2011) through a tidal-tectonic model called tidal walking (Hoppa et al., 1999, 2000). Throughout an orbit, the tidal stress at a crack cycles through periods of tension and compression and between left-lateral and right-lateral shear stress. The crack is presumed to be open when in tension, allowing displacement along the crack. When the crack is closed, friction restricts or even prohibits sliding. The result is a net displacement in the direction of simple shear at the end of the opening phase. Based on this model, the net sense of slip (right or left lateral) along a crack can be predicted if the latitude, longitude, and azimuth of the crack are known. The global pattern of strike-slip motion produced by eccentricity-driven tides has the following characteristics (Hoppa et al., 1999, 2000): only left lateral faults form above 35°N, only right lateral faults form below 35°S, and between these regions, both right and left lateral faults form with the sense of slip depending on the longitude and the azimuth of the crack. A limited survey of strike-slip faults on Europa showed that faults do tend to follow the pattern predicted by the tidal walking model (Hoppa et al., 2000). In cases where predictions did not match observations, longitudinal translation could often alleviate the mismatch.

Sarid et al. (2002) conducted a comprehensive mapping survey of strike-slip faults in five regions of Europa and identified almost 200 strike-slip faults. Comparison with the global pattern expected from the tidal walking model revealed that the region of mixed right and left lateral faults was too far north in one hemisphere and too far south in the other hemisphere. This observation led to the conclusion that polar wander of ~30° had occurred in Europa's recent geologic past. Because polar wander would generate very large stresses – and we find no evidence of faulting in response to polar wander – it must have occurred slowly enough for the stresses to relax. The polar wander interpretation, while plausible, is difficult to reconcile with observations of cycloids, which do not appear to require latitudinal shifts. Also, the hemispheric differences in strike-slip population have persisted despite the presumed non-synchronous rotation. That implies the rate of strike-slip fault formation and the rate of polar wander must be short compared to the timescale of non-synchronous rotation. This too is difficult to reconcile

with cycloids, even the most recent of which require substantial longitude migration. These complications suggest that a more in-depth study of tidal-tectonic processes is required to fully assess the rotation and fracture history of Europa.

The overarching goals of this work are to (1) better understand Europa's rotation state and the influence of rotational dynamics on tidal stress, (2) unravel the fracture history of Europa's surface to inform both studies of fracture formation and Europa's rotation history, and (3) investigate the process of tidally-driven fracture formation in an elastic shell. Europa's rotation state has implications on tidal heating, and thus, the structure of its interior. This work also has broader implications as it provides a tool for examining tidal-tectonic processes on other icy ocean worlds. For example, tides caused by Enceladus' eccentricity and close proximity to Saturn have been linked to the motion and eruption timing along the tiger stripe fractures near the south pole (Hurford et al., 2007b; Nimmo et al., 2007; Smith-Konter and Pappalardo, 2008). The tiger stripes are sources of the volatile-rich plume that replenished the e-ring (Porco et al., 2007). Understanding tidal-tectonic processes on Europa provides a framework for studying Enceladus. Additional targets for further study include other outer planet satellites such as Dione, Triton, and Miranda, and the dwarf planet Pluto, as all are thought to have ice-covered oceans (Hussman et al., 2006).

1.2 Avenues for further study

1.2.1 Investigating the effects of a more complex rotation state

An important consideration is whether eccentricity alone contributes to the formation of tidally-driven fractures. Non-synchronous rotation is expected to occur, but because its role in generating tidal stress may be limited, it cannot fully alleviate the disparities between predictions and observation. Europa's obliquity should be driven toward zero by tidal dissipation (e.g. Peale 1999). However, gravitational interaction among Jupiter's largest satellites can force the obliquity of Europa to be ~0.1° if Europa acts as a solid body (Bills 2005). The obliquity could be many times larger if the surface is mechanically decoupled from the interior (Bills et al. 2009), as expected from several lines of evidence that indicate a global ocean underlying Europa's icy shell (Anderson et al. 1998; Carr et al. 1998; Kivelson et al. 2000; Hoppa et al. 1999a). The magnitude of the obliquity is expected to change on timescales of $10\text{-}10^3$ yr, with larger variations for a decoupled ice shell (Bills et al. 2009). The direction of the spin pole can change by 0.2°/day to more than 2°/day depending again on Europa's internal structure (Bills 2005; Bills et al. 2009). Therefore, changes in the value of the obliquity could potentially be captured in the paths of cycloids that formed at different times. The precessing spin pole could even alter the paths of individual cycloids if each arc is subjected to a slightly different value.

Obliquity causes the latitude of the tidal bulges to vary throughout each Europan day, which would alter the pattern of Europa's time-varying tidal stress, thus influencing the formation of tidally-driven cracks (Bills 2005; Bills et al. 2009; Hurford et al. 2009a). In addition, even an obliquity as small as 0.1° could generate a significant fraction of Europa's tidal heat (Tyler 2008), which may contribute to the long-term stability of the ocean. Despite its potential importance, there are few observational constraints on

Europa's obliquity. Theoretical arguments (e.g. Bills 2005) only provide a lower bound (0.1°). There is no upper bound, but the lack of signal in the gravity measurements requires that Europa's obliquity is small (Anderson et al. 1998).

Gravitational torque from Jupiter on the oblate shape of Europa forces a physical libration in addition to the longitudinal libration of the tidal bulges caused by Europa's eccentricity. As with obliquity, the physical libration is typically damped such that its effects are negligible (Peale 1977). However, Bills et al. (2009) has shown that, if Europa acts as a solid body, physical libration would cause a reference point such as the sub-Jupiter point to undergo longitudinal displacement of ~133 m at the equator, which corresponds to a libration amplitude of 0.005°. The presence of an ocean could increase this value by a factor of 10^3, although the amplification is likely restricted by gravitational coupling between the shell and the interior (see also, Van Hoolst et al. 2008). We have been unable to identify any observational constraints on Europa's libration in the literature. Physical libration would modulate the longitudinal motion of the tidal bulge induced by eccentricity, and could thus alter the pattern of tidal stress on the surface.

Hurford et al. (2009a) investigated the effects of obliquity on the global pattern of cycloids because the eccentricity-only model fails to reproduce two important characteristics of observed cycloids. First, a tidal model that incorporates only eccentricity predicts that two regions of boxy cycloids would form on the equator in opposite hemispheres. Although two regions of boxy cycloids are observed, they are offset from the equator – one is too far north, and the other is too far south, but the discrepancy is opposite the offsets in the global strike-slip fault pattern as described by Sarid et al. (2002). The second characteristic that cannot be explained by an eccentricity-only model is the existence of regular cycloids that cross the equator. Hurford et al. (2009a) found that, for certain spin pole directions, an obliquity of 0.1° would result in an offset of each boxy region by an amount and in a direction that is consistent with the observations and, in addition, could generate equator-crossing cycloids consistent with those observed. These results strongly suggest that Europa's obliquity is large enough to affect cycloid formation.

In the first part of this work, I investigate how obliquity, spin pole precession, and physical libration alter the tidal stress field (Chapter 2). I then test tidal models that include these parameters (along with stress and migration due to NSR) by comparing how well each model reproduces observed cycloids. I have designed and implemented an automated parameter-searching algorithm that relies on a quantitative measure of fit quality to identify the best fits to observed cycloids. I rely on statistical techniques to determine the tidal model best supported by the data and constrain the values of Europa's rotational parameters. The methodology and results are detailed in Chapter 3. In Chapter 4, I calculate the effect of Io-raised tides on Europa, which has been neglected in previous work. I then assess the importance of Io-raised tides on the formation of cycloids.

As with cycloids, the stress field used to predict the slip directions along pre-existing faults incorporates only the tidal effects of Europa's forced eccentricity. Obliquity and physical libration would likely influence the displacement along individual faults and the global pattern of fault formation. For example, obliquity breaks the symmetry in tidal stress across the sub-Jupiter point, which could account for the

observed regional differences in the fault patterns. A tidal model that includes obliquity could potentially reconcile predictions of strike direction with observations without requiring large translations in latitude. I examine this possibility, as described in Chapter 5, by generating predictions of slip direction with different tidal models using the tidal walking framework. I first create global predictions to compare against the observed global pattern and then make predictions at the locations and azimuths of individual cycloids.

1.2.2 Investigating the formation of strike-slip faults

Even without more complex rotational dynamics, the tidal walking model for strike-slip formation reproduces the basic pattern of observed strike-slip faults on Europa (Hoppa et al., 1999; 2000; Sarid et al., 2002). As described in Chapter 5, adding the effects of obliquity improves the predictive power of the model. However, the mechanics of tidal walking are oversimplified. Neither stress release due to cracking nor stress relaxation with time is explicitly included, and predictions of slip direction are based solely on the sign of the shear stress when the normal stress becomes compressive. Furthermore, failure is only allowed when the fault is experiencing tensile normal stress, so the model is only applicable in the upper tens of meters of Europa's surface. Deeper within the shell, the compressive overburden stress would exceed the tidal stress and clamp the fault throughout the entire orbit.

A different tidal-tectonic formation model was proposed by Smith-Konter and Pappalardo (2008) for hypothesized strike-slip motion along the Tiger Stripe fractures on Enceladus (henceforth, the SKP model) and should be equally applicable to Europa. Although more quantitative and mechanically-based than the tidal walking model, the SKP model may not be applicable to the ice shells of Europa and Enceladus. Europa's ice shell acts elastically over short timescales, so the shell will impose a restoring force on the fault that will act to reduce slip on the fault if the shear stress that produced the slip decreases. One way to visualize this process is to think of the fault as a boundary between Earth-like plates that are connected in the far field by a spring rather than two plates that move independently. The effect of the elastic restoring force is neglected in the SKP model but included in the tidal walking model. However, the tidal walking model lacks quantitative analysis of stress and slip on faults and cannot be applied to faults at depth.

To better understand the mechanics of strike-slip faulting on Europa, I first develop a mechanical model that relies on quantitative analysis of stress and slip, includes a more realistic treatment of fault mechanics, and incorporates the elastic restoring force imposed by Europa's ice shell by reducing shear stress on the fault to zero when the fault slips. I then use the global pattern of strike-slip faults to test formation models with and without the elastic shell response: the shell tectonics model and a model based on Smith-Konter and Pappalardo (2008), respectively. Finally, incorporating obliquity and using the shell tectonics model, I assess several characteristics of the observed fault population. This work is described in Chapter 6.

1.3 Summary of main results

In Chapter 7, I synthesize the results of these studies. Both cycloids and strike-slip

faults indicate that Europa's spin pole is tilted ~1° and likely varies in magnitude and direction over geologically short timescales. In addition, Europa likely undergoes a physical libration that is in-phase with the eccentricity libration. Although stress from non-synchronous rotation is not well-supported by cycloid modeling, longitude migration is required to achieve good fits to cycloids and to reproduce the entire population of observed strike-slip faults. Polar wander is no longer required to explain the hemispheric differences in strike-slip fault populations when obliquity is included in the tidal stress calculations. Tidal stresses induced by Io are large enough to slightly alter the paths of cycloids in some regions but do not improve fits to individual observed cycloids.

The shell tectonics model is better at reproducing the observed fault populations than a model based on Smith-Konter and Pappalardo (2007), supporting the hypothesis that the assumptions of fault slip in the shell tectonics model are more applicable to Europa than those in the SKP model. The shell tectonics and tidal walking models make the same assumptions about fault slip direction, so both models can reproduce the observed global pattern of strike-slip faults especially when a small obliquity is incorporated into calculations of tidal stress. However, the shell tectonics model predicts the slip directions of more faults at their current locations than the tidal walking model. The shell tectonics model allows faults to slip whenever the CFC is met, whereas the tidal walking model requires faults to be in net tension to slip. The shell tectonics model predicts the slip directions along preexisting faults as well as the relative rates of slip accumulation for faults of different azimuths. Using this additional information, we find that the shell tectonics model can explain azimuth clustering in the strike-slip record, and has helped identify an interesting tectonic region in which strike-slip is formed through regional extension and compression rather than tidal shear stress.

Chapter 2: Calculating tidal stress, a primer

2.1 Calculating tidal stress with complex rotational dynamics

If Europa maintained a circular orbit, had zero obliquity, and rotated synchronously, the tidal bulges raised by Jupiter would be located on the equator and at the same longitude throughout each orbit (Peale 1999). Over time, Europa would permanently adopt the shape governed by this primary tide. Because Europa's orbit is eccentric, however, the distance and location of Jupiter varies with respect to Europa. This causes Europa's tidal shape to deviate from the primary tidal figure in both magnitude and direction, which generates stress on Europa's surface (Greenberg et al. 1998). Similarly, obliquity and non-synchronous rotation act to reorient Europa's tidal bulges away from the primary tidal shape. The total tidal stress field imposed on Europa's surface is the combination of the primary tide, eccentricity-driven tide, obliquity-driven tide, and stress induced by non-synchronous rotation.

To calculate the each tidal stress contribution, we assume a thin, elastic, outer shell that is mechanically decoupled from the interior. This outer layer conforms to fit the tidally-controlled shape of Europa's interior. The surface stress generated by the primary tide is given by (e.g., Melosh 1977; Melosh, 1980)

$$\text{(2.1a)} \quad \sigma_\delta = C\,(5 + 3\cos 2\delta_P)$$
$$\text{(2.1b)} \quad \sigma_\alpha = -C\,(1 - 9\cos 2\delta_P)$$

where $C = 3h_2 M\mu(1 + \nu)/ 8\pi\rho a^3(5 + \nu)$ and h_2 is the tidal Love number, M is Jupiter's mass, μ is the shear modulus, ν is Poisson's ratio, ρ is the average density, a is the distance between Jupiter and Europa, and δ_P is the angular distance from a point on Europa's surface to the primary tidal bulge. The σ_δ stress is directed radially from the tidal bulges and the σ_α stress is perpendicular to the σ_δ stress. Since all the stress calculations contain a factor of C, its value does not influence the results presented in the following chapters.

Europa's eccentricity causes the tidal bulges to libration in longitude; obliquity predominantly causes a latitudinal libration. Spherical trigonometry is used to calculate the varying location of the tidal bulge, which depends on the spin pole direction (SPD) and the true anomaly. Since the locations of the tidal bulges are changing, the angular distance to the bulge, δ, also changes. The tidal stress equations can thus be modified to account for the eccentricity and obliquity (see also Hurford et al. 2009a).

$$\text{(2.2a)} \quad \sigma_\delta = C\,(1 - e\cos n)^{-3}\,(5 + 3\cos 2\delta)$$
$$\text{(2.2b)} \quad \sigma_\alpha = -C\,(1 - e\cos n)^{-3}\,(1 - 9\cos 2\delta)$$

where e is eccentricity, ε is obliquity, φ is the SPD, and n is the true anomaly (Fig. 2.1). When Europa is at pericenter, if the spin pole is pointing toward Jupiter, the SPD is defined as 90°; SPD increases clockwise. The value of δ depends on the bulge colatitude, λ, and the bulge longitude, ω, as follows:

(2.3a) $\lambda = \pi/2 - \varepsilon \sin(n + \varphi)$
(2.3b) $\omega = -2e \sin n$

Physical libration is caused by Europa's oblateness and affects tidal stresses. Whereas eccentricity causes the tidal bulges to move relative to a reference location such as the sub-Jupiter point, physical libration is the physical oscillation of that reference point (Hurford et al., 2009b). It is characterized by an amplitude, α, and a phase, ϕ. A libration phase of 0° indicates that the reference line is tracking the tidal bulge while a phase of 180° means the reference line is moving in the opposite direction of the tidal bulge. Libration thus enters the tidal stress equations in the calculation of the bulge longitude, ω. Equation 2.3b becomes:

(2.4) $\omega = -2e \sin(n) + \alpha \sin(n + \phi)$

At a given instance in time, the precession rate does not enter into the tidal stress equations. However, to model cycloids and strike-slip faults, we calculate the tidal stress at successive time steps. To incorporate precession, we increase the spin pole direction at each time step by an amount determined by the precession rate.

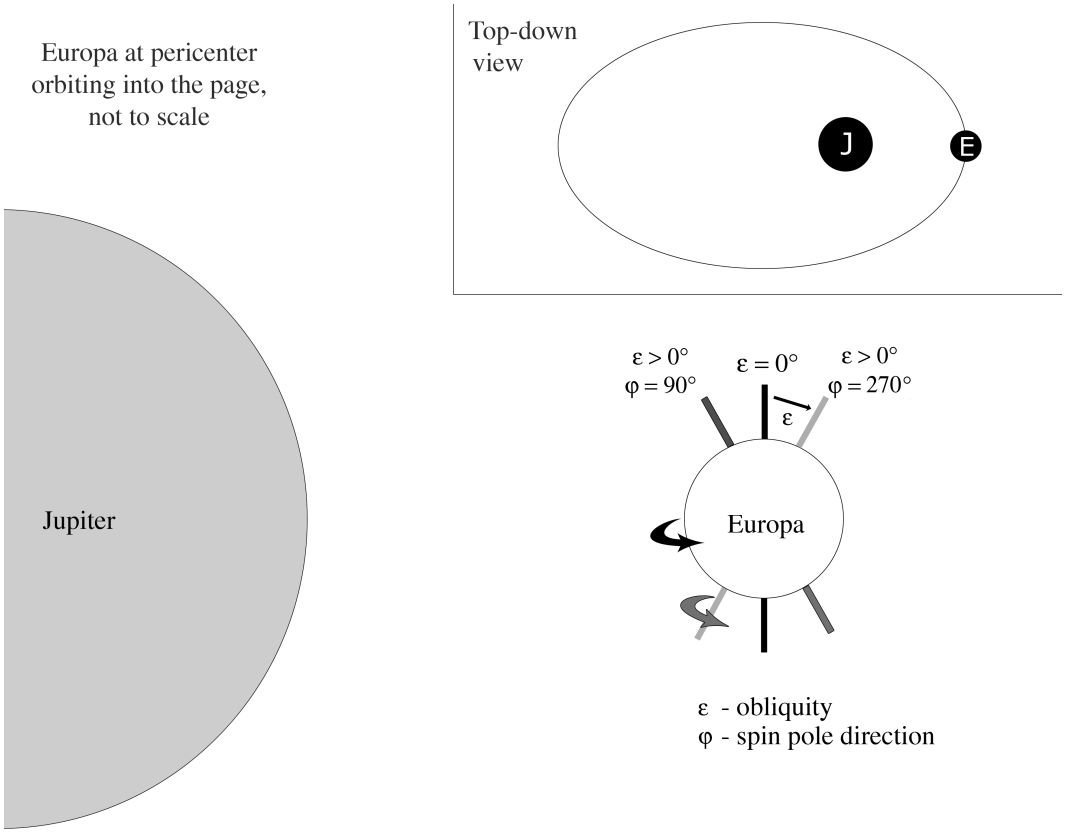

Figure 2.1: A schematic illustrating obliquity and spin pole direction. An SPD of 0° means that the spin pole is pointing out of the page, opposite Europa's orbit direction, at pericenter. Whereas, at 90°, the spin pole is pointing toward Jupiter, as shown. The SPD increases clockwise.

Europa may rotate slightly faster than synchronous in order to balance tidal torques (Greenberg and Weidenschilling 1984). In that case, Europa's surface will slowly migrate in longitude with respect to the direction of Jupiter, carrying the tidal bulges out alignment with Jupiter. We can approximate the stress caused by non-synchronous rotation in terms of the number of degrees of rotation that Europa undergoes before stress generated by non-synchronous rotation relaxes. Stress from NSR is calculated by taking the difference between stresses generated with the old bulge location and those generated with the bulge rotated a number of degrees away (i.e. using Eq. 2.1a,b with different values of δ_P).

Equations 2.2a and 2.2b give the total tidal stress due to eccentricity and obliquity (using Eq. 2.3) and physical libration (using Eq. 2.4). To isolate the diurnal tide, we rotate the total tidal stress and the primary tidal stress (Eq. 2.1a,b) to a common coordinate system and subtract out the primary tidal stress. When applicable, the diurnal stress can then be combined with the non-synchronous stress. In the new coordinate system, the diurnal stress has two normal stress components and a shear stress component. For cycloid modeling, the diurnal stresses are decomposed into principal stresses. With strike-slip faults, the diurnal tidal stresses are decomposed into normal (σ) and shear (τ) components relative to a fault's orientation, where ζ is the azimuth of the crack measured clockwise from north.

$$\text{(2.4a)} \quad \sigma = 0.5\,(\sigma_{\delta*} + \sigma_{\alpha*}) + 0.5\,(\sigma_{\delta*} - \sigma_{\alpha*})\cos(2\zeta) + \sigma_{\delta\alpha}\sin(2\zeta)$$

$$\text{(2.4b)} \quad \tau = -0.5\,(\sigma_{\delta*} - \sigma_{\alpha*})\sin(2\zeta) + \sigma_{\delta\alpha}\cos(2\zeta)$$

2.2 Visualizing the diurnal stress field

The first column of Figure 2.2 shows contours plots of the maximum tensile stress from the diurnal tide, generated by eccentricity only, at four times in Europa's orbit. Note that tension is positive in these plots. At pericenter (t = 0), Europa is at its closest point to Jupiter, so the diurnal tidal amplitude is at a maximum and is aligned with the primary bulge direction. The net result is an enhancement of the primary tidal deformation: tension at the sub- and anti-Jupiter points (longitude 0° and 180°, respectively) and compression in a ring 90° away. As Europa continues its orbit, the magnitude of the eccentricity tide decreases but its direction moves out of alignment with the primary tidal bulge so it is not completely canceled out when the primary bulge is subtracted. The resultant diurnal bulge is offset from the sub-Jupiter point leading to a concentration of tension at the bulge longitude and compression 90° away, as shown in the panel marked $t = \pi/2$. A similar pattern emerges at $t = 3\pi/2$ in which the offset is the opposite direction. At apocenter, Europa is farther from Jupiter than average, so the eccentricity tide is smaller than the primary tide with which it aligns. The diurnal stress at $t = \pi$ thus becomes inverted with compression at the sub- and anti-Jupiter points and tension in a band 90° away.

The influence of obliquity on the diurnal stress field depends on the spin pole direction (SPD) because it controls when in Europa's orbit Jupiter will cross Europa's equator into the northern or southern hemispheres. An SPD of 90° indicates that the pole

is pointing toward Jupiter when Europa is at pericenter (see Fig. 2.1 for a schematic), and spin pole direction increases clockwise. Hurford et al. (2009a) represented the same phenomenon with a variable called argument of pericenter, ω, which is equal to the SPD. With an SPD of 0°, the obliquity-driven bulge is on the equator at pericenter and apocenter at which times the eccentricity-driven bulge is at the sub-Jupiter point. Thus, at $t = 0$ and $t = \pi$ in column 2 of Figure 2.2, the diurnal stresses are the same as in the eccentricity-only case. At $t = \pi/2$ and $t = 3\pi/2$, however, the stress pattern is skewed because the obliquity bulge is now off of the equator. When the SPD = 90°, the obliquity tide is at a maximum in magnitude and distance from the equator at t = 0. When combined with the effects of eccentricity, the result is still tension at the sub- and anti-Jupiter points but now the stresses are offset in latitude: north of the equator at longitude 0° and south at longitude 180°. At $t = \pi/2$ and $t = 3\pi/2$, obliquity does not cause an offset of the bulge latitude so the stress field is no different from the eccentricity-only case. At $t = \pi$, the diurnal stress is inverted and offset yielding compressive stress concentrations north of the equator at longitude 0° and south of the equator at longitude 180°.

Physical libration can reduce or enhance the effective longitudinal separation between the primary and eccentricity-driven tidal bulges depending on the libration phase. As shown in column 4 of Figure 2.2, for a phase of 0°, physical libration has no effect at $t = 0$ or $t = \pi$. However, at $t = \pi/2$ and $t = 3\pi/2$, the libration reduces the longitudinal separation between the bulges so the diurnal stress exhibits the same pattern as the eccentricity-only case (column 1), but with much lower magnitudes. When the libration phase is 90° (column 5), the libration is out of phase with the longitudinal motion of the eccentricity-driven bulge. At $t = 0$, the physical libration determines the location of the bulge, and the resulting diurnal stress pattern is thus offset from the sub-Jupiter point. At $t = \pi/2$ and $t = 3\pi/2$, the libration does not alter the location of the eccentricity-driven bulge, so the stress is the same as in the eccentricity-only case. When both obliquity and physical libration are non-zero, even more complex patterns arise as the components interfere. Contour plots for these cases are shown in Figure 2.3.

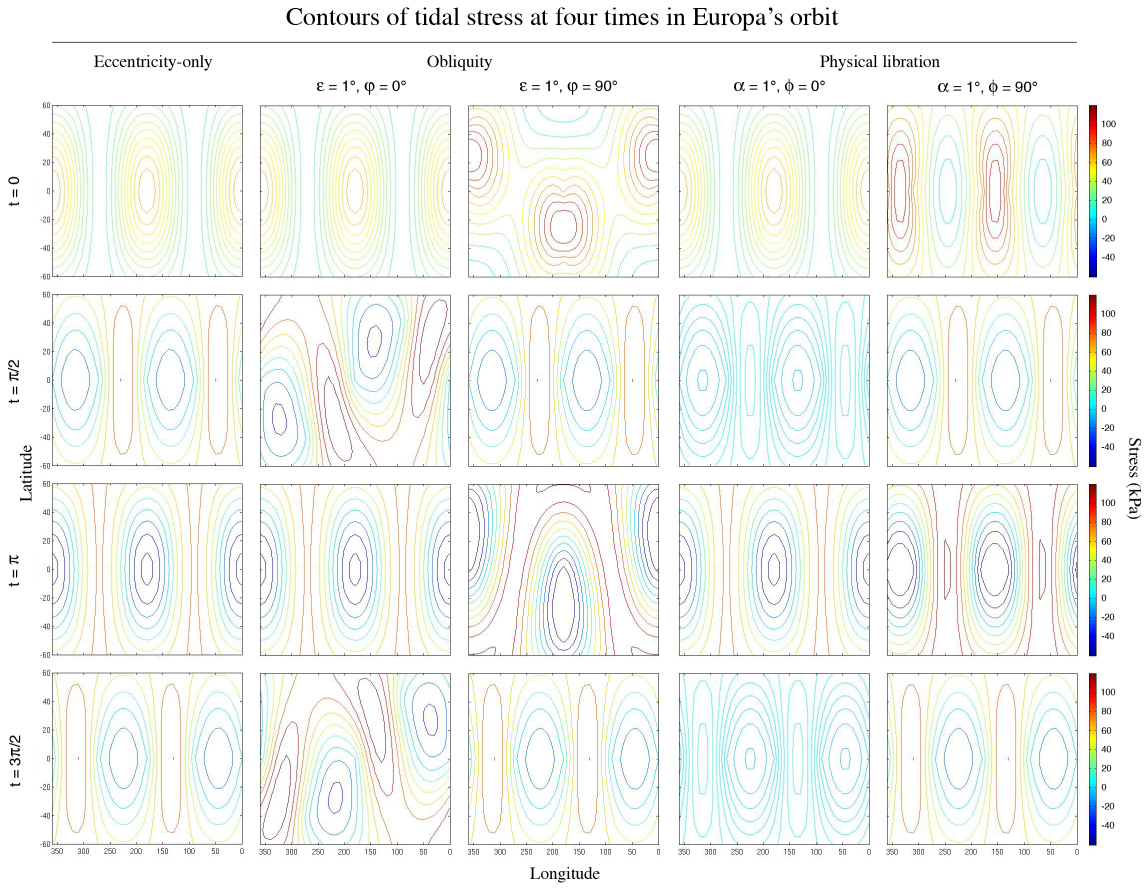

Figure 2.2: Contour plots of the maximum tensile stress magnitudes using various tidal models (columns) to show the influence of obliquity and physical libration on the diurnal tidal stress field at four times during the orbit (rows).

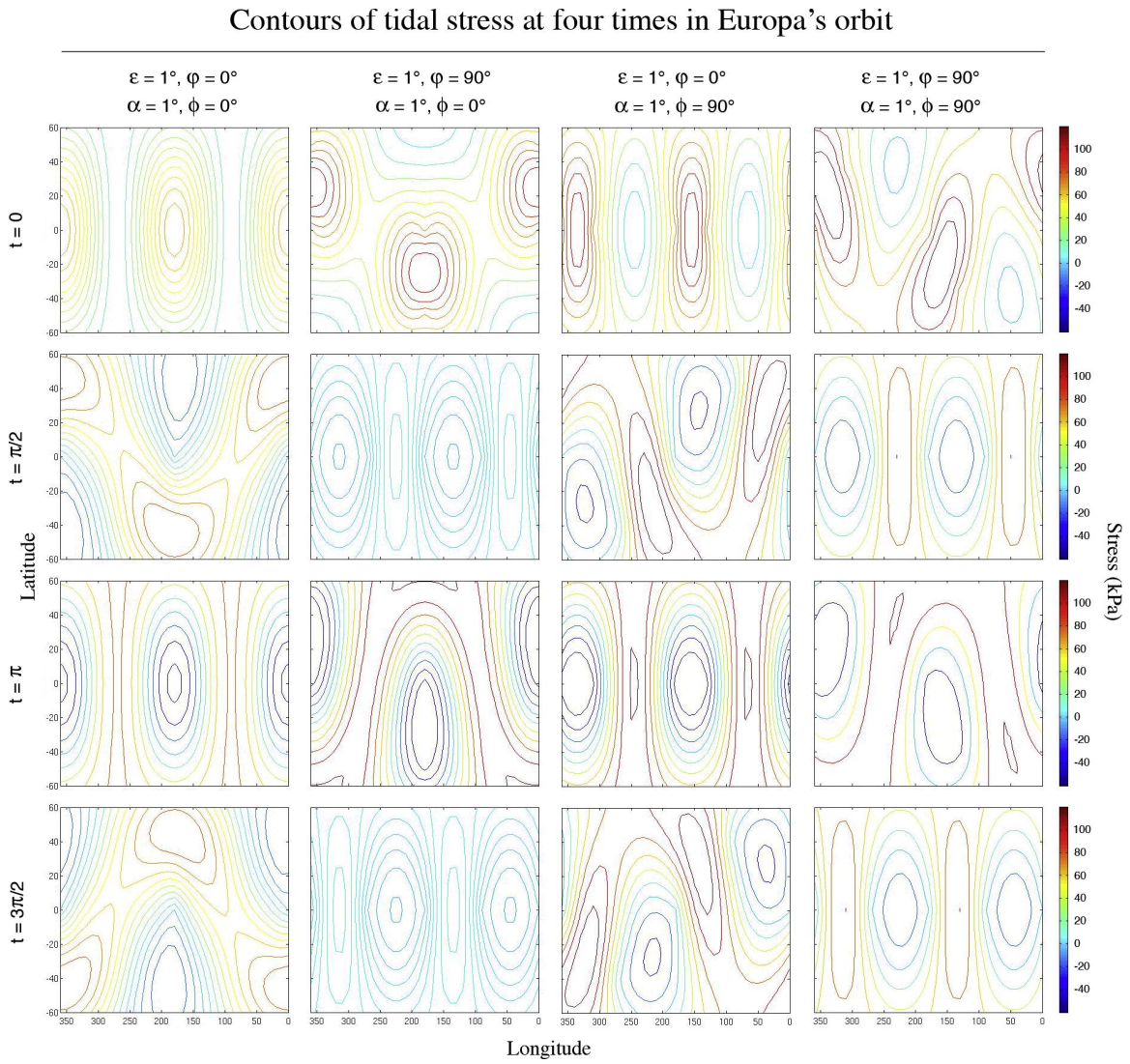

Figure 2.3: Contour plots of the maximum tensile stress magnitudes using tidal models with varying amounts of obliquity and physical libration (columns) to show the combined effects on the diurnal tidal stress field at four times during the orbit (rows).

Chapter 3: Constraining Europa's rotation state using cycloids

3.1 Introduction

Cycloids are chains of arcs, with each arc linked by a cusp, often flanked by paired ridges (Fig. 3.1). It has been proposed that they form as tensile cracks propagating in response to diurnally-varying tidal stress on Europa (Hoppa et al. 1999a; Hoppa et al. 2001; Hurford et al. 2007a; Marshall and Kattenhorn 2005), thus recording the stress changes that occurred during their formation. A physical model based on this hypothesis has been developed (Hoppa et al. 1999a; Hoppa et al. 2001). First, the tidally-induced tension in a region must increase enough to initiate tensile failure in the ice shell, forming a crack perpendicular to the direction of maximum tension. As Europa orbits Jupiter, the magnitude and direction of the stress field change causing the crack to propagate along a curved path, following the maximum tension. Later, the magnitude of the stress at the crack tip drops below the failure threshold for propagation, completing one arc. The crack then remains dormant as the stress field continues to change. When the stress at the crack tip increases above the initiation threshold, failure reinitiates, although the propagation direction has changed, resulting in a cusp. Subsequently, one of several proposed processes (e.g. Greenberg et al. 1998; Head et al. 1999; Nimmo and Gaidos 2002) creates ridges adjacent to the crack, perhaps reflecting many cycles of opening and closing along the crack. If cycloids do form in response to tidal stress, we may be able to extract from their shapes information about the rotational dynamics of Europa that contribute to tidal stress.

We test different tidal models by comparing their proficiency at reproducing observed cycloids. This process allows us to identify relevant rotational parameters, including ones neglected in previous work, and constrain both the dynamical and mechanical parameters that govern cycloid formation. Specifically, we seek to determine whether obliquity, fast precession, stress or longitude migration due to non-synchronous rotation, and/or physical libration are indicated by cycloid shapes, and if so estimate their values (see section 1.2.1 for the motivation behind investigating these particular parameters). In addition, the mechanical parameter values indicated by our cycloid fits may offer some insight as to the physical process of cycloid formation.

With each of the tidal models we investigate, we adjust parameters to identify the best fits to three cycloids in the southern hemisphere and three equatorial cycloids. To accomplish this, we first augment the tidal stress equations to include the dynamical parameters of interest and then apply numerical techniques, which rely on a quantitative measure of fit quality, to identify the parameter sets that best fit the observed cycloids. Incorporating only obliquity and using our systematic and quantitative approach (described in Section 3.3), we find better fits to southern hemisphere cycloids, in some cases with far fewer free parameters, than in previous work that neglected obliquity (Hoppa et al. 2001; Hurford et al. 2007a). We also successfully reproduce equatorial cycloids, including the cycloid fit by Hurford et al. (2009a); our methodology allows a more precise estimate of the obliquity required for this feature (Section 3.5.2). Statistical analysis shows that a tidal model including obliquity is heavily favored over models that do not (Section 3.5.1). When we combine obliquity with other effects, we find that

neither fast precession nor non-synchronous rotation stresses make significant contributions in most cases, but physical libration further improves our fits, sometimes by an order of magnitude. In fact, we show that a tidal model that includes both obliquity and physical libration is favored over all other models (Section 3.5.1). We find Europa's obliquity to be large (for a tidally-damped satellite) and different for each feature, as expected for a mechanically decoupled ice shell. Since the predicted timescale for obliquity change is short compared to Europa's surface age (Bills et al. 2009), it is reasonable to expect that cycloids, which may have formed at different times in Europa's history, would also have formed with different amounts of obliquity. The relatively large and varying libration amplitudes we find are also best explained by the presence of a global ocean, which could act to decouple the shell and interior of Europa.

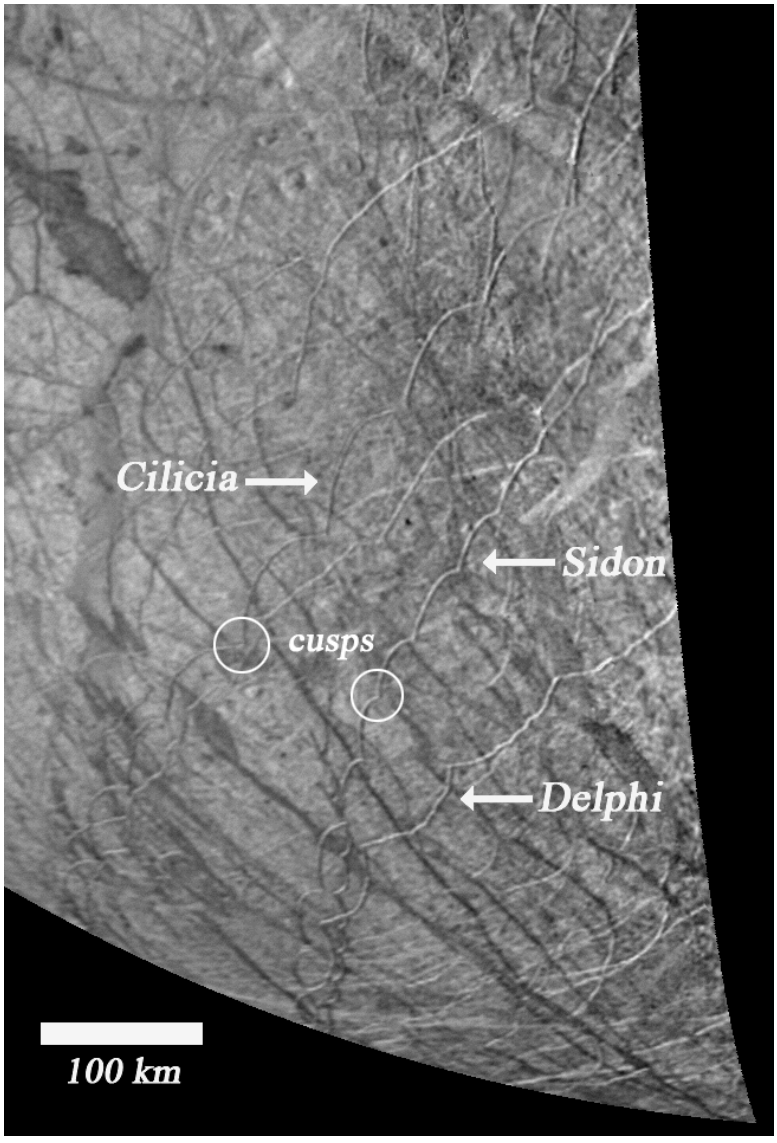

Figure 3.1: Mosaic of Voyager 2 images (PIA00325) showing the three southern hemisphere cycloids in this study: Cilicia, Sidon, and Delphi. Examples of cusps are marked with white circles.

3.2 The history of cycloid modeling

Hoppa et al. (2001) showed that a formation model based on tidal stress could account for the general trends of cycloids in the southern hemisphere of Europa (Fig. 3.1) when the calculated stresses included the effects of Europa's forced eccentricity. However, in creating these fits, Hoppa et al. (2001) imposed the condition that the crack always stops propagating at the end of each Europan orbit in order to ensure that a cusp is generated when cracking reinitiates in the next orbit. Hurford et al. (2007a) removed this condition and was still successful at matching the general shapes of cycloids in the southern hemisphere although they required different parameters than were reported by Hoppa et al. (2001). Hurford et al. (2007a) was able to further improve fits after allowing the mechanical parameters (the stress at which the crack will start and stop propagating and the crack propagation speed) to vary arbitrarily for each arc of a cycloid. Whether this variation reflects real differences in the material properties of Europa's ice shell is unclear; the improvement in fit may have only been due to the addition of free parameters. Fits from both studies required shifts in formation longitude from the current locations of the observed cycloids, which was attributed to non-synchronous rotation of the ice shell (Hoppa et al. 2001). In fact, Hurford et al. (2007a) obtained slightly better fits when they added stress from 0.5° of non-synchronous rotation (NSR) into the tidal model used to reproduce cycloids. However, their model failed to reproduce observed equatorial and equator-crossing cycloids even with stress from non-synchronous rotation (Hurford et al. 2007a; Hurford et al. 2009a).

Hurford et al. (2009a) examined the effects of a hypothetical obliquity of 0.1° on the global cycloid distribution especially insofar as it pertained to equatorial and equator-crossing cycloids. In the absence of obliquity, the stress field is symmetric across the equator, which restricts the formation of equator-crossing cycloids to certain longitudes and propagation directions (nearly north-south). In addition, these simulated equatorial cycloids appear boxy and quite distinctive from the arcuate features predicted for other regions of the stress field. These characteristics are inconsistent with many observed cycloids. However, boxy cycloids are indeed observed on Europa and cluster in two regions that lie ~180° apart. The better imaged of these regions is referred to as the Wedges (Argadnel Regio). The eccentricity-only model predicts that these regions would both be centered on the equator. Instead, one region lies just north of the equator, and the other is just south. These regions deviate from the predictions in the opposite direction expected from polar wander (Sarid et al. 2002). For certain spin pole directions, an obliquity of at least 0.1° would result in an offset of the Wedges regions by an amount and in a direction that is consistent with the observations (Hurford et al. 2009a).

At longitudes outside of the regions of boxy cycloids, the stress field with obliquity would produce arcuate equator-crossing cycloids with arcs of consistent concavity, in agreement with observations. However, 0.1° of obliquity was insufficient to reproduce an observed equator-crossing cycloid informally called Tyrrel (Hurford et al. 2009a). Rather, an obliquity of 0.25° resulted in a qualitatively good, albeit preliminary, fit. This fit used a different set of mechanical parameters for each arc (30 free parameters in all) and did not reproduce the last arc. The 30-dimensional parameter space was searched by hand and the quality of the fit was determined subjectively, which was the same method used to obtain fits to cycloids in the southern hemisphere (Hoppa et al.

2001; Hurford et al. 2007a).

The results presented by Hurford et al. (2009a) indicate that an obliquity of 0.1°, the value expected from interactions between a solid Europa and the other large satellites, would alter the tidal stress field in ways that make global cycloid patterns more consistent with observations. However, the value of the obliquity is still in question as the only fit to an observed, equator-crossing cycloid required a larger obliquity. The reliability of the 0.25° result is further diminished by the use of so many free parameters in achieving the fit to Tyrrel. Finally, the methods used to identify and evaluate potential fits were not systematic enough to ensure the best fit within parameter space was identified.

Our work is an improvement over previous studies because we (1) include the effects of obliquity, non-synchronous rotation, fast precession, and physical libration, (2) use numerical methods to comprehensively explore parameter space, (3) use a quantitative rather than subjective measure of fit quality, and (4) apply statistical analysis to compare tidal models and constrain the values of the parameters in each model.

3.3 Methodology

3.3.1 Tidal models under consideration

We used the physical model described in the introduction (section 3.1) and the expanded tidal stress equations derived in Chapter 2 to test several tidal models, all of which include the effects of eccentricity. We begin with the simplest models to determine the relative importance of non-synchronous rotation (NSR) and obliquity. These include eccentricity-only (Null), NSR stress (NSRnoO), obliquity (OBLQ), and obliquity plus NSR stress (NSRO). The eccentricity-only model has four free parameters: formation longitude, the time at which the crack begins propagating (a proxy for initiation threshold), propagation threshold, and speed. Stress from non-synchronous rotation adds one free parameter whereas the obliquity model requires two additional parameters: obliquity and spin pole direction. To examine the additional influence of physical libration and fast precession, we test the following models, all of which include eccentricity and obliquity: fast precession (RateO), physical libration (LibO), and libration with fast precession (LibRateO). In all cases, we allow the formation longitude of the cycloid to vary, presumably due to non-synchronous rotation, even when NSR stress is not included.

3.3.2 Finding and evaluating fits

Latitude and longitude information for Europan cycloids was obtained from the Galileo data set. Most cycloids appear as typical double ridges, so we recorded the location of the central trough of the cycloid as a proxy for the crack propagation path. This method is limited by the resolution of the images and the clarity of the path. Younger cycloids tend to have more clearly defined paths, although cycloids that do not have well-developed ridges (thought to be a sign of youth) can be difficult to trace especially when they are parallel to the sun direction. In addition to the southern hemisphere cycloids fit by previous authors, we selected three equatorial cycloids that each had three or more complete arcs (i.e. cusps on both sides of the arc were visible), were not significantly disrupted within those arcs, and had arcs with substantial radius of

curvature such that a straight line through the arc would be a poor fit. In theory, we could include all cycloids that meet these qualifications in our study. However, the main goal of this work was to test different tidal models to determine if they contain a signal of rotational parameters that have not been measured directly. Once a preferred tidal model has been identified, comprehensive mapping and modeling of cycloids could be a very useful next step.

In order to evaluate a fit, we first translate the observed cycloid data points in longitude such that the starting point of the observed and simulated cycloids are the same, since the difference in starting longitude is attributed to non-synchronous rotation moving the cycloid rather than model misfit. We then compute the deviation in latitude and longitude by comparing the data points to interpolated points on the simulated curve that lie at the same fractional length as the data points. From this, we obtain a χ^2 for the model fit and then divide by the number of data points to achieve the reduced χ^2.

For the elastic parameters, we use the values of $\mu = 3.52 \times 10^9$ Pa and $\nu = 0.33$, which are appropriate for water ice (Gammon et al. 1983). We set $h_2 = 1.275$, which corresponds to a 30m tidal amplitude (Greenberg et al. 1998). These are the same values used in previous modeling studies (Hoppa et al. 2001; Hurford et al. 2007a). As mentioned in section 2.1, these values will not influence our results; we include them here only for reproducibility.

The ranges of the model parameters that define our search space are listed in Table 3.1. The starting longitude of the cycloids can vary a full 360°; with obliquity there is no symmetry across the sub-Jupiter point. The obliquity of Europa is known to be low, so we limited the obliquity to 3°. The spin pole direction can vary from 0°- 360°. Although the stress field with obliquity is not symmetric about the sub-Jupiter point, there is a degeneracy between longitude and spin pole direction such that, when both are modulated by 180°, the stress field is identical. The amount of stress that can accumulate due to non-synchronous rotation has been restricted to less than 3°. The libration amplitude ranges from 0°-3°, and the phase can vary from 0°-360°. The precession rate ranges from 0°-2.5°. The number of (Eulerian) time steps per orbit constrains the possible values of the starting time (the point in the orbit at which the crack begins propagating); we use 850 time steps per orbit. The crack propagation speed can be up to 20 m/s with this time step.

In our simulations, the threshold for crack initiation is specified through the selection of a time in the orbit when the crack will begin propagating. That way, the initiation stress is restricted to values that exist within the stress field without us having to guess the maximum stress that can be achieved with each tidal model. The threshold for crack initiation is also required to be greater than the propagation threshold, which determines at what stress the crack stops moving. Both thresholds must be greater than zero, as we hypothesize these cracks to form and propagate in tension.

In the original cycloid modeling work of Hoppa et al. (2001), only one set of parameters governed the formation of the entire cycloid. In more recent studies (Hurford et al. 2007a; Sarid et al. 2006; Hurford et al. 2009a) the mechanical parameters were varied for each arc of a cycloid. It was thought that the surface could be heterogeneous in ways that allow arcs to form at different thresholds or propagate at different speeds. For this work, we did not vary the cracking parameters over the length of a cycloid. It was our hypothesis that including the effects of additional dynamical parameters and using

automated parameter searching would allow us to identify parameter sets that provide good fits to observed cycloids without adding these extra degrees of freedom, thus strengthening our results.

When a cycloidal crack first begins propagating, it can go in one of two directions (e.g – southwest or northeast). Without obliquity, the propagation direction and the concavity of the cycloidal arcs are linked, so the propagation direction of a cycloid can be determined by simple observation (Hoppa et al. 2001). However, both obliquity and libration alter the stress patterns such that cracks can propagate in either direction with the same concavity. To deal with this ambiguity, the initial propagation direction (east to west or west to east) is specified at the beginning of the simulation, and runs in both directions were attempted for each cycloid for tidal models that included obliquity or libration.

To determine the set of model parameters that best reproduces an observed cycloid, we developed an automated parameter-searching algorithm that combines Broyden-Fletcher-Goldfarb-Shanno (BFGS) conjugate gradient optimization (Dennis and Schnebal 1983; Jacobs 1977), global 1, 2, and 3 dimensional parameter scanning, and local Monte Carlo search methods (Hastings 1970). The fitting process begins with a random set of parameter values; the cycloid they produce is compared to the data and the initial χ^2 is determined. Coarse-grid scans of the parameter space are then performed, and the parameter set that produces a cycloid with the lowest χ^2 is adopted (provided that this value is less than the initial χ^2). Once this initial scan is complete, the BFGS optimization algorithm begins at the parameter set found by the scan and takes small steps through parameter space reducing the χ^2. Because the likelihood surface is rough even on small scales, local Monte Carlo is used to further constrain the minimum identified using BFGS. We then perform additional scans, increasing the number of dimensions over which the scanning occurs and decreasing the grid spacing, in search of another, disconnected region of parameter space with lower χ^2. The combination of these search strategies allows us to explore the local parameter region and to make large jumps to reach other basins around other minima. The simulation ends when even the finest scans over three dimensions of parameter space fail to identify a lower χ^2 parameter set. Such a complex approach is required due to the complexity of the fitness landscape. Tiny changes in some model parameters can lead to large changes in the quality of a fit. For example, a small change in a parameter that controls the stress field may reduce the stress just enough to inhibit crack initiation after a cusp or prevent cycloid formation altogether. Despite our multi-pronged approach, the algorithm can still become trapped in local minima, so we run 500 simulations each starting in a different, randomly-chosen, region of parameter space.

This methodology allows us to determine uncertainties in our fit parameters. We use Markov Chain Monte Carlo (Hastings 1970), beginning at the ending points of our most promising simulations, to create histograms for each parameter. We also identify the parameter set that produced the lowest chi-squared within each Markov Chain. To compute the uncertainty for a given parameter, we apply the expression

$$(3.1) \quad \delta\beta^2 = < (\beta_i - \beta^*)^2 >_i$$

where β is any varied parameter of interest, β^* is the value corresponding to the best fit

(lowest χ^2), i represents each entry in the Markov Chain, and $\delta\beta$ is the 1σ (68%) uncertainty. Since we vary the time in the orbit at which the crack began propagating as a proxy for the initiation threshold, we do not report uncertainties for initiation threshold. Our strategy is an improvement over that of previous cycloid modeling efforts, which relied on manual parameter searches and subjective evaluation of fits and were thus unable to compute uncertainties (Hoppa et al. 2001; Hurford et al. 2007a; Hurford et al. 2009a). However, the runtime of each simulation, the numerous simulations we complete for each model and each cycloid, and the lengthy Markov Chains required for error analysis do make this approach computationally intensive.

Table 3.1: Parameters and range of values

Parameter	**Range of allowed values**
Longitude	0 - 360º
Obliquity	0 - 3.0º
Spin pole direction	0 - 360º
Amount of NSR that produces stress	0 - 3.0º
Start time (proxy for crack initiation threshold)	Number of steps per orbit (850)
Threshold for crack propagation	> 0 and ≤ 200kPa
Apparent propagation speed	> 0 and ≤ 20 m/s
Libration amplitude	0 - 3.0°
Libration phase	0 - 360º
Precession rate	0 - 2.5°/day

3.4 Results

We reproduced three of the cycloids considered by Hoppa et al. (2001) and Hurford et al. (2007a), which lie in the southern hemisphere (Fig. 3.1), and three equatorial cycloids (Fig. 3.2), including the one fit by Hurford et al. (2009a). Figure 3.3a-c shows our best fits to the southern hemisphere cycloids using three tidal models: Null, NSRnoO, and OBLQ. Fits for the equatorial cycloids are shown in Fig. 3.4a-c. For each cycloid, the black, dotted line traces out the data points we extracted from Galileo imagery and the colored lines are our best fits for each model. The χ^2, best-fit parameters, and corresponding uncertainties are listed in Table 3.2; the exact values used to generate the plots are given in Table 3.3. The fits are shown at the current longitudes of the observed cycloids, but they were produced at different longitudes, implying that these cycloids have migrated since they formed. In Table 3.2, we report both the longitude at which we obtained the fit (Formation longitude) and the amount of eastward migration from the fit longitude to the observed longitude (Longitude migration), which is consistent with the hypothesis that eastward non-synchronous rotation is the mechanism for longitudinal displacement of the cycloids. The fits with the OBLQ model are far superior to those using the Null model, and to the NSRnoO model in all but one case, and imply a range of obliquity values, from 0.23°-0.83°, and variable spin pole directions.

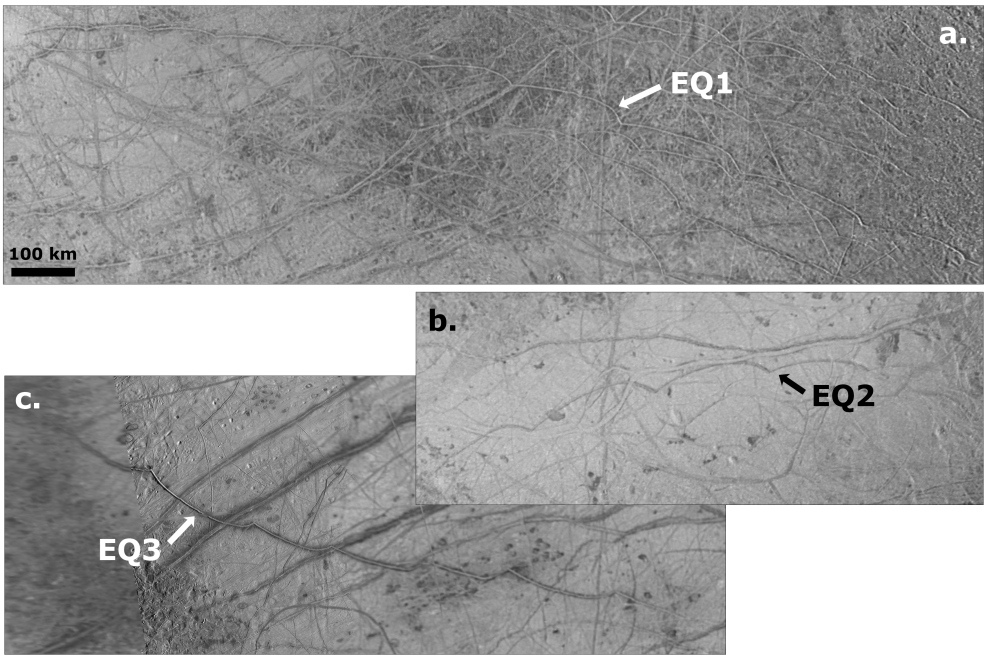

Figure 3.2: Images from a global mosaic showing the three equatorial cycloids included in this study: (a) EQ1, (b) EQ2, and (c) EQ3.

After achieving improved fits with obliquity, we fit the same six cycloids with four models that included obliquity and additional rotational parameters. As shown in Table 3.2, adding fast precession (RateO) produced zero to less than 1% improvement in fits. Adding NSR stress (NSRO) produced mixed results. There was no improvement in χ^2 for Cilicia or EQ2 and only a few percent for Delphi, and the best fits included almost no stress from NSR. On the other hand, there was substantial improvement (32-46%) in χ^2 for the fits to EQ1, EQ3, and Sidon, which required 0.1728°, 0.4022°, and 0.7785° of NSR stress, respectively. In fact, the fit to EQ1 produced using the NSRO model is the best EQ1 fit that we achieved. Although fits to these three cycloids improved with stress from NSR, the required longitude migration was comparable to that found using the OBLQ model.

The most significant overall improvements came from the addition of physical libration (LibO); incorporating fast precession as well (LibRateO) only improved fits by zero to a few percent. Figure 3.5a-c shows the LibO model fits (solid lines) to each of the southern hemisphere cycloids (dotted lines); Figure 3.6a-c shows the equatorial cycloid fits. The fit to EQ2 is quite good, having a chi-squared of only 24.72 (a 96% decrease in χ^2 from the OBLQ fit), which corresponds to an average difference in the location of a model and data point of less than 5 km or 5 pixels in the image. The fits to the other cycloids are improved by 23 – 62% over the OBLQ model fits although the fit to EQ1 is not the best model fit we found and has some troubling characteristics. Although it captures the trend and concavity of the arcs across the equator and fits the two eastern-most arcs quite well, it has two long arcs rather than four short arcs on the western portion of the cycloid.

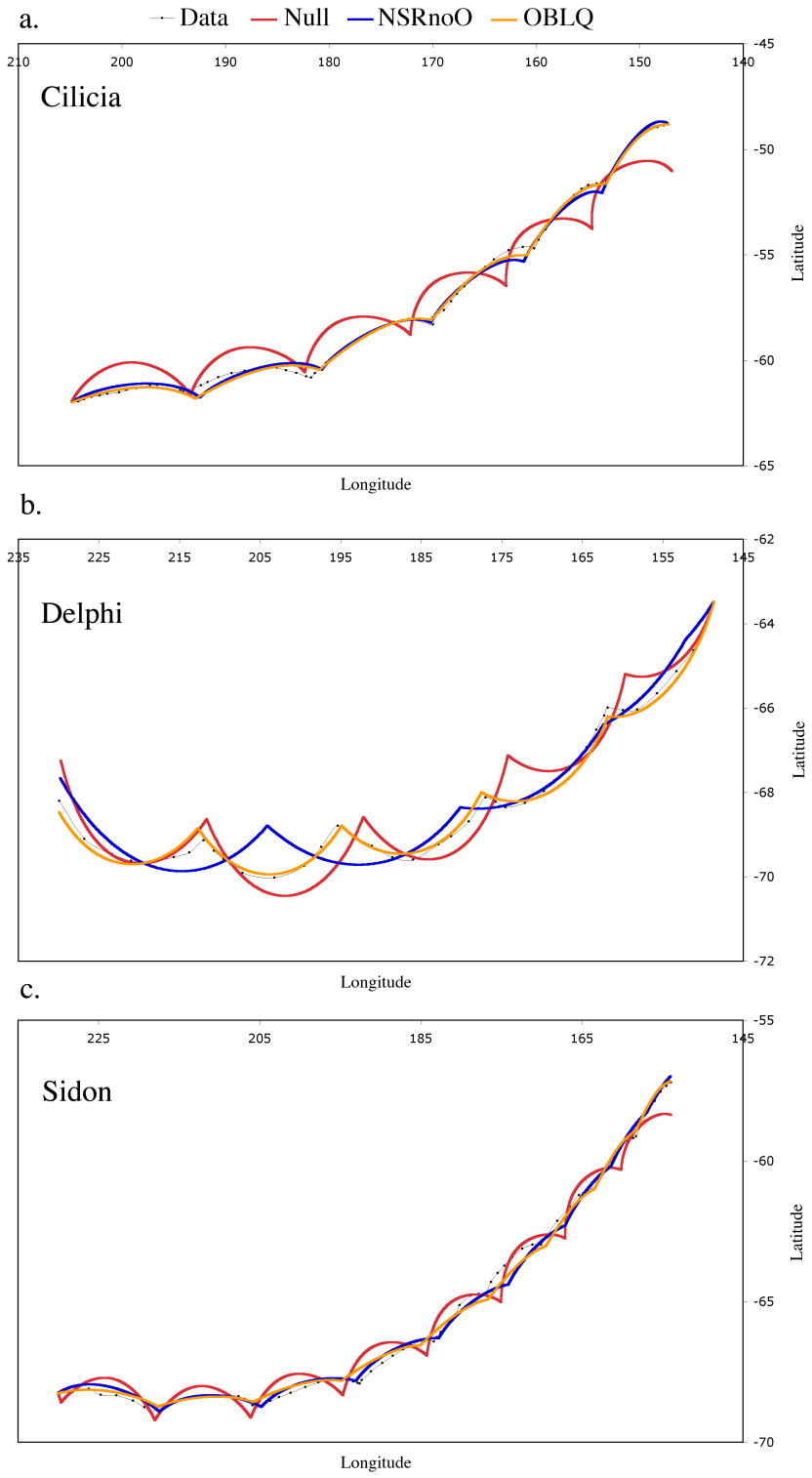

Figure 3.3: Fits to the three southern hemisphere cycloids: (a) Cilicia, (b) Delphi, and (c) Sidon. Data for each cycloid is shown as a black dotted line. The best fit with the eccentricity-only model (Null) is shown in red, the model with stress from non-synchronous rotation (NSRnoO) in blue, and obliquity (OBLQ) in orange.

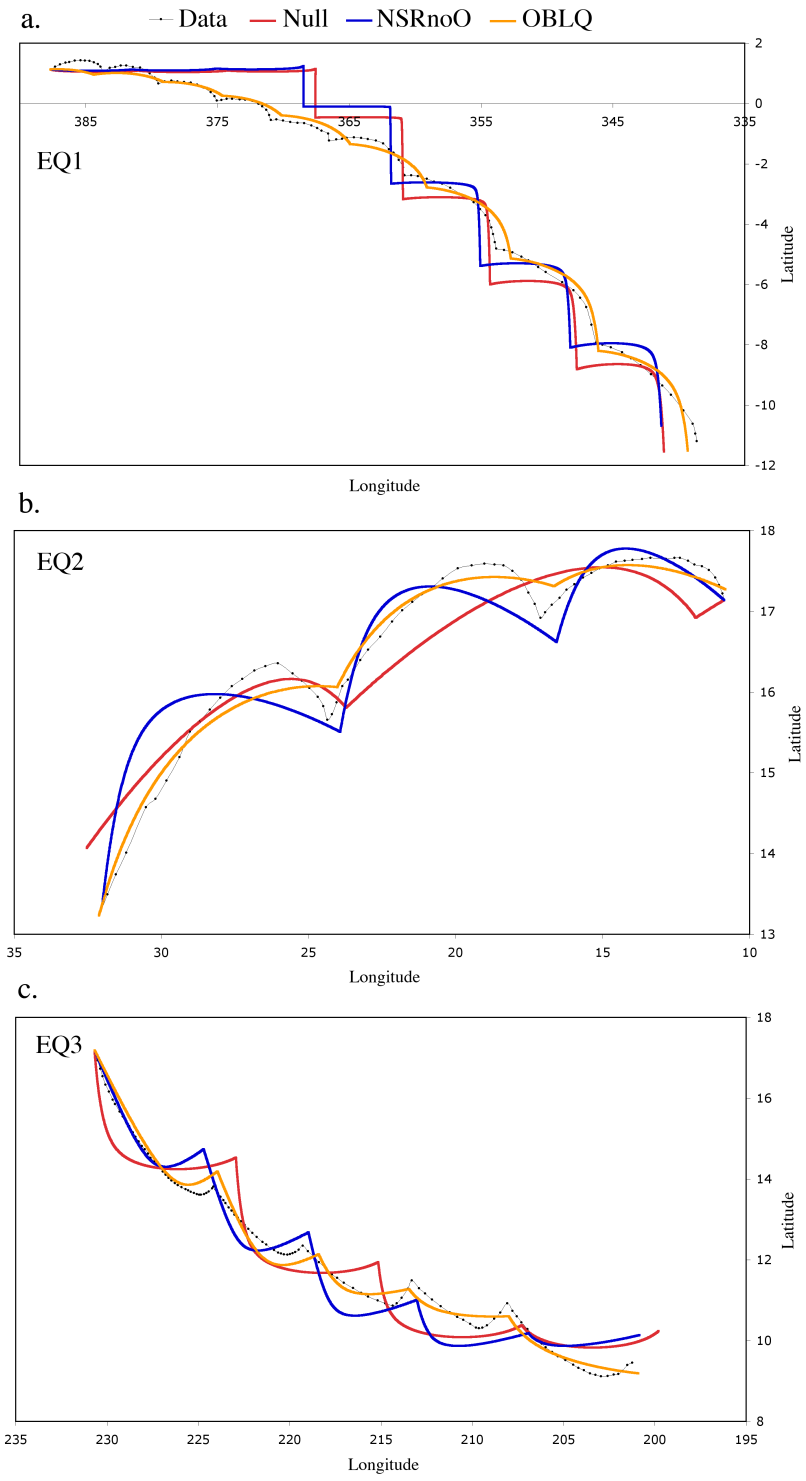

Figure 3.4: Fits to the three equatorial cycloids: (a) EQ1, (b) EQ2, and (c) EQ3. Data for each cycloid is shown as a black dotted line. The best fit with the eccentricity-only model (Null) is shown in red, the model with stress from non-synchronous rotation (NSRnoO) in blue, and obliquity (OBLQ) in orange.

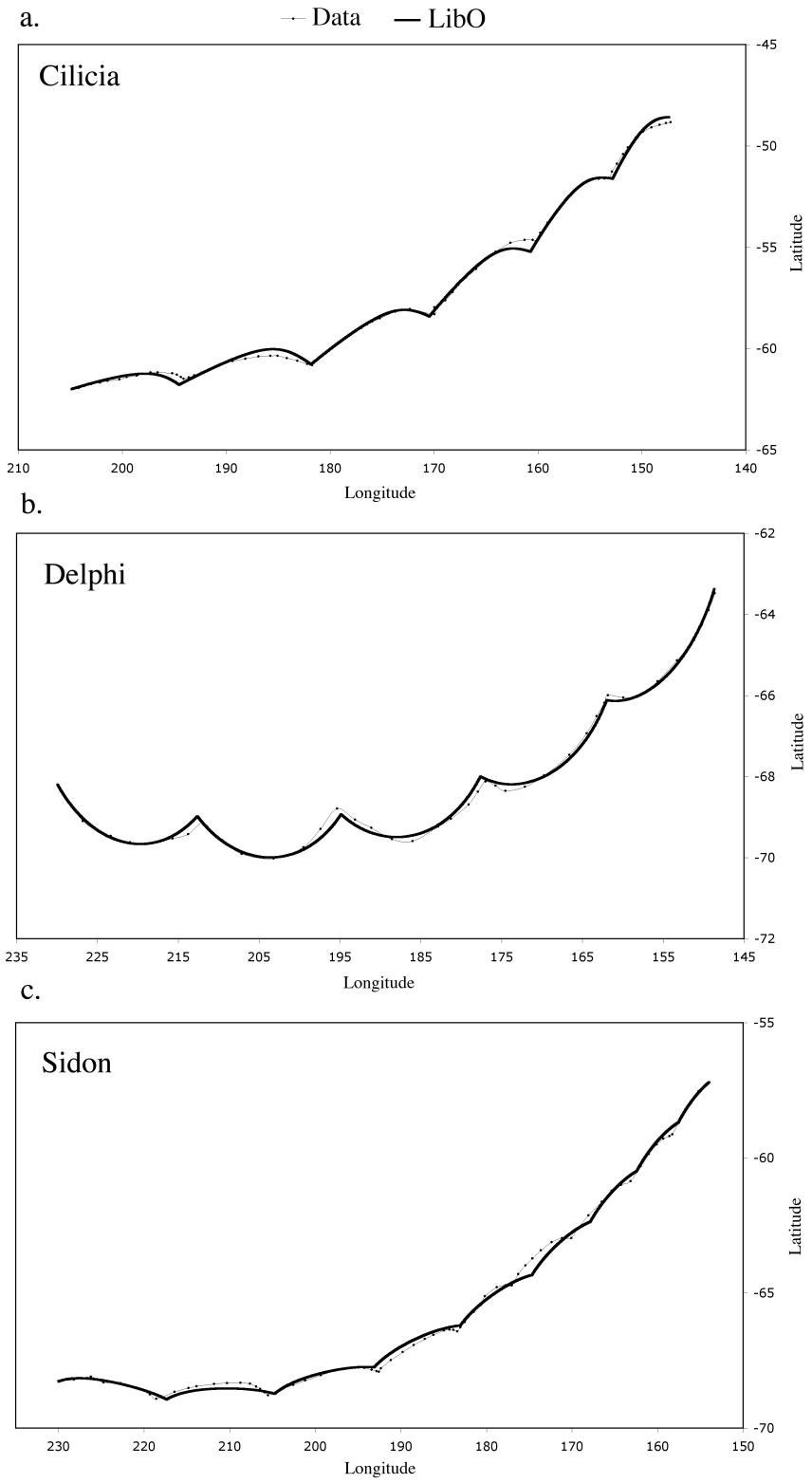

Figure 3.5: Fits to the three southern hemisphere cycloids: (a) Cilicia, (b) Delphi, and (c) Sidon. Data for each cycloid is shown as a black dotted line. The solid black line is the best fit using the libration model (LibO), which also includes obliquity.

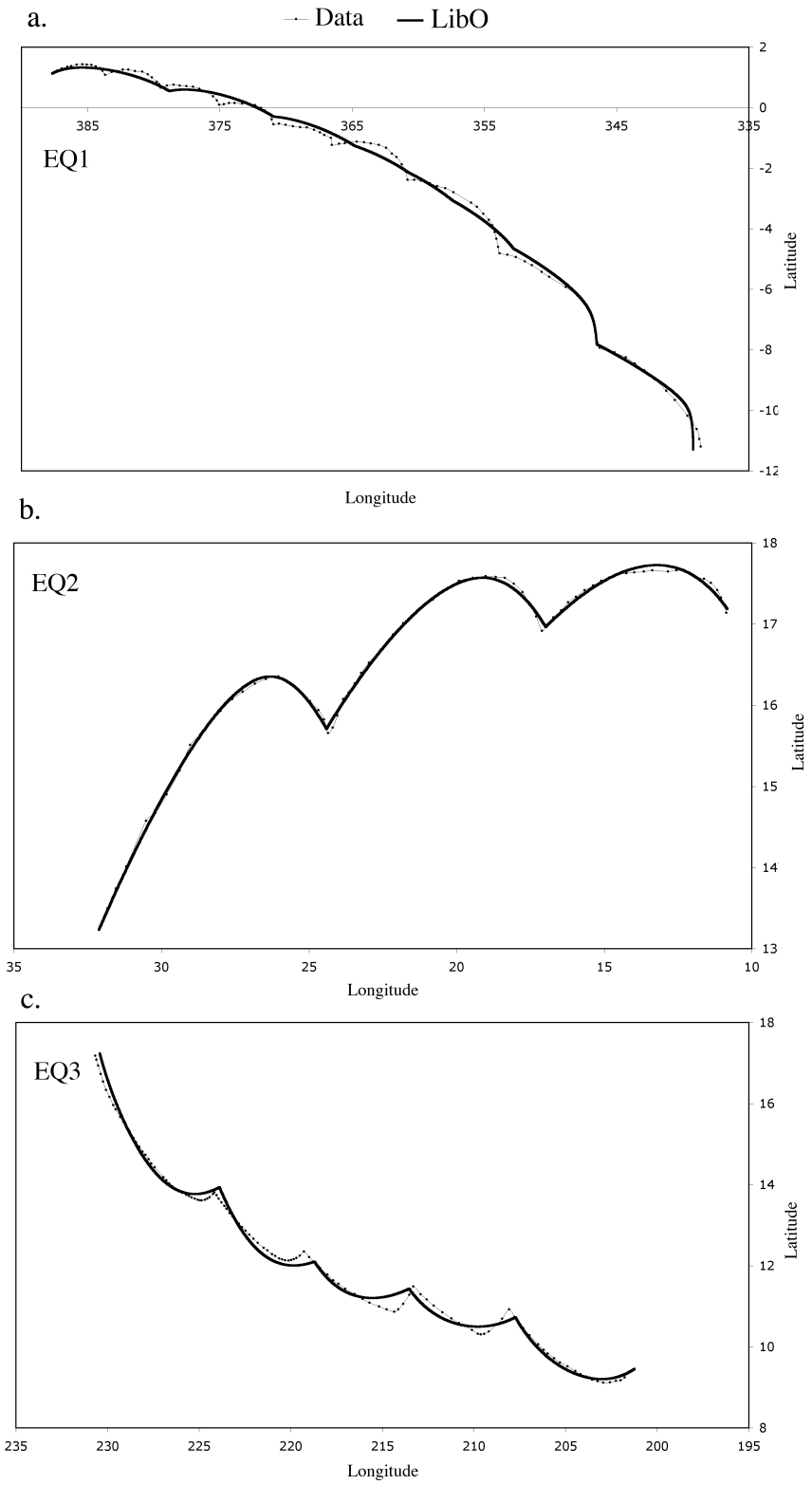

Figure 3.6: Fits to the three equatorial cycloids: (a) EQ1, (b) EQ2, and (c) EQ3. Data for each cycloid is shown as a black dotted line. The solid black line is the best fit using the libration model (LibO), which also includes obliquity.

Table 3.2: Cycloid modeling results

Model name	Rotational parameters tested	Feature	Prop dir	χ^2	Formation longitude (1)	Formation longitude (2)	Longitude migration (1)	Longitude migration (2)	Obliq (°)	Spin pole direction (1) (°)	Spin pole direction (2) (°)	NSR stress (°)	Libration amplitude (°)	Libration phase (°)	Precession rate (°/day)	Initiation threshold (kPa)	Propagation threshold (kPa)	Propagation speed (km/hr)
Null	-	Cilicia	W2E	19949.03	271.169 ± 0.015	91.169	66.299	246.299	-	-	-	-	-	-	-	31	31.500 ± 0.016	2.8836 ± 0.0007
NSRnoO	NSR	Cilicia	W2E	1117.17	226.247 ± 0.034	46.247	21.377	201.377	-	-	-	0.8689 ± 0.0018	-	-	-	53	15.914 ± 0.13	2.6416 ± 0.0044
OBLQ	OBLQ	Cilicia	W2E	802.40	52.761 ± 0.046	232.761	207.891	27.891	0.6854 ± 0.0028	8.54 ± 0.28	188.54	-	-	-	-	96	34.76 ± 0.12	5.5933 ± 0.0075
NSRO	OBLQ, NSR	Cilicia	W2E	802.40*	52.761 ± 0.046	232.761	207.891	27.891	0.6854 ± 0.0028	8.54 ± 0.28	188.54	0.00	-	-	-	96	34.76 ± 0.12	5.5933 ± 0.0075
RateO	OBLQ, Precession rate	Cilicia	W2E	801.28	52.214 ± 0.046	232.214	207.344	27.344	0.6716 ± 0.0017	4.25 ± 0.36	184.25	-	-	-	0.7285 ± 0.0040	95	34.83 ± 0.13	5.583 ± 0.014
LibO	OBLQ, Libration	Cilicia	W2E	613.85	268.93 ± 0.18	88.932	64.062	244.062	0.7273 ± 0.0062	276.44 ± 0.51	96.44	-	0.716 ± 0.014	17.34 ± 0.42	-	94	27.29 ± 0.81	5.613 ± 0.011
LibRateO	OBLQ, Libration, Precession rate	Cilicia	W2E	613.74	268.90 ± 0.15	88.899	64.03	244.03	0.7274 ± 0.0015	276.38 ± 0.17	96.375	-	0.718 ± 0.001	17.23 ± 0.16	0.0007 ± 0.0012	94	27.176 ± 0.11	5.6170 ± 0.0089
Null	-	Delphi	E2W	3810.29	36.276 ± 0.015	216.276	247.646	67.646	-	-	-	-	-	-	-	62	61.607 ± 0.013	5.2323 ± 0.0022
NSRnoO	NSR	Delphi	E2W	2716.28	198.817 ± 0.021	18.817	50.187	230.187	-	-	-	0.0638 ± 0.0003	-	-	-	76	75.751 ± 0.011	12.6410 ± 0.0087
OBLQ	OBLQ	Delphi	E2W	396.98	208.788 ± 0.032	28.788	60.158	240.158	0.4429 ± 0.0007	187.74 ± 0.11	7.744	-	-	-	-	67	62.597 ± 0.051	6.6003 ± 0.0091
NSRO	OBLQ, NSR	Delphi	E2W	385.79	208.495 ± 0.041	28.495	59.865	239.865	0.4340 ± 0.0009	184.14 ± 0.14	4.137	0.0255 ± 0.0002	-	-	-	65	64.532 ± 0.062	6.537 ± 0.011
RateO	OBLQ, Precession rate	Delphi	E2W	396.98	208.788 ± 0.027	28.788	60.158	240.158	0.4429 ± 0.0006	187.74 ± 0.09	7.744	-	-	-	0.0000 ± 0.0023	67	62.597 ± 0.045	6.6003 ± 0.0076
LibO	OBLQ, Libration	Delphi	W2E	234.75	118.77 ± 0.16	298.77	248.84	68.84	0.4833 ± 0.0017	175.03 ± 0.18	355.03	-	2.1377 ± 0.0014	357.789 ± 0.060	-	62	51.72 ± 0.19	6.3361 ± 0.0092
LibRateO	OBLQ, Libration, Precession rate	Delphi	W2E	232.60	118.797 ± 0.031	298.797	248.867	68.867	0.5459 ± 0.0011	169.48 ± 0.09	349.48	-	2.1070 ± 0.0004	357.486 ± 0.027	2.2846 ± 0.0014	58	47.566 ± 0.066	6.0860 ± 0.0057
Null	-	Sidon	W2E	5132.13	282.246 ± 0.012	102.246	52.216	232.216	-	-	-	-	-	-	-	48	37.856 ± 0.025	2.4127 ± 0.0003
NSRnoO	NSR	Sidon	W2E	874.16	72.569 ± 0.020	252.569	202.539	22.539	-	-	-	0.2804 ± 0.0005	-	-	-	71	45.475 ± 0.066	3.2244 ± 0.0022
OBLQ	OBLQ	Sidon	W2E	945.11	245.782 ± 0.030	65.782	15.752	195.752	0.5817 ± 0.0017	120.50 ± 0.49	300.50	-	-	-	-	73	45.153 ± 0.094	4.4365 ± 0.0087
NSRO	OBLQ, NSR	Sidon	W2E	594.21	67.219 ± 0.032	247.219	197.189	17.189	0.6585 ± 0.0015	204.02 ± 0.05	24.024	0.7785 ± 0.0010	-	-	-	64	51.52 ± 0.11	2.5819 ± 0.0013
RateO	OBLQ, Precession rate	Sidon	W2E	939.99	245.121 ± 0.014	65.121	15.091	195.091	0.6185 ± 0.0004	114.19 ± 0.23	294.19	-	-	-	0.2214 ± 0.0012	73	46.557 ± 0.031	4.6336 ± 0.0032
LibO	OBLQ, Libration	Sidon	E2W	515.94	46.915 ± 0.041	226.915	252.955	72.955	0.6242 ± 0.0013	214.01 ± 0.14	34.011	-	1.9254 ± 0.0009	12.359 ± 0.042	-	61	33.744 ± 0.049	3.8283 ± 0.0038
LibRateO	OBLQ, Libration, Precession rate	Sidon	E2W	497.86	37.739 ± 0.050	217.739	243.779	63.779	0.4735 ± 0.0008	216.78 ± 0.09	36.784	-	1.7712 ± 0.0005	8.254 ± 0.051	2.1832 ± 0.0005	53	38.926 ± 0.046	3.9268 ± 0.0024
Null	-	EQ1	W2E	7442.50	99.245 ± 0.027	279.245	71.575	251.575	-	-	-	-	-	-	-	22	21.693 ± 0.025	4.5677 ± 0.0086
NSRnoO	NSR	EQ1	W2E	7430.11	278.44 ± 0.38	98.44	250.77	70.77	-	-	-	0.175 ± 0.054	-	-	-	24	23.86 ± 0.62	4.543 ± 0.038
OBLQ	OBLQ	EQ1	W2E	721.51	280.94 ± 0.48	100.94	253.27	73.27	0.2278 ± 0.0032	3.00 ± 0.56	183.00	-	-	-	-	83	39.03 ± 0.15	6.679 ± 0.030
NSRO	OBLQ, NSR	EQ1	W2E	489.31	285.72 ± 0.50	105.72	258.05	78.05	0.2769 ± 0.0036	14.12 ± 1.08	194.12	0.1728 ± 0.0026	-	-	-	80	37.62 ± 0.24	5.9339 ± 0.0059
RateO	OBLQ, Precession rate	EQ1	W2E	721.16	280.940 ± 0.044	100.940	253.27	73.27	0.2282 ± 0.0026	2.92 ± 0.57	182.92	-	-	-	0.0000 ± 0.0021	83	39.04 ± 0.14	6.6797 ± 0.017
LibO	OBLQ, Libration	EQ1	W2E	521.46	103.87 ± 0.25	283.87	76.20	256.20	0.3158 ± 0.0027	226.26 ± 0.54	46.26	-	0.993 ± 0.013	84.50 ± 0.50	-	58	57.776 ± 0.017	7.745 ± 0.040
LibRateO	OBLQ, Libration, Precession rate	EQ1	W2E	508.31	258.66 ± 0.49	78.66	230.99	50.99	0.1855 ± 0.0003	350.15 ± 0.97	170.15	-	0.4825 ± 0.0032	35.42 ± 1.16	2.1637 ± 0.0029	59	58.75 ± 0.17	9.28 ± 0.10
Null	-	EQ2	E2W	2634.23	330.748 ± 0.011	150.748	319.881	139.881	-	-	-	-	-	-	-	65	56.792 ± 0.008	19.94743 ± 7E-05
NSRnoO	NSR	EQ2	E2W	1811.91	195.607 ± 0.010	15.607	184.740	4.740	-	-	-	1.14591 ± 0.00001	-	-	-	134	0.0000 ± 0.0015	4.7970 ± 0.0020
OBLQ	OBLQ	EQ2	W2E	597.32	307.77 ± 0.17	127.767	275.652	95.652	0.8319 ± 0.0009	45.23 ± 0.32	225.23	-	-	-	-	83	83.066 ± 0.093	9.087 ± 0.013
NSRO	OBLQ, NSR	EQ2	W2E	597.32	307.78 ± 0.12	127.775	275.660	95.660	0.8319 ± 0.0007	45.25 ± 0.23	225.25	0.00000 ± 2e-05	-	-	-	83	83.070 ± 0.067	9.0870 ± 0.0094
RateO	OBLQ, Precession rate	EQ2	W2E	597.32	307.768 ± 0.098	127.768	275.653	95.653	0.8319 ± 0.0006	45.23 ± 0.19	225.23	-	-	-	0.00000 ± 1.5e-04	83	83.067 ± 0.053	9.0868 ± 0.0073
LibO	OBLQ, Libration	EQ2	W2E	24.72	35.717 ± 0.086	215.717	3.602	183.602	0.9285 ± 0.0022	317.02 ± 0.13	137.02	-	1.5568 ± 0.0007	17.72 ± 0.10	-	70	59.33 ± 0.12	12.333 ± 0.011
LibRateO	OBLQ, Libration, Precession rate	EQ2	W2E	24.70	215.809 ± 0.072	35.809	183.694	3.694	0.9328 ± 0.0020	136.52 ± 0.18	316.52	-	1.5650 ± 0.0008	17.581 ± 0.079	0.1449 ± 0.0054	70	59.55 ± 0.19	12.309 ± 0.017
Null	-	EQ3	W2E	5648.27	119.69 ± 0.11	299.687	249.01	69.01	-	-	-	-	-	-	-	27	27.380 ± 0.083	5.0363 ± 0.0083
NSRnoO	NSR	EQ3	W2E	4143.35	174.97 ± 0.21	354.97	304.29	124.29	-	-	-	0.2762 ± 0.0013	-	-	-	58	58.429 ± 0.085	9.347 ± 0.024
OBLQ	OBLQ	EQ3	W2E	815.83	7.781 ± 0.025	187.781	137.10	317.10	0.5665 ± 0.0012	193.57 ± 0.12	13.57	-	-	-	-	64	60.185 ± 0.033	9.3254 ± 0.0092
NSRO	OBLQ, NSR	EQ3	W2E	436.88	350.080 ± 0.070	170.080	119.40	299.40	0.2150 ± 0.0008	225.05 ± 0.22	45.05	0.4022 ± 0.0008	-	-	-	56	51.015 ± 0.069	11.439 ± 0.015
RateO	OBLQ, Precession rate	EQ3	W2E	815.83	7.781 ± 0.023	187.781	137.10	317.10	0.5663 ± 0.0010	193.55 ± 0.12	13.55	-	-	-	0.0029 ± 0.0013	64	60.186 ± 0.026	9.3253 ± 0.0085
LibO	OBLQ, Libration	EQ3	E2W	311.02	345.973 ± 0.063	165.973	144.73	324.73	1.3452 ± 0.0028	273.40 ± 0.12	93.40	-	2.4445 ± 0.0031	353.964 ± 0.047	-	49	28.78 ± 0.11	5.470 ± 0.011
LibRateO	OBLQ, Libration, Precession rate	EQ3	E2W	310.97	345.988 ± 0.064	165.988	144.73	324.73	1.3439 ± 0.0025	273.27 ± 0.10	93.27	-	2.4423 ± 0.0019	353.945 ± 0.044	0.0012 ± 0.0041	49	28.66 ± 0.11	5.469 ± 0.010

Since there is degeneracy in longitude (without obliquity) and between longitude and spin pole direction (with obliquity), we list both sets of values as indicated by (1) and (2).
For a given model, parameters that were set to zero and not varied in the simulation have a dash rather than a numerical value.
*We were unable to find any set of parameters with NSR stress that were better than the Obliq best fit so we report results identical to the Obliq model.

Table 3.3: Parameter values used to generate the cycloids fits in Figures 3.3-3.6

Model name	Rotational parameters tested	Feature	Prop dir	Starting time step	Formation longitude	Oblq (°)	Spin pole direction (°)	NSR stress (°)	Libration amplitude (°)	Libration phase (°)	Precession rate (°/day)	Propagation threshold (bar)	Propagation speed (km/timestep)
Null	-	Cilicia	W2E	103.53396910	271.16946490	0.0	0.0	0.0	0.0	0.0	0.0	0.31499545980	0.28911163018
NSRnoO	NSR	Cilicia	W2E	327.04661570	226.24719840	0.0	0.0	0.86890223 27	0.0	0.0	0.0	0.15913847660	0.26485272 84
OBLQ	OBLQ	Cilicia	W2E	505.09938880	52.761283980	0.68539213 33	8.54002165	0.0	0.0	0.0	0.0	0.34763053930	0.56080344 50
LibO	OBLQ, Libration	Cilicia	W2E	398.89607340	268.93196100 0	0.72731714 71	276.44072480	0.0	0.71640096 37	17.334749200	0.0	0.27289029350	0.56282204 07
Null	-	Delphi	E2W	411.04138500	36.275995290	0.0	0.0	0.0	0.0	0.0	0.0	0.61607267980	0.52461211 22
NSRnoO	NSR	Delphi	E2W	581.70867730	198.81717100 0	0.0	0.0	0.06381837198	0.0	0.0	0.0	0.75751001310	1.26742579 00
OBLQ	OBLQ	Delphi	E2W	435.43571870	208.78786970 0	0.44292881 47	187.74442670	0.0	0.0	0.0	0.0	0.62596881140	0.66176631 66
LibO	OBLQ, Libration	Delphi	W2E	354.65475190	118.76900210 0	0.48333815 01	175.03296600	0.0	2.13766798 10	357.788634451	0.0	0.51724188340	0.63527623 22
Null	-	Sidon	W2E	680.86452890	282.24612350 0	0.0	0.0	0.0	0.0	0.0	0.0	0.37856092820	0.24190291 80
NSRnoO	NSR	Sidon	W2E	352.59644430	72.569199010	0.0	0.0	0.28034714 94	0.0	0.0	0.0	0.45475036000	0.32329053 42
OBLQ	OBLQ	Sidon	W2E	448.98226020	245.78211350 0	0.58168868 99	120.49620560	0.0	0.0	0.0	0.0	0.45153084910	0.44481884 41
LibO	OBLQ, Libration	Sidon	E2W	285.97470120	46.914821750	0.62416202 44	214.01053480	0.0	1.92535396 60	12.358851060	0.0	0.33743714750	0.38384009 06
Null	-	EQ1	W2E	553.83467720	99.245343730	0.0	0.0	0.0	0.0	0.0	0.0	0.21692636740	0.45797273 65
NSRnoO	NSR	EQ1	W2E	546.80445090	278.43764880 0	0.0	0.0	0.17467136 88	0.0	0.0	0.0	0.23857818210	0.45549829 99
OBLQ	OBLQ	EQ1	W2E	400.02806940	280.94194880 0	0.22776187 30	2.99824451	0.0	0.0	0.0	0.0	0.39030327340	0.66969039 91
LibO	OBLQ, Libration	EQ1	W2E	527.95420720	103.87191510 0	0.31582496 13	226.26257050	0.0	0.99259139 78	84.500665700	0.0	0.57776033920	0.77651162 30
Null	-	EQ2	E2W	273.34644460	330.7482958	0.0	0.0	0.0	0.0	0.0	0.0	0.5679258591	1.99999999 5
NSRnoO	NSR	EQ2	E2W	727.49971320	195.60652730 0	0.0	0.0	1.14591113 5	0.0	0.0	0.0	0.00000023249	0.48095074 75
OBLQ	OBLQ	EQ2	W2E	90.538138470	307.76669490 0	0.83187650 55	45.22795869	0.0	0.0	0.0	0.0	0.83065830250	0.91107249 55
LibO	OBLQ, Libration	EQ2	W2E	824.74094565	35.717131530	0.92845987 44	317.01853770	0.0	1.55683507 00	17.720215300	0.0	0.59327649750	1.23649506 90
Null	-	EQ3	W2E	461.77887650	119.68694940 0	0.0	0.0	0.0	0.0	0.0	0.0	0.27379668160	0.50495546 44
NSRnoO	NSR	EQ3	W2E	771.53110460	174.97123080 0	0.0	0.0	0.27617862 41	0.0	0.0	0.0	0.58428481840	0.93718803 24
OBLQ	OBLQ	EQ3	W2E	662.08602270	7.7808834 13	0.56649118 97	193.57363210	0.0	0.0	0.0	0.0	0.60185101680	0.93500194 46
LibO	OBLQ, Libration	EQ3	E2W	626.17963560	345.97331520 0	1.34524334 30	273.39988270	0.0	2.44446919 80	353.963976100	0.0	0.28783602220	0.54843736 78

The LibO fits are consistent with our OBLQ fits in that they indicate a variable obliquity and spin pole direction and require longitude migration. The obliquities are somewhat larger, however, ranging from 0.32 – 1.35°. The libration amplitudes are also variable and quite large with values of 0.72 – 2.44°; the libration phases cluster around 0°, ranging from -6.04° – 17.72° with one outlier at 84.5° from the fit to EQ1.
All of our best fits require a shift in longitude from the current locations of the observed cycloids. In Table 3.2, for models without obliquity, we list the formation longitude that resulted from our fitting procedure (marked as 1) and the longitude 180° away (marked as 2) as either location is equally possible. We also list the corresponding amount of eastward longitude migration implied for each location. With obliquity, there is a degeneracy between longitude and spin pole direction, so we have also listed the corresponding spin pole directions for each of the formation longitudes for each fit. Note that, in Table 3.2, the column labeled NSR stress refers to the amount of stress generated by non-synchronous rotation, not the amount of longitude migration. It is given in units of degrees, which corresponds only to the amount of non-synchronous rotation that still contributes to tidal stress and does not include stress that has relaxed or been accommodated by fracture.

3.5 Discussion

3.5.1 Model comparison

In addition to illustrating the precision of our results, the uncertainties shown in Table 3.2 can be used to determine whether an improvement in χ^2 from one model to the next is statistically significant. This is especially important when comparing models with different numbers of free parameters. We applied Bayesian statistical analysis (Sivia and Skilling 2006) to compare the best fits to each cycloid using the different tidal models. For all cycloids, the OBLQ model is strongly favored over the Null model despite the addition of two free parameters (obliquity and spin pole direction), strengthening the case for substantial Europan obliquity. Also, for all cycloids, the LibO model is strongly favored over the OBLQ model and, with the exception of EQ1, the LibO model is preferred over every other model we tested. The RateO model was never favored over OBLQ, and the LibRateO model was only preferred over LibO for EQ1, which suggests that precession is too slow to alter cycloid paths enough for us to detect. Adding NSR stress (NSRO) produced mixed results when compared to the OBLQ model (producing better fits to EQ1, EQ3, and Sidon) but was only preferred over the LibO model in one case: EQ1. Based on this statistical analysis, we conclude that (1) obliquity is supported and is more effective at reproducing observed cycloids than stress from non-synchronous rotation, (2) fast precession is not supported, and (3) the preferred tidal model incorporates both obliquity and physical libration (LibO).

3.5.2 Parameter values and implications

Fits generated using our preferred model, LibO, require longitude migration and indicate a large and variable obliquity, spin pole direction, and libration amplitude. The uncertainties on obliquity and libration amplitude are quite small and show that these parameters are not consistent across all cycloids to very high confidence. The obliquity

values for each fault, grouped by tidal model, are shown in Figure 3.7. The range of values within each model is remarkably consistent over all models. Only the best-fit obliquity value for EQ3 varies considerably between models; the best-fit obliquity value jumps from 0.57° for the OBLQ model to 1.35° using the LibO model. The high obliquity values we find are compatible with the expectation for a mechanically decoupled ice shell, and the variability in obliquity is consistent with the prediction of a geologically short timescale for obliquity variation (Bills 2005; Bills et al. 2009).

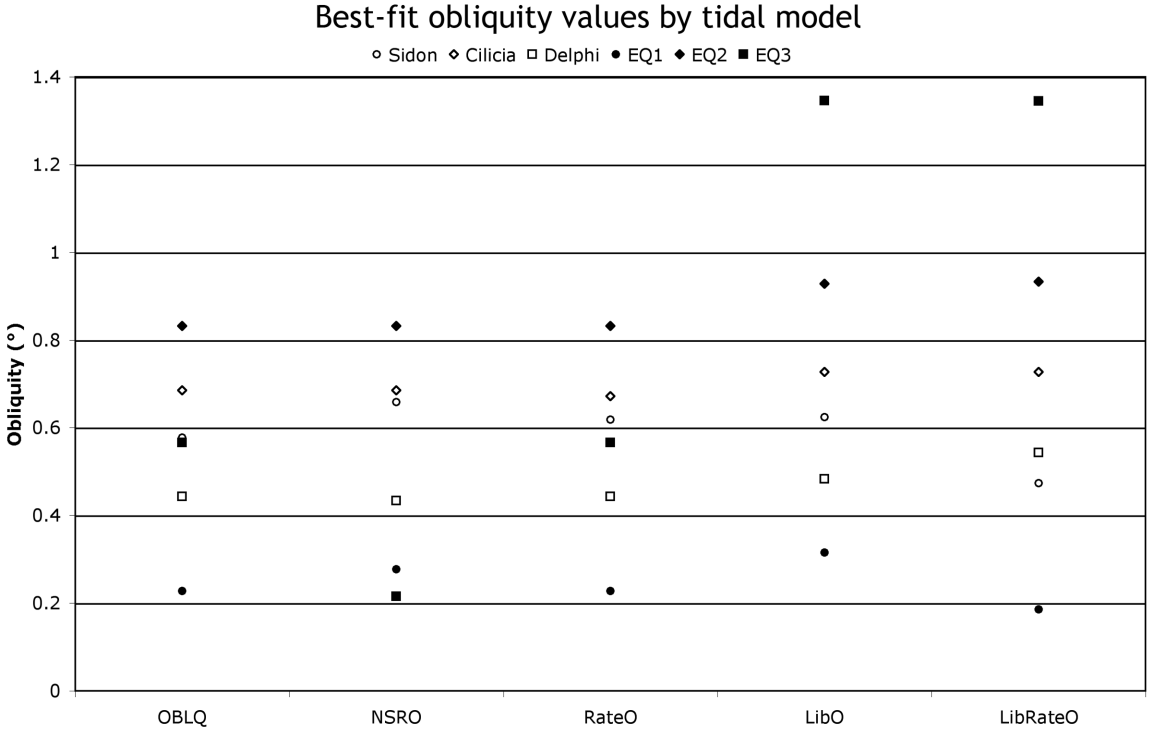

Figure 3.7: The best-fit obliquity values for each cycloid, grouped by tidal model. The values for each cycloid do not exhibit much variation across the models, with the exception of EQ3.

The libration amplitudes required for these fits are also rather large. The highest is for the EQ1 fit, which may be anomalous (see above), but the next highest libration amplitude is from the fit to Delphi, 2.14°, and that fit is quite good. These values are plausible in the presence of a global ocean (Bills et al. 2009; Van Hoolst et al. 2008), which could act as a decoupling layer. If Europa's current libration amplitude is in the range we find here, it may be detectable via spacecraft or possibly with Earth-based radar measurements. The values of libration phase cluster near 0°, which implies that the libration is nearly in phase with the motion of the tidal bulge.

In Figure 3.8, we show the minimum amount of longitude translation required for each cycloid using the two best tidal models (OBLQ and LibO). Due to degeneracy in the stress field, these values could change by 180° or any multiple of 180° and would create the same cycloid as long as the SPD changed by an equal amount. Therefore, these cycloids could have formed in less than half of one non-synchronous rotation of the ice

shell or over many rotations. Unfortunately, there are not enough cross-cutting relationships between these features to create an age sequence. Better imagery, especially of the equatorial regions of Europa, would certainly prove useful. If an age sequence could be constructed, it would constrain the amount of non-synchronous rotation required to fit all six cycloids. In the LibO model, four of the cycloids appear to have formed nearly contemporaneously, as they all require 64°-76° of shell rotation. The other two cycloids formed ~70° earlier and ~70° later in this model. This pattern is intriguing, but without the age constraints, there is not way to be sure that the faults formed this way. The simultaneous lack of need for NSR stress and requirement of longitude migration is consistent with the conclusion of Goldreich and Mitchell (2010) that, because non-synchronous rotation is limited by the stress it generates, the rotation must be slow enough that much of the stress relaxes leaving only a very small contribution to the tidal stresses that control cycloid formation.

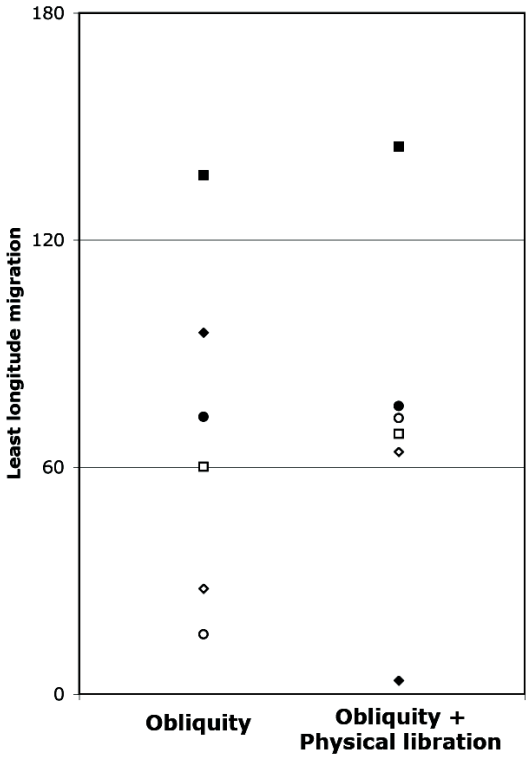

Figure 3.8: The minimum amount of longitude translation associated with the best fits using obliquity (left) and with physical libration as well (right). The open symbols represent the southern hemisphere cycloids; the filled symbols are the equatorial cycloids. In both cases, all six cycloids could have formed during less than half of one non-synchronous rotation of the shell. However, there is no way to constrain the amount of rotation without additional imagery such that age relationships between the cycloids can be established.

The average values for the mechanical parameters found for all fits in Table 3.2 are 67 kPa for the initiation stress, 47 kPa for the propagation stress, and 7.0 km/hr for the propagation speed. For only the LibO fits, the average initiation stress is 66 kPa and the propagation stress is 43 kPa. These values are similar to those reported by previous authors (Hoppa et al. 2001; Hurford et al. 2007a). The initiation stress is low compared to the tensile strength of terrestrial ice: ~1MPa (e.g. Schulson 2001). If Europa's ice shell is thickening over time, induced global, uniform, tensile stresses (Nimmo 2004) may combine with tidal stresses to reach these higher values. In that case, the diurnal stress would be a small modulation that controls the orientation of the total stress. The crack propagation speeds we find are also low; cracks in ice propagate at near the Rayleigh wave speed: 2 km/s (Freund 1990). However, it has been proposed that cycloidal arcs

form as a concatenation of small segments (Lee et al. 2005). In this hypothesis, an individual fracture segment would propagate quickly but only over a short distance because it is restricted by its penetration depth (Lee et al. 2005), which is limited by the tensile strength and rheological parameters of the ice (Rudolph and Manga 2009). As the stress field changes, a new segment forms at the tip of the previous segment in order to relieve stress. The speed we find would then reflect the rate of change of the stress field and represent an average propagation speed. Some crevasses in Antarctic ice sheets and alpine valley glaciers exhibit this type of episodic propagation behavior, which leads to low average propagation speeds (e.g. Bassis et al. 2005).

Marshall and Kattenhorn (2005) point out that the dormant end of a cycloidal arc would experience both normal and shear stresses as the stress field changes in magnitude and direction. They propose that the shear stress initiates a tailcrack at the end of the arc, thereby creating a cusp. Although the perturbed near-tip stress field thus governs cusp formation and the initiation angle of the subsequent arc, once the crack propagates away from the cusp, its path is likely dictated by the maximum tensile (tidal) stress. Marshall and Kattenhorn (2005) find that cusps along some cycloids appear more consistent with a tailcrack model than the standard cusp formation model of Hoppa et al. (1999a, 2001), although Marshall and Kattenhorn (2005) did not attempt to model an entire cycloid. In addition, the influences of obliquity and/or physical libration on the expected characteristics of cycloids were not considered. In both cusp formation models, the majority of the cycloid is formed in response to the tensile tidal stress so our cycloid fits should still offer useful constraints on the nature of the stress field even if cusp formation is shown to be a more complex process than we assume here. However, if a new arc is generated via tailcrack formation, we are imposing an unnecessary restriction by requiring the initiation angle of the new arc to be perpendicular to the maximum tension.

It is interesting to note that the best fits to a given cycloid produced with different tidal models can have different propagation directions. Without obliquity, the concavity of the arcs is linked to the propagation direction (Hoppa et al. 2001). Using this criteria, Cilicia, Sidon, EQ1, and EQ3 should all have propagated west to east (W2E), while Delphi and EQ2 should have propagated east to west (E2W). With the addition of obliquity, the best fit to EQ2 is actually a W2E-propagating crack. Using the LibO model, the best fits to Delphi, EQ3, and Sidon also propagate the opposite direction from the original predictions. Given that our cycloid fits strongly support both obliquity and physical libration, we conclude that the propagation direction of a cycloid cannot be determined simply by the concavity of its arcs. This likely has important implications for the interpretations of cycloid characteristics such as the multiple branches or splays observed along some cycloids (Sarid et al. 2004; Marshall and Kattenhorn 2005).

A major difference between our fitting procedure and the work presented in Hurford et al. (2007a, 2009a) is that we do not vary the mechanical parameters for different arcs of a cycloid, thereby reducing the number of free parameters. Our OBLQ model produced results comparable in quality to those of Hurford et al. (2007a), without obliquity, for the southern hemisphere cycloids. However, we fit five arcs of Delphi using six free parameters whereas Hurford et al. (2007a), who fit only four arcs, used a different set of mechanical parameters for each arc for a total of 13 free parameters. Our six-parameter OBLQ fits to Sidon and Cilicia are also comparable to those of Hurford et al. (2007a), which required 19 free parameters for Cilicia and 28 for Sidon. Achieving

comparable fits with far fewer parameters means that our fits are much more robust.

Hurford et al. (2009a) presented a preliminary obliquity fit to EQ1 that is qualitatively better than our six-parameter OBLQ fit but required 30 free parameters. In addition, we are now able to reproduce the ninth arc of EQ1. Using the OBLQ model, the values we find for obliquity and formation longitude differ from those used for the Hurford et al. (2009a) fit by ~5%; the spin pole directions differ by ~10%. These differences mainly arise because we obtained the fit in Hurford et al. (2009a) by manually changing parameters by discrete amounts restricting the possible solutions. While both studies successfully identified the best region of parameter space for reproducing this cycloid, our improved methodology allowed for thorough exploration of the parameter space, and thus, more precise determination of the best fit parameters. Such differences are important given that small deviations in the value of the obliquity, for example, lead to large variations in tidal heating.

3.6 Conclusions

We have shown that tidal models including obliquity significantly improve fits to observed cycloids in the southern hemisphere and in the equatorial region of Europa. Physical libration combined with obliquity further improves the fits and is the preferred tidal model based on our statistical analysis. Fits using this model indicate large and variable values for obliquity, spin pole direction, and libration amplitude. The values for libration phase cluster near 0° implying that the librational motion tracks the tidal bulge. All fits do require longitude migration, presumably due to non-synchronous rotation, although stress from non-synchronous rotation is not indicated in most fits. Models including fast precession (RateO and LibRateO) are not supported.

These results lead us to several conclusions: (1) At the time these cycloids formed, Europa's obliquity and physical libration were non-zero, large enough to affect the formation of tidally-driven tectonics, and variable on short geologic timescales. The precession rate of the spin pole was likely slow compared to the formation timescale of a cycloid. (2) The large and variable values we find for obliquity and libration are best explained by the presence of an ocean (decoupling the shell from the solid interior) at the time of cycloid formation. There is also a large independent body of evidence for an ocean existing at present. (3) These cycloids did not form where we currently observe them. Thus, non-synchronous rotation is implied even though stress from NSR does not significantly improve fits. (4) When obliquity and physical libration are included, the formation model initially described by Hoppa et al. (1999a, 2001) is successful at reproducing cycloids in detail, even vertical-trending or equatorial cycloids, without arbitrarily varying the mechanical parameters for each arc. However, the formation direction of a cycloid cannot be determined merely by the concavity of its arcs when these tidal effects are included.

These results may allow more accurate estimates of tidal heating, more complete modeling of the gravitational interactions among Jupiter's large satellites, and better interpretation of the tectonic record. Looking forward, measuring Europa's current obliquity and libration via spacecraft or Earth-based techniques could confirm the results of this study or reveal that Europa's rotation state has changed significantly since cycloid formation. The large and variable values we find for obliquity may have interesting implications on Europa's thermal-orbital history; perhaps the ice shell has undergone

periods of tidally-induced warming (when obliquity was high) and cooling (when obliquity was low) thus altering the stress state of the shell over time. The addition of uniform tensile stress due to cooling of the ice shell could combine with the low diurnal stress values indicated by our work to induce cycloid formation. We expect that a better understanding of the fracture processes that produce cycloids will be a key to further advances in our understanding of Europan cycloid formation. Our work supports a tidal formation model, but even as we have improved fits we still find very low values for crack propagation speed and the stress required to initiate fractures. The coupled problem of a diurnally-varying tidal stress field and dynamic crack formation and propagation, which would include such effects as stress relief due to cracking, would be a useful albeit formidable undertaking. Adding the vertical dimension to fracture modeling of cycloids may also prove instructive.

3.A1 Cross-correlations between fitting parameters

We computed the R^2 correlations between each of the fit parameters using data from all applicable models (Table. 3.A1) and the two best tidal models – OBLQ and LibO (Table 3.A2). Almost all parameters are uncorrelated or weakly correlated, having R^2 values of less than 0.2. The parameter sets with R^2 values higher than 0.2 are the same whether we use all the data or only the data from the best tidal models. In both tables, R^2 values between 0.2 and 0.4 are highlighted in yellow and values greater than 0.4 are in green. Only one parameter set had an R^2 higher than 0.5, implying that there are no significant trade-offs between these parameters.

Several of the higher R^2 values involve the NSR stress, including the highest R^2: NSR stress and the spin pole direction, which has a value of 0.6159. In this case, we are using the spin pole direction corresponding to the minimum amount of longitude migration. Recall that degeneracy between these two parameters allows us to modulate both by 180° and get the same stresses. If we instead use the minimum value of the spin pole direction, the R^2 between NSR stress and SPD drops to 0.0615 – not a significant correlation.

Table 3.A1: Cross-correlations using parameter values from all tidal models

R^2	Obliquity	Spin pole direction (SPD)	NSR stress	Crack initiation threshold	Crack propagation threshold	Propagation speed	Libration amplitude	Libration phase	Precession rate
Minimum longitude migration	0.0256	0.0343	0.0221	0.1005	0.0469	0.1238	0.2301	0.0827	0.0363
Obliquity		0.0281	0.0206	0.0017	0.0028	2.00E-06	0.3198	0.302	0.184
Spin pole direction (SPD)			0.6159 (-)	0.0019	0.0065	0.2684	0.0114	0.0307	0.032
NSR stress				0.0829	0.4553	0.2223			
Crack initiation threshold					0.0021	0.0162	0.4346	0.0145	0.2071
Crack propagation threshold						0.3175	0.0352	0.2176	0.0047
Propagation speed							0.0726	0.0931	0.0375
Libration amplitude								0.433	0.0046
Libration phase									0.0186

Table 3.A2: Cross-correlations using parameter values from the best tidal models

R^2	Obliquity	Spin pole direction (SPD)	Crack initiation threshold	Crack propagation threshold	Propagation speed	Libration amplitude	Libration phase
Minimum longitude migration	0.0564	0.002	0.1993 (-)	0.0008	0.0022	0.2008	0.0351 (-)
Obliquity		0.1661	0.0309 (-)	0.0305 (-)	0.0104	0.2388	0.3817 (-)
Spin pole direction (SPD)			0.0009	0.0254	0.2507	.0002 (-)	.0267 (-)
Crack initiation threshold				0.0113	0.0005	.5404 (-)	0.0001
Crack propagation threshold					0.4392	.0127 (-)	0.2464
Propagation speed						0.0598	.0559 (-)
Libration amplitude							.4407 (-)

Chapter 4: The influence of Io-raised tides on Europa

4.1 Introduction

Incorporating the effects of a more complex rotation state significantly improved fits to observed cycloids, as described in Chapter 3. These fits required longitude translation, which is the strongest geologic evidence that Europa's shell rotates non-synchronously. However, cycloid EQ2 is the best fit to any cycloid in the study, with a χ^2 of only 14, and requires only 3° of longitude translation. Perhaps this is merely a coincidence, but it leaves open the possibility that cycloids did form at their present locations, and we are unable to fit them because we are still neglecting a significant contribution to the stress field.

Diurnal tidal stresses on Europa are calculated by subtracting stress associated with the average (or static) tidal shape due to Jupiter's gravitational field from the instantaneous shape, which varies as Europa moves through its eccentric orbit. In other words, it is the change of shape away from average that generates tidal stress. One might expect tidal contributions from the other large moons of Jupiter to be negligible given their size and the height of the tides they raise on Europa compared to Jupiter's mass and the height of the tide it raises on Europa. However, what matters for tidally-induced stress is not how large the Io-raised bulge is compared to the Jupiter-raised bulge but rather the differences between the instantaneous and static bulges in each case. For example, when Europa is at apocenter, Jupiter raises a tide 30m lower than its static tide. At the same time, Io raises a tide about 0.5m higher than its static tide. Hence, the change in Io's tidal distortion is about 2% of the change in the Jovian distortion when Europa is at apocenter.

Here, we assess whether Io-raised tides on Europa can affect the formation of cycloids. Building upon the tidal stress equations developed in Chapter 2, we first derive expressions for the contribution of the Io-raised bulge to Europa's diurnal surface stress. We then determine the change in the magnitude and direction of the maximum tensile stress when Io's contribution is added. Finally, we assess how this additional stress would alter the formation of cycloids by (1) creating global maps of hypothetical cycloids and (2) adding stress from Io to the cycloid simulator described in Chapter 3. We find that, although there is a noticeable change in the paths of some hypothetical cycloids, adding Io-derived stresses does not significantly alter the results of the cycloid modeling presented in Chapter 3.

4.2 Calculating Io's contribution to Europa's diurnal stress

The equations for tidal stress in a thin elastic shell, developed in Chapter 2, depend on the distance between Europa and the tide-raiser and the angular distance from a location on Europa's surface to the tidal bulge. In order to compute the tidal stress imposed by Io on Europa, we need to determine these values for both the average and instantaneous positions of Io and Europa over an orbit.

We use the guiding-center approximation (Murray and Dermott, 1999) to derive expressions for the relative locations of Io, Europa, and Jupiter. As shown in the schematic in Figure 4.1, we can use simple geometry and the Laws of Sines and Cosines to define several quantities. First, the distance between Io and Europa, *d*, is

(4.1) $d^2 = r_E^2 + r_I^2 - 2r_E r_I \cos(\gamma)$

where γ, the angle between Europa and Io is given by

(4.2) $\gamma = f_I - f_E = (2e_I \sin(2nt) + 2nt + \pi) - (e_E \sin(nt) + nt)$

Here, we define *nt* as the mean motion of Europa. The term describing Io's orbital position (f_I) differs from that of Europa (f_E) because Io's orbital period is half of Europa's, leading to the 2*nt* term, and Io is at apocenter when Europa is at pericenter.

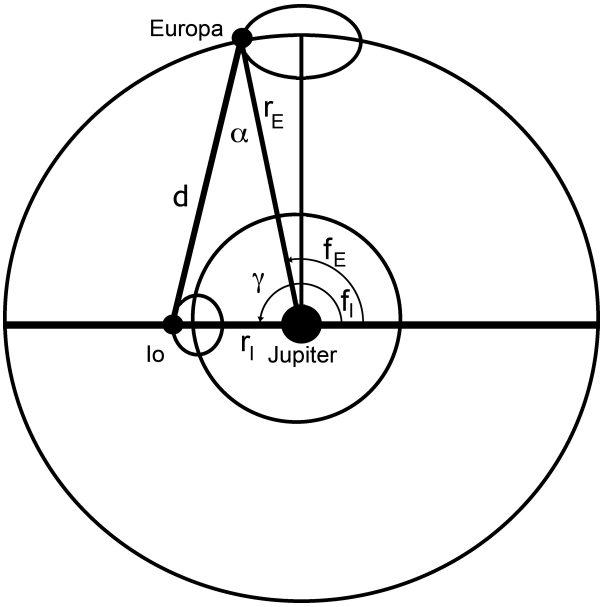

Figure 4.1: A schematic of Jupiter, Europa, and Io using the guiding-center formulation. Geometric quantities relevant for calculating the locations of the instantaneous bulges raised by Jupiter and Io are marked.

Because the eccentricities (e_E and e_I) are small, we can use an approximation for the distances between the moons and Jupiter such that

(4.3a) $r_E = a_E(1-e_E\cos(nt))$
(4.3b) $r_I = a_I(1-e_I\cos(nt))$

where a_E and a_I are the semimajor axes of Europa and Io, respectively. Using these expressions, the distance between Io and Europa at a given time, *t*, can be written as

(4.4) $d^2 = r_E^2 + r_I^2 - 2\cos(\gamma)a_E a_I(1-e_E\cos(nt))(1-e_I\cos(nt))$

This distance is used to compute the instantaneous tide. To determine the primary tide, we calculate the average distance between Europa and Jupiter over an orbit.

For both Io and Jupiter, the primary bulges are located at 0° longitude. The longitudes of the instantaneous bulges raised by Io and Jupiter, ω_I and ω_J are respectively determined by

(4.5a) $\omega_I = -2e_E\sin(nt) + \alpha$
(4.5b) $\omega_J = -2e_E\sin(nt)$

where α, the angle between Jupiter and Io, is given by

(4.6) $\alpha = \text{acos}(-r_I \sin(\gamma)/d)$

The colatitudes of the primary bulges are located at the equator. However, the instantaneous bulges raised by Io and Jupiter are given by

(4.7a) $\lambda_I = \pi/2 - \varepsilon \sin(nt + \varphi - 2e_E \sin(nt))$
(4.7b) $\lambda_J = \pi/2 - \varepsilon \sin(nt + \varphi - 2e_E \sin(nt) + \alpha)$

The expression for the colatitude of the Jupiter bulge has an extra - $2e_E$*sin(nt) term that is not present in Eq. 2.3a for the colatitude of Jupiter's bulge. Without obliquity, the eccentricity-driven bulge librates in longitude but is always located on the equator. With obliquity, the eccentricity-driven bulge can actually move of the equator depending on the spin pole direction. Because Europa's eccentricity is small, this correction is also small. We include it here to calculate the bulge longitudes of both Io and Jupiter for completeness. Removing this term did not alter our results.

Using these equations, we can calculate the diurnal tidal stress following the formulation in Chapter 2, in which we convert the primary and instantaneous components to a common coordinate system and subtract out the effects of the primary tide.

4.3 Effects on the global stress field

Due to the mean motion resonance between Io and Europa, the two moons are at closest approach when Europa is at apocenter. Therefore, the magnitude of the tidal stress when Io's contribution is included changes most appreciably when Europa is at apocenter. The top row of Figure 4.1 shows contours of the change in magnitude of the maximum tensile stress at apocenter when Io's contribution is included. With only eccentricity (left-most panel), the largest increases in tensile stress are at 0° and 180°, the locations of the tidal bulges. Europa is at apocenter, so the instantaneous tide raised by Jupiter is lower than average here. Hence, Europa would become more spherical leading to compression at the bulges. However, the bulge raised by Io is larger than average at this time, so the two effects destructively interfere causing Europa to become slightly less spherical than it would have from Jupiter tides alone. The net change in stress at the bulges (longitude 0°/180°) with Io's contribution is positive; the stress is more tensile than it otherwise would have been. The tidal stress magnitude at this time differs from the Jupiter-only case by 2% percent. When Europa's obliquity is included, the pattern of stress change varies slightly depending on the spin pole direction; the contours representing the largest increase in tensile stress (red in Figure 4.1) are located at the locations of the tidal bulges, which may now be off the equator as in the top right panel of Figure 4.1.

At pericenter and apocenter, the instantaneous tidal bulges raised by Io and Jupiter point directly toward Jupiter and are thus longitudinally aligned with the static bulges. The locations of the instantaneous bulges then change throughout the orbit. The Jupiter-raised bulges migrate in longitude by $\pm 2e_E$ from the location of the static bulge.

Using the equations developed in section 4.2, we find that the angle subtended by the Io-raised bulges is more than an order of magnitude larger, ~40°.

The location of the instantaneous bulge to a given point on the surface affects the direction of the principal stress in that region. The bottom row of Figure 4.1 shows contours of the difference between the direction of maximum tensile stress with and without Io's tidal contribution. The difference is least when the Io and Jupiter bulges are aligned (pericenter and apocenter, not shown) and greatest when they are maximally misaligned, when Europa is at 3/8 past pericenter and 1/8 past apocenter. The largest deviation at those times is about half a degree without obliquity (bottom left) and as much as 3° with obliquity (bottom center and right).

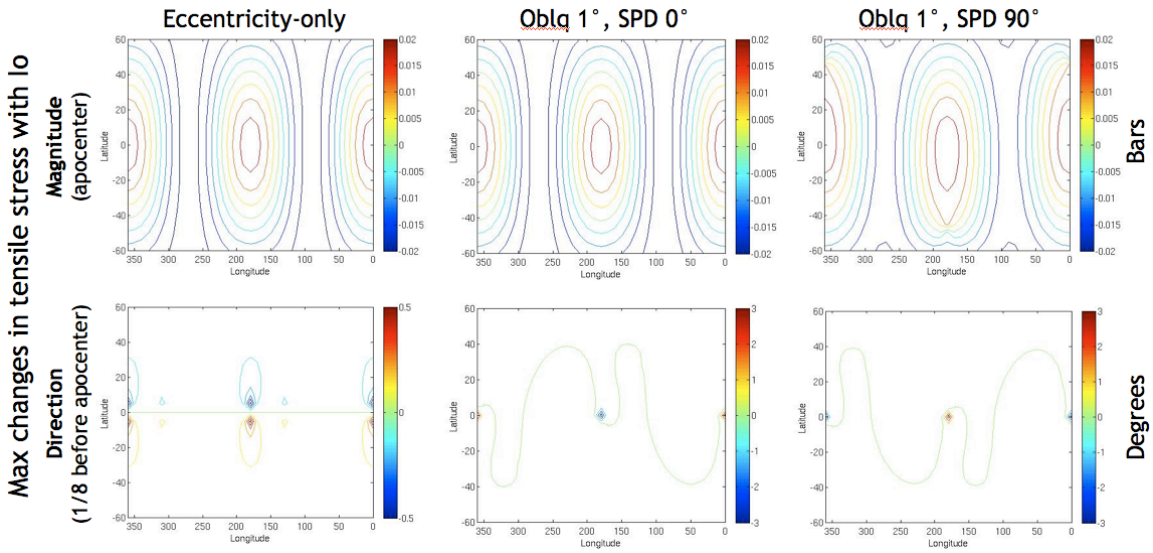

4.4 Effect on cycloid formation

To determine the effect of Io-raised tides on cycloid formation, we first created global maps of hypothetical cycloids. To generate these cycloids, we assume a starting stress of 50 kPa, a stopping stress of 40 kPa, and a speed of 5 km/hr, which are similar to the values identified in the cycloid fitting work described in Chapter 3. We then propagate each crack in a direction perpendicular to the direction of maximum tension. Cycloids were generated at every 15° of longitude and 10° of latitude from 75°S to 15°S and from 15°N to 75°N. Figure 4.2 shows hypothetical cycloids propagating from east to west without the effects of Io (red) and with Io (green). The left panel uses eccentricity tides, while the right panel also includes obliquity (ε=1°; φ=0°). In both cases, there are cycloids whose paths are slightly altered when Io is included, but it does not dramatically change the global pattern or any individual cycloid paths.

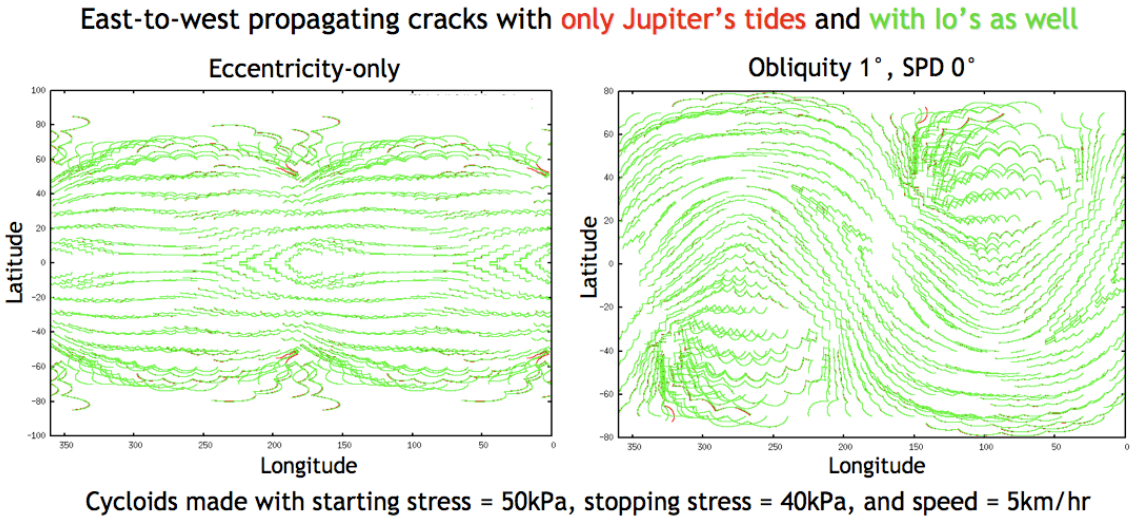

Figure 4.2: Hypothetical cycloid paths with only Jupiter's tides (red) and with Io's tides as well (green). The paths differ only slightly in some areas.

In addition to these global maps, we also incorporated Io's tidal contribution into the cycloid simulator described in Chapter 3. We began a simulation with the parameter values that gave the best overall fit – cycloid EQ2 with obliquity, physical libration, and longitude migration (see Table 3.3 for the exact values). The result of this simulation is shown in Figure 4.3. The EQ2 data is shown in black, the original best fit is shown in red, and the best fit with Io's tidal contribution is shown in green. The fits are nearly identical, and the chi squared is not significantly improved. The amount of longitude migration is also unchanged. However, the best-fit values of obliquity and physical libration do differ from those of the Jupiter-only fit. The obliquity changes from 0.9285° to 0.9456°, and the SPD changes from 317.02 to 318.18. Based on the error bars derived in section 3.3 (Table 3.2), these seemingly small differences are actually many sigma. Although these results do not change the conclusions of the cycloid modeling work presented in Chapter 3, accounting for Io's tidal contribution could alter the exact values of the rotational parameters for each cycloid.

4.5 Conclusions

We find that incorporating Io's tidal effects makes very small differences in the magnitude and direction of the principal surface stresses on Europa. Our analysis shows that hypothetical cycloids paths are slightly altered when Io tides are incorporated into calculations of the tidal stress field, and the best-fit parameters of modeled cycloids may also be affected. However, this contribution does not significantly affect our previous modeling results; good fits to observed cycloids still require obliquity, physical libration, and longitude translation.

Ganymede is larger than Io and should also raise tides on Europa. However, the formulation we use to assess tidal stresses generated by Jupiter and Io may not be valid for Ganymede. Recall that the Jupiter-raised bulges librate only a few degrees about the sub-Jupiter point and the Io-raised bulges move through ~40°. Because Ganymede orbits

exterior to Europa, the bulge it raises circulates through all 360° of Europa's surface. Hence, there is no primary bulge. A circulating bulge would have a distinctly different effect on the tidal stresses on Europa, but more sophisticated techniques are likely needed to adequately address this process.

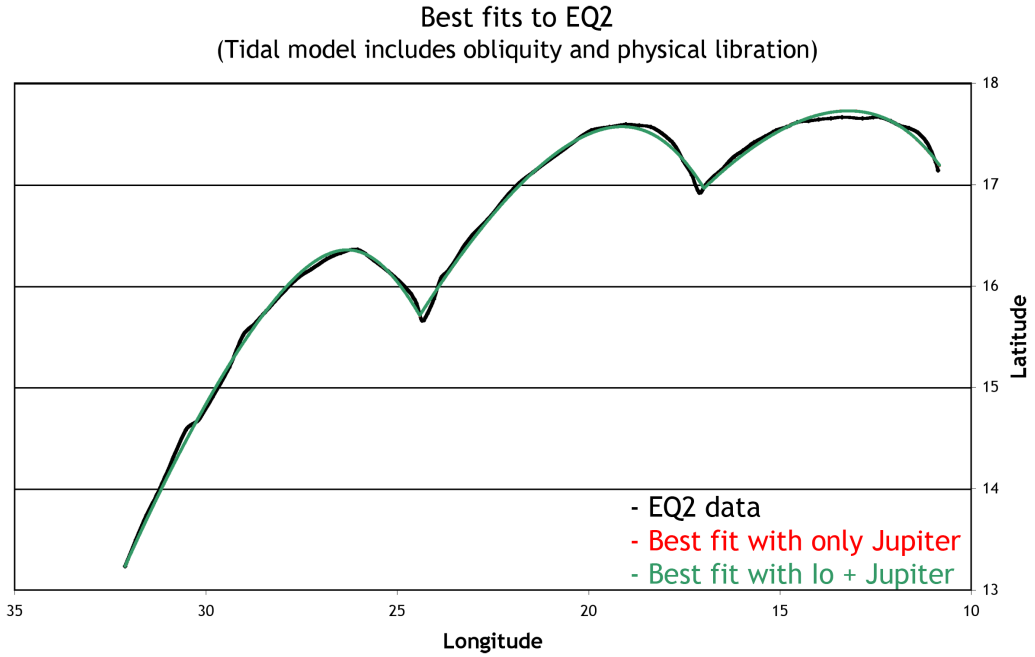

Figure 4.3: The best fits to EQ2 using the cycloid simulator described in Chapter 3. The best fits with only Jupiter's tides (red) and with Io's contribution added (green) are indistinguishable. The best-fit parameters are slightly different, however.

Chapter 5: Interpreting strike-slip faults using tidal walking

5.1 Introduction

Strike-slip displacement on Europa was first identified by Schenk and McKinnon (1989) within a region of boxy lineaments called "The Wedges". Later, Tufts et al. (1999) identified extensive strike-slip displacement along a cycloid called Astypalaea Linea. The appearance of such strike-slip displacement was puzzling until it was considered within the context of tides. Europa's eccentric orbit leads to daily changes in tidal stress, which may then drive tectonics. Hoppa et al. (1999c, 2000) developed a tidal-tectonic model for the formation of strike-slip faults, dubbed "tidal walking", in which tidal stresses acting on a crack lead to net displacement along the crack during each tidal cycle. In particular, throughout an orbit, the tidal stress at a crack cycles through periods of tension, then shear, then compression, and then shear in the opposite direction. Although there are two periods of shear, displacement along the fault mainly occurs while the crack is open; when the crack is closed, friction restricts or even prohibits sliding. The result is a net displacement due to shear stress applied during the open phase (i.e. shear that occurs after a period of tension). Based on this model, the net sense of slip (right or left lateral) along a crack can be predicted if the latitude, longitude, and azimuth of the crack are known. The global pattern of strike-slip motion produced by eccentricity-driven tides has the following characteristics (Hoppa et al. 1999c, 2000): only left lateral faults form above 35°N, only right lateral faults form below 35°S, and between these regions, both right and left lateral faults form with the slip-direction depending on the longitude and the azimuth of the crack. A limited survey of strike-slip faults on Europa showed that faults do tend to follow the pattern predicted by the eccentricity-only tidal walking model (Hoppa et al., 2000). In cases where predictions did not match observations, longitudinal displacement, presumably due to non-synchronous rotation, could alleviate the mismatch.

Sarid et al. (2002) conducted a comprehensive mapping of strike-slip faults in the Regional Mapping imagery taken by the Galileo spacecraft at ~250 m/pixel, which covered two broad swaths extending from about 70°N to 70°S. RegMap02 is in the leading hemisphere, centered at ~80°W and extending about 10° on either side. RegMap01 is in the trailing hemisphere at ~220°W with a southern extension closer to 180°W. They also included a region directly north of RegMap01 that was imaged separately. Examples of faults found in the survey are shown in Figure 5.1 from the north trailing hemisphere (Fig. 5.1a) and south leading hemisphere (Fig. 5.1b). For each of the 192 mapped faults (Fig. 5.2 and Appendix 5.A1), Sarid et al. (2002) recorded the latitude, longitude, azimuth, amount of displacement, and sense of slip. To determine whether the strike-slip observations supported the tidal walking model, they used the global predictions of slip direction from Hoppa et al. (1999c), which indicated that only left lateral faults form at 45°N and 60°N, only right lateral faults form at 45°S and 60°S, and there is a mixture of right and left lateral faults at intermediate latitudes for which the prediction depends on longitude and crack azimuth. Using these predictions to match specific faults was challenging because the longitudes of the two survey regions fell in between the longitudes at which the predictions were determined (every 30°). There were also many faults with latitudes intermediate to the prediction latitudes. However, relying on only the general pattern, Sarid et al. (2002) showed that the observations and

theoretical predictions did not match. In the trailing hemisphere, right lateral faults were observed as far north as 60° and very few left lateral faults were observed just south of the equator. In the leading hemisphere, the mixture of right and left lateral faults extended far south although the number of strike-slip observations in this region was limited due to pervasive chaos.

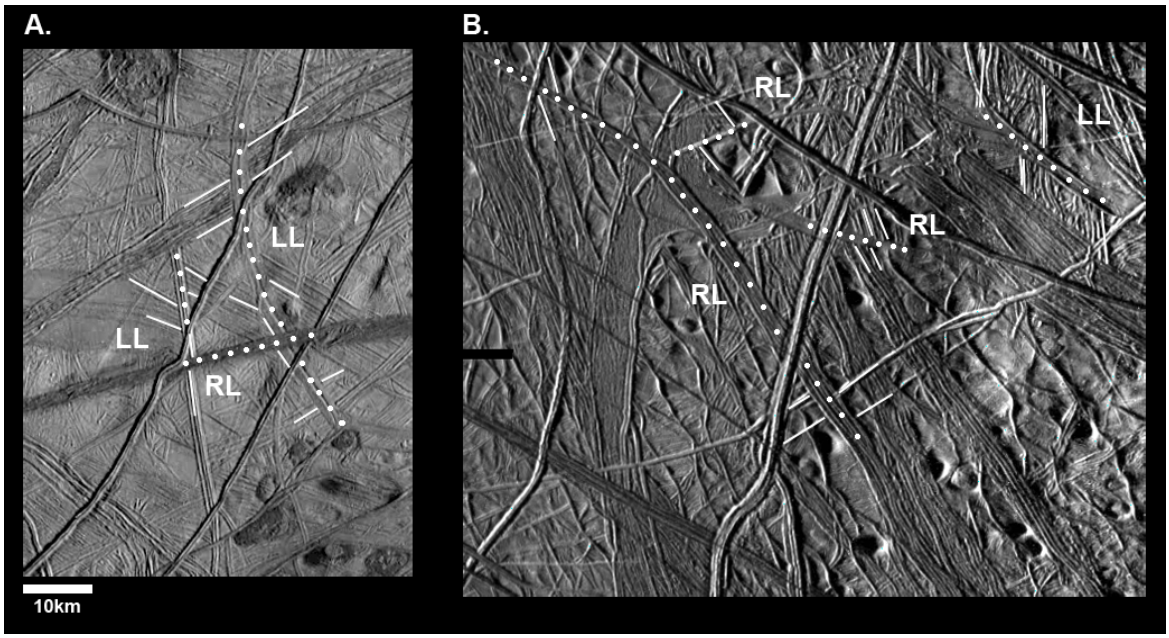

Figure 5.1: Examples of strike-slip faults identified in the survey by Sarid et al., (2002) in the (a) north leading hemisphere (orbit e15-01, image s0449961865) and the (b) south leading hemisphere (orbit e17-02, image s0466676901). White dots trace out the fault along which slip has occurred. Offset features along each fault are highlighted with thin white lines, and the slip direction is noted. Maps of all faults included in the survey are shown in Figure 1 of Sarid et al., 2002.

Sarid et al. (2002) concluded that, based on the general pattern of strike-slip faults expected to form in response to eccentricity-driven tides, ~30° of polar wander had occurred since the majority of the faults formed, causing the pattern to appear too far north in one hemisphere and too far south in the other. In addition, they inferred that polar wander occurred slowly enough that the induced stresses could viscously relax and not impose surface stresses that would otherwise swamp the tidal stress expected to generate these strike-slip faults. The distributions of chaotic terrain and other non-tectonic features also appear to have some oblique antipodal symmetry (Riley et al. 2000; Greenberg et al. 2003) bolstering the polar wander interpretation. If Europa's ice shell is mechanically decoupled from the interior, modest shell thickness variations could induce polar wander. Ojakangas and Stevenson (1989a) showed that temperature differences between the equator and poles could lead to thickness variation in the ice shell, and ultimately, reorientation of thicker ice to the equator. However, any process that locally thins the ice shell could theoretically drive polar wander, moving the thinned region poleward.

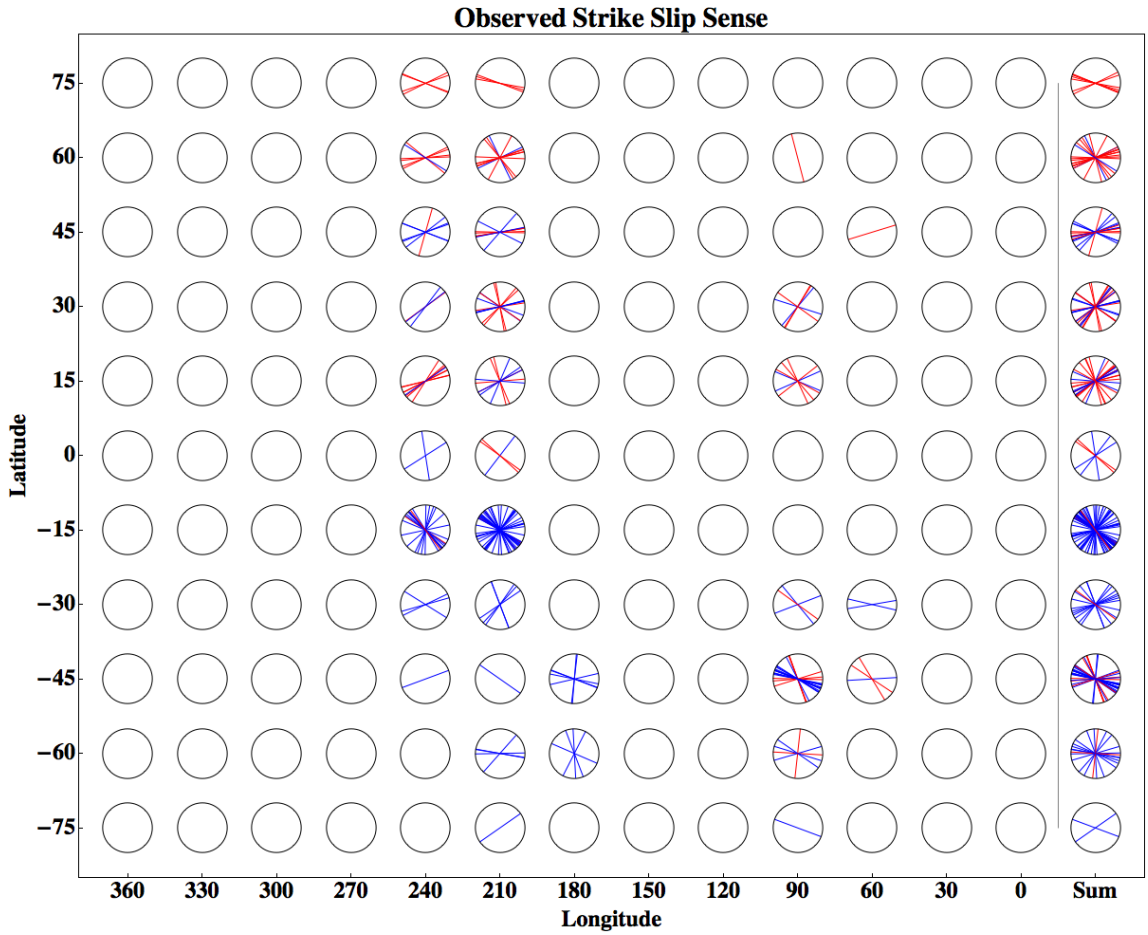

Figure 5.2: Observed strike-slip faults from Sarid et al. (2002), binned according to their current latitudes and longitudes for comparison with global predictions. Blue lines represent right lateral faults while red shows left lateral faults. The azimuths of the lines correspond to the azimuths of the faults. At longitude 90° and latitudes 0° and 15°S, no faults were mapped due to extensive chaotic terrain. Longitudes that have empty bubbles at all latitudes were not mapped in the strike-slip survey because the image resolution was too low.

Since a more detailed comparison was not possible given the sparseness of the predictions, Sarid et al. (2002) did not fully address whether non-synchronous rotation was required to fit the strike-slip observations. However, there was an expectation that any discrepancy between model predictions and observations that was not corrected by polar wander could be accounted for with non-synchronous rotation. In fact, a more detailed comparison using such a model may not offer much additional insight. Polar wander would change the azimuths of displaced faults, in addition to their latitudes, unless the faults happen to fall exactly along the polar wander rotation axis. Determining the extent of azimuth change for a given fault is further complicated if non-synchronous rotation occurs along with slow polar wander thereby moving faults out of alignment over time.

The stress field used to predict these strike-slip patterns incorporated only the

tidal effects of Europa's forced eccentricity. As described in section 1.2, there are theoretical arguments supporting the idea that Europa has a small but non-negligible obliquity and undergoes a physical libration. In addition, the detailed fits to individual cycloids greatly improve when the tidal model includes obliquity and libration, as shown in Chapter 3 (see also, Hurford et al., 2009a; Rhoden et al., 2010). Specifically, the obliquities ranged from 0.32 – 1.35°, and the libration amplitudes varied from 0.72 – 2.44°. The libration phases mainly clustered between -6.04° and 17.72°. These findings are consistent with the theoretical predictions in the case that Europa has a subsurface ocean separating the ice shell from the interior. There was almost no signal of fast spin pole precession within cycloid shapes, suggesting that either precession is slower than expected or cycloid formation is not sensitive to small changes in spin pole direction. Stress from non-synchronous rotation (NSR) did little to improve cycloid fits although longitude translation, presumably due to NSR, was required to obtain good fits with all models (Rhoden et al., 2010).

Here, we investigate the influence of obliquity on fault slip-direction and reevaluate the polar wander interpretation of observed strike-slip faults. We first update the global predictions from Hoppa et al. (1999c, 2000), which incorporated only eccentricity, because the predictions for the region in which both right and left lateral faults can form were incorrect (Section 5.3.1, Appendix 5.A2). We next produce global predictions that incorporate obliquity. Finally, we predict the slip-direction for each strike-slip fault recorded by Sarid et al. (2002) using tidal models with and without obliquity, physical libration, and longitude migration. Consistent with theoretical expectations and results from our previous cycloid modeling (Chapter 3 and Rhoden et al., 2010), we find that a tidal model including obliquity of at least 1.2°, along with longitude migration, can predict the slip-directions of all observed features in the survey. Adding physical libration to the obliquity model increases the number of correctly predicted features at their current longitudes, but cannot account for all observations. Applying a tidal model that incorporates obliquity alleviates the need to invoke polar wander in order to reconcile the tidal walking hypothesis with observations, although both scenarios require longitude migration presumably due to non-synchronous rotation.

5.2 Methodology

In the tidal walking hypothesis, daily changes in tidal stress control the opening and closing of pre-existing faults at the surface and the direction of the net shear displacement along the faults. To calculate tidal stress, we use the equations for stress derived in Chapter 2. We first focus on the effects of obliquity, to determine if the latitudinal variation in bulge location caused by obliquity can account for the latitudinal mismatch between theory and observations. We then add longitude translation or physical libration to determine whether either motion improves the predictions. We do not include any stress from non-synchronous rotation or polar wander when determining predictions of slip direction. In addition, we do not address the formation mechanism of the preexisting crack, only subsequent motion along the fault.

To determine the slip direction along a fault, we first specify the latitude and longitude of the fault, the fault azimuth, and the amount of obliquity and spin pole direction (SPD). There is degeneracy between spin pole direction and longitude such that the stress field is identical when both are modulated by 180°. Using these parameters, we

calculate the stress throughout an orbit, beginning at pericenter and ending at apocenter. We then evaluate the changes in stress over time using a tidal-walking model to determine the prediction for slip direction along the fault.

Figure 5.3 shows the normal and shear stresses plotted over one orbit for a fault with azimuth 120° at a longitude of 210° in the far north (Fig. 5.3a) and far south (Fig. 5.3b). When the normal stress changes from negative (compression) to positive (tension), shear displacement along the crack is encouraged. This corresponds to the "opening" phase described by Hoppa et al. (1999c, 2000). However, as long as slip can occur more easily during the tensile phase than during the compressive phase, the tidal walking model should still produce displacement even without physically opening the crack. The time at which this transition occurs is marked A in Figure 5.3a, and corresponds to a near maximum in right lateral shear stress, resulting in an initial right-lateral displacement, which then decreases over time until switching to left lateral shear (point B).

Because the local region of interest is connected to Europa's global ice shell, we conceptualize the sides of the fracture as two ice blocks pinned far from the location of the fracture. As the blocks distort under the influence of tidal shear stress, there is a competing elastic restoring force due to the ice shell's elasticity. Thus, as the right lateral shear stress decreases, the displacement on the fault also decreases (Fig. 5.3a). When the shear stress reaches zero, at point B, we would expect no displacement along the crack due to the elastic response of the shell. After point B, and until the fault closes (point C), the shear stress is increasingly left lateral. Therefore, we would predict left-lateral displacement along this northern hemisphere fault during the open phase. The opposite is true in the southern hemisphere (Fig. 5.3b) in which, after opening occurs, the left lateral shear stress decreases and then becomes increasingly right lateral resulting in a right-lateral fault. We can, therefore, use the shear direction at the time of closing to predict the slip direction along the fault. Although we treat the ice shell as elastic, which is probably appropriate at the surface when subjected to daily-varying stress, the tidal walking model assumes that some stress is slowly relaxed during the dormant phase causing the fault to retain a net displacement in each subsequent orbit (Hoppa et al. 1999c, 2000).

5.3 Results

5.3.1 Global strike-slip predictions

To examine the influence of obliquity on global strike-slip patterns, we determined the slip directions of faults at azimuths from 0 to 180° in increments of 1°, for every 30° of longitude, and every 15° of latitude from 75°N to 75°S; we tested obliquity values of 0, 0.5, and 1.0° with spin pole directions of 0, 90, 180, and 270°. If Europa's spin pole precesses quickly with respect to the accumulation of strike-slip displacement along faults, the fault displacements in the survey may reflect different spin pole directions. We therefore also computed the predictions for spin pole directions at every 30° combined. Finally, we examined the potential effects of longitude migration due to non-synchronous rotation by combining predictions at all longitudes.

a.

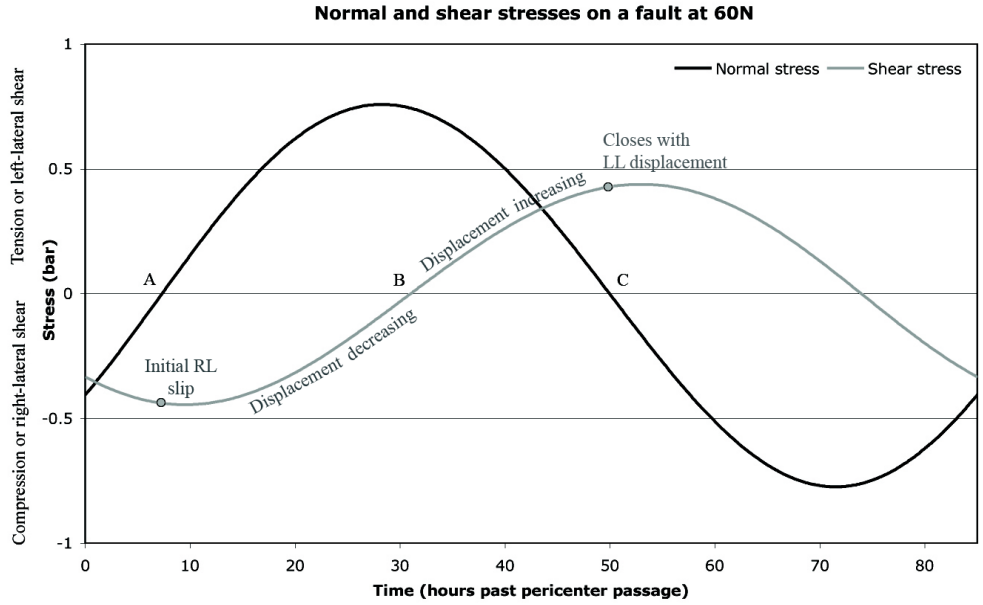

b.

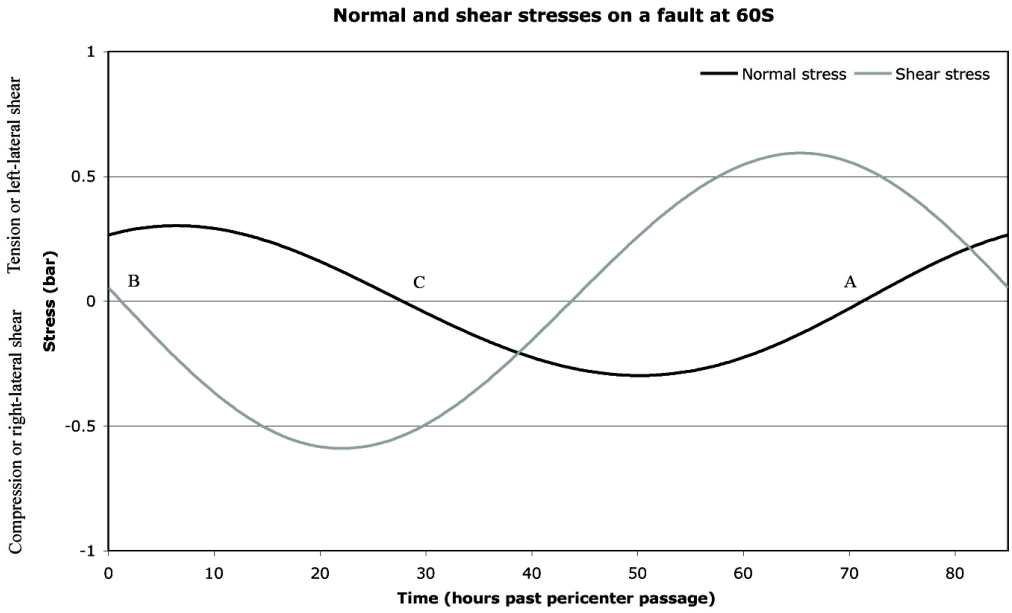

Figure 5.3: Stress change throughout one orbit on a fault of azimuth 120° at longitude 210° and latitude 60°N (a) or 60°S (b). The normal stress is shown in black, and the shear stress is grey. In the tidal walking theory, shear occurs more easily when the normal stress becomes tensile (i.e. greater than 0), which occurs at A, than when the normal stress becomes compressive, at point C. Between these times, the shear stress controls the displacement along the fault. The point at which the shear stress switches from decreasing right lateral to increasing left lateral (in case a; the opposite for case b) is marked as B. Since the northern fault (a) is subject to left lateral shear when the fault becomes compressive, it would exhibit left lateral displacement. The southern fault (b) should then be right lateral.

Figure 5.4 shows the global predictions for the eccentricity-only case (see also, Appendix 5.A2). Black represents fault azimuths that undergo left lateral slip, light grey represents right lateral slip, and white shows cases where no net slip is predicted. The white regions are difficult to discern since the prediction of no net slip tends to apply just at the azimuth separating predictions of right and left lateral fault motion. At the equator, these regions are slightly more visible and run nearly horizontal and nearly vertical. The last column of Figure 5.4 shows a combination of the predictions made at each longitude. Here, dark grey indicates that both right and left lateral faults form within the span of longitudes tested for a given crack azimuth. The overall pattern we find is the same as Hoppa et al. (1999c). In the region of mixed right and left lateral faults, our predictions differ because Hoppa et al. (1999c) incorrectly decomposed stresses along the crack when making their predictions. This error would probably not have changed the interpretation by Sarid et al. (2002) since it was based on the global pattern, but it would affect a more detailed analysis of near-equatorial faults (such as our analysis, described in section 5.3.2).

Figure 5.5 shows the global predictions for an obliquity of 1.0°, at each of the four SPDs (a-d) and for SPDs at every 30°combined (e). Plots using an obliquity of 0.5° are shown in Appendix 5.A3. The last column of each plot shows the predictions combined over all longitudes. Just as before, black signifies left lateral faults, light grey signifies right lateral faults, dark grey indicates that either type of fault can form, and white shows cases where we predict no net slip. These global prediction plots show that increasing obliquity creates increasing asymmetry in the fault pattern. Right lateral faults can form in the far north, left lateral faults can form in the far south, and the mixed regions are offset from the equator in different patterns depending on the spin pole direction. Considering these global prediction plots, it seems plausible that the observed pattern of strike-slip faults (Fig. 5.2) may be accounted for by inclusion of obliquity.

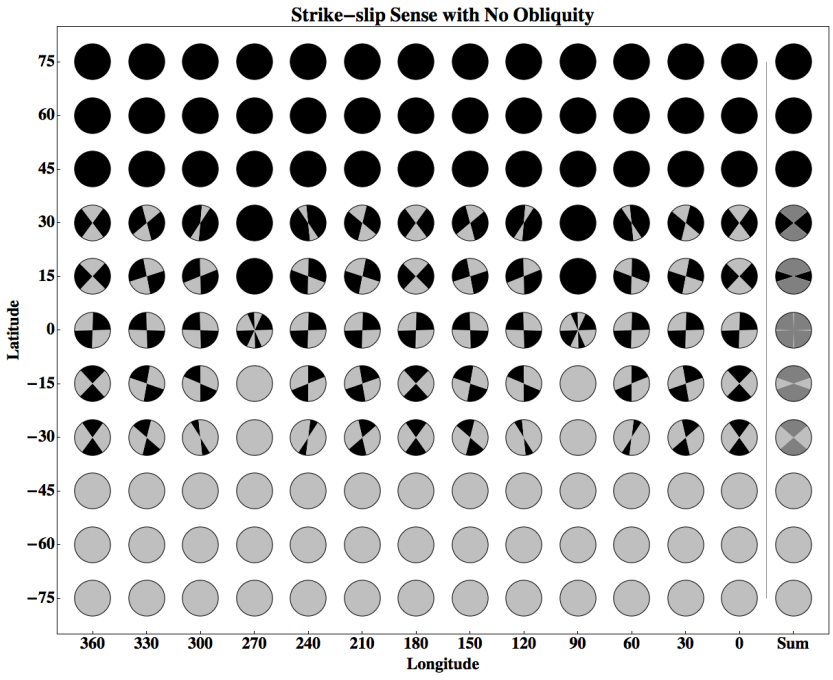

Figure 5.4: Predictions with zero obliquity. Black indicates crack azimuths along which we predict left lateral displacement; light grey represents right lateral fault azimuths, and white indicates that no net slip is predicted. The last column shows the predictions summed over all longitudes, in which dark grey represents azimuths that could display slip in either direction depending on their formation longitude.

Figure 5.5: a-e. Predictions with 1.0° obliquity at spin pole directions of 0° (a), 90° (b), 180° (c), 270° (d), and with SPDs at every 30° combined (e). In each plot, the last column shows the predictions at all longitudes combined. Black represents fault azimuths that will exhibit left lateral displacement, and light grey represents right lateral faults; dark grey indicates that either type of fault can form, and white shows cases where we do not predict any net slip.

a.

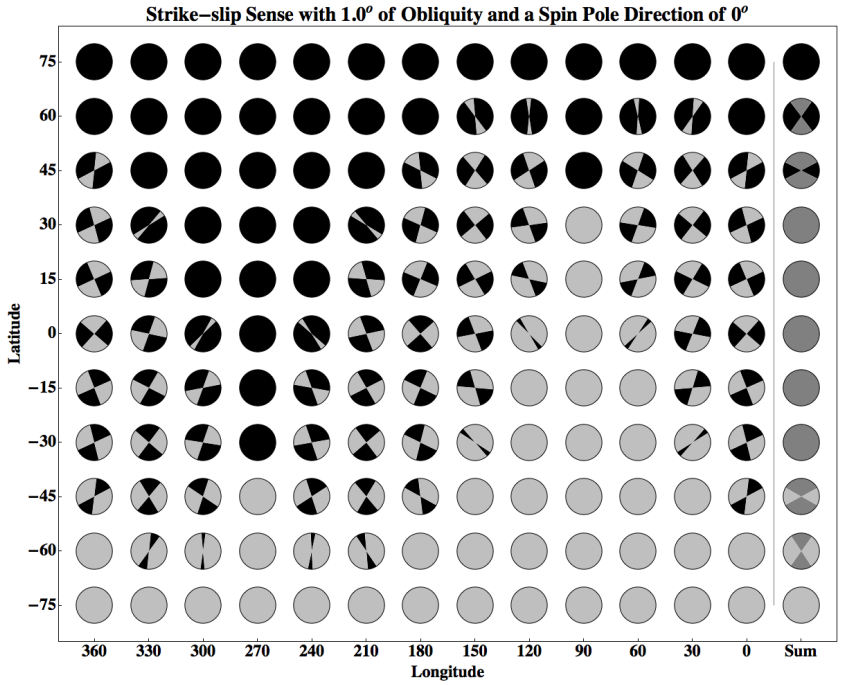

b.

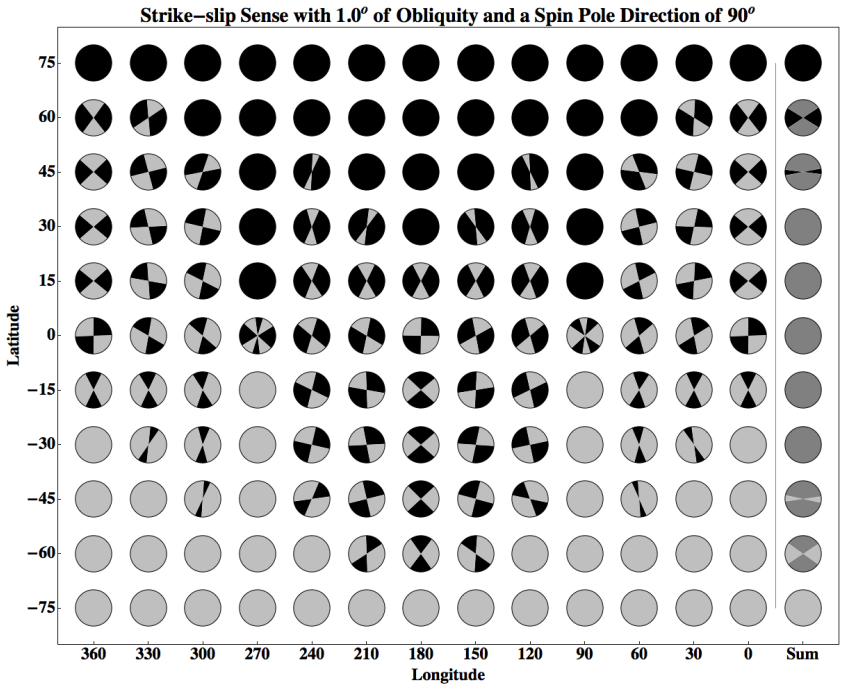

c.

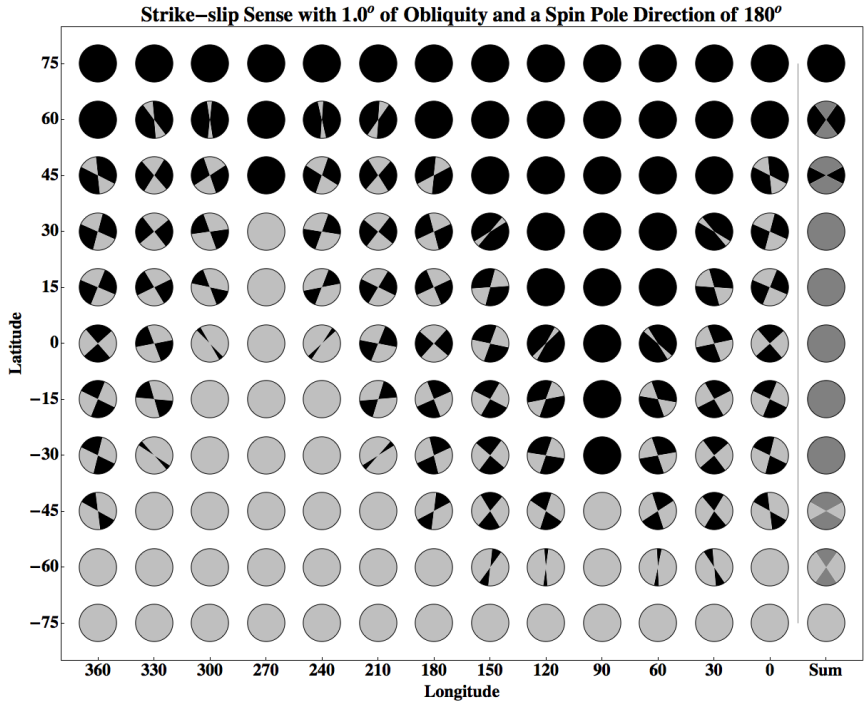
Strike−slip Sense with 1.0° of Obliquity and a Spin Pole Direction of 180°
Latitude
75
60
45
30
15
0
−15
−30
−45
−60
−75
360
330
300
270
240
210
180
150
120
90
60
30
0
Sum
Longitude

d.

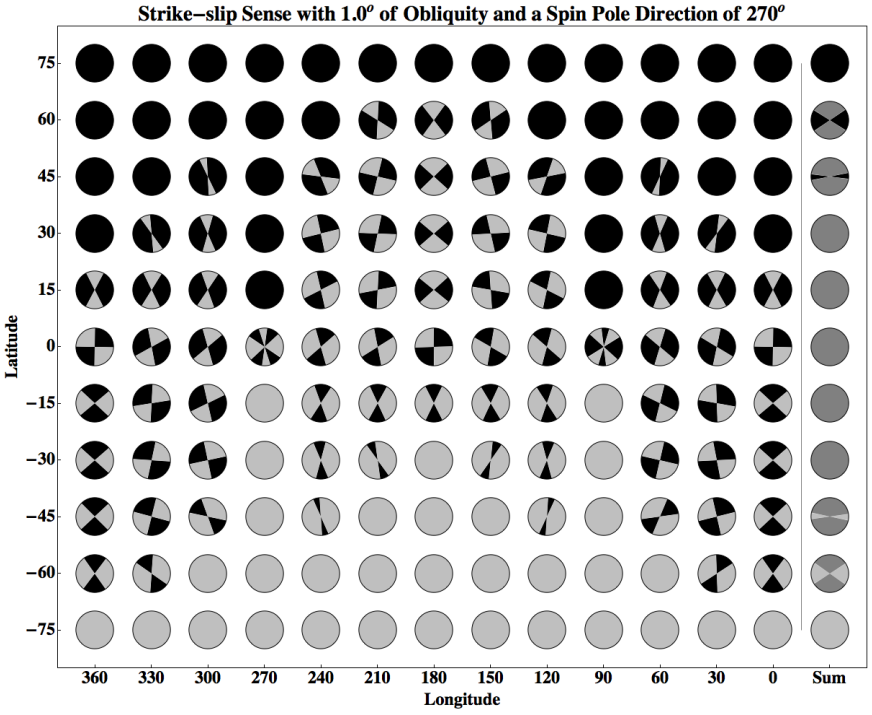
Strike−slip Sense with 1.0° of Obliquity and a Spin Pole Direction of 270°
Latitude
75
60
45
30
15
0
−15
−30
−45
−60
−75
360
330
300
270
240
210
180
150
120
90
60
30
0
Sum
Longitude

e.

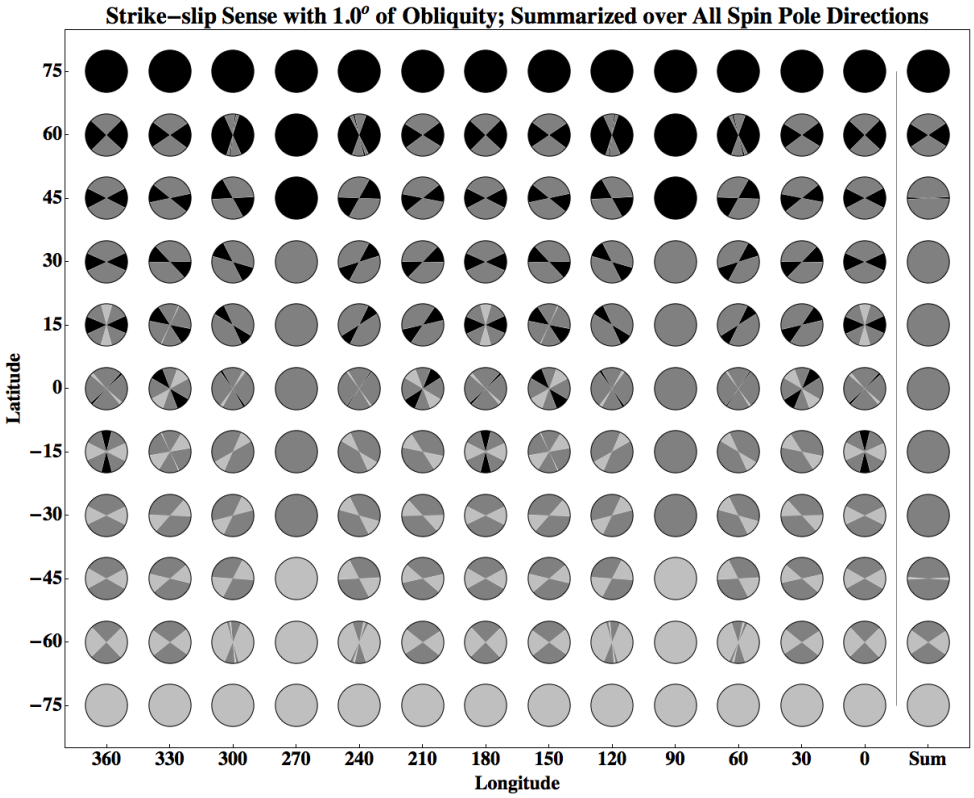

5.3.2 Direct comparison to observed faults

We conducted a direct comparison between our predictions and the 192 observed strike-slip faults from Sarid et al. (2002). To do this, we used the exact locations of the faults rather than the global prediction grid. Sarid et al. (2002) showed maps of strike-slip faults they identified; the corresponding database of faults contains the azimuth, slip direction, and latitude and longitude for the starting and ending points of each fault (Appendix 5.A1). We checked the database against Galileo images that have been tied into Europa's latitude/longitude grid (image cubes were obtained from the Planetary Image Research Lab at University of Arizona) and found that the latitude information for many faults in the leading hemisphere appeared incorrect. Further investigation revealed that latitude information in the Galileo regional mosaics (e.g. E17REGMAP01) differs from that of the global mosaics in which Galileo images are inset into global Voyager imagery. In regions that were imaged by Voyager and included in the Galileo regional mapping data set, the latitudes were again inconsistent although resolution may also be an issue in those cases. Latitudes vary by as much as 1° in the southern leading hemisphere, which also causes some variability in the corresponding longitudes of affected features. In regions where both right and left lateral faults can form, the azimuth cutoff between the two may change slightly depending on the latitude and longitude. Because of the uncertainties in location and ambiguity as to where along each fault to make the comparison, we made predictions at all of the points listed as starting points and then at all of the ending points (Appendix 5.A1). We conducted tests to determine the extent to which the uncertainty in location influenced our results. Using models that do not include

longitude migration, we found that the predictions differ for 0 to 2 faults depending on the exact location at which the prediction is made. In cases where the results were different, we report the higher number of incorrectly predicted faults. With longitude migration, the accuracy of the longitude measurement is less important because the prediction will not be made at that longitude.

Using the current fault locations (Appendix 5.A1), we tested tidal models with eccentricity only, eccentricity and obliquity, eccentricity and physical libration, and all three effects combined. The values of obliquity we tested were guided by which global predictions had asymmetric patterns consistent with observations. In addition, we tested physical libration amplitudes of 0.5, 1.0, and 1.5° using libration phases of 0, 90, 180, and 270°. For our final test, we added longitude migration to the eccentricity-only and obliquity models by making predictions at every 10° of longitude. In cases with longitude migration, we considered a fault to be accurately predicted if its slip direction was matched at any tested longitude. Results from our comparisons with observed faults are summarized in Table 5.1 in which we list each of the models tested and the number of features that could not be produced with each model.

Table 5.1: Tidal models tested against strike-slip observations and corresponding results.

Obliquity	Spin pole direction	Longitude migration	Physical libration amplitude	Physical libration phase	Number of incorrectly predicted faults
0°		No	0°		71
0°		No	0.5°	Any	71
0°		No	1.0°	Any	71
0°		No	1.5°	90/180/270°	71
1°	270°	No	0°		60
1.1°	270°	No	0°		63
1.2°	270°	No	0°		63
1°	Combined	No	0°		30
1.1°	Combined	No	0°		28
1.2°	Combined	No	0°		27
1.2°	Combined	No	0.5°	0°	18
1.2°	Combined	No	1.0°	0°	6
1.2°	Combined	No	1.5°	90°	18
0°		Yes	0°		30
1°	90/270°	Yes	0°		4
1.1°	90/270°	Yes	0°		1
1.2°	90/270°	Yes	0°		0

Using the current locations of the faults, the eccentricity-only model fails to predict the slip directions of 71 faults. Adding physical libration (without obliquity) does not improve the results for any combination of libration amplitude or phase we tested. The global predictions show that an obliquity less than 1° produces strike-slip patterns that are not asymmetric enough to match the observed strike-slip patterns so we explored values between 1° and 1.2°. The best of these tidal models includes an obliquity of 1.0°

with SPD 270°, and still cannot fit 60 faults. With all SPDs combined, the lowest number of mismatched faults falls to 27 with 1.2° of obliquity.

In our last attempt to predict faults at their current locations, we use a tidal model that combines 1.2° of obliquity, the combined predictions at spin pole directions every 30°, and physical libration. Using a libration amplitude of 1° and libration phase of 0° provides the best match to observations, accurately predicting all but six faults. Although this result requires no longitude migration, the model does introduce additional degrees of freedom from the libration amplitude and phase and requires the assumption of fast spin pole precession to justify combining predictions made with different spin pole directions.

Allowing longitude migration improves results for the eccentricity-only and obliquity cases. We did not test any tidal models that included physical libration or combined spin pole directions along with longitude migration. The predictions using the eccentricity-only model match all but 30 faults. An obliquity of 1° and a spin pole direction of 90° (equivalent to 270°) combined with longitude migration can accurately predict the slip directions of all but four faults. Increasing the obliquity to 1.1° fits all but one fault; 1.2° results in accurate predictions for the slip directions of all 192 faults.

5.4 Discussion

We used a modified version of the tidal walking model to predict slip direction, based on the direction of shear stress at the time the normal stress becomes compressive. Hoppa et al. (1999c, 2000) used the difference in shear stress at opening versus closing. If the shear stress increased while the crack was open (i.e. in tension), they predicted left lateral displacement; a decrease resulted in right lateral displacement. In cases where the magnitude of the shear stress was the same at opening and closing, they predicted no slip on the fault. The only substantial differences between these two methods are in the predictions at the equator, which Hoppa et al. (1999c, 2000) did not show in their global prediction plots. We attempted to fit observed strike-slip faults using both methods in test cases with and without obliquity, libration, and longitude migration; the results differed for 1-2 faults in several cases. However, we also tested those cases that provided the best fit to observed faults and found no difference in the number of faults fit with each method.

Our global predictions (Figs. 5.4 & 5.5) show systematic changes in the predicted slip directions of faults from exclusively left lateral in the far north to only right lateral in the far south for most longitudes. However, the equatorial predictions at longitudes 90° and 270° have a unique pattern with additional disconnected regions in which right or left lateral faults form. Upon further inspection of the stress in this region, we found that the magnitude of the normal stress is much less than the shear stress, which could permit shear displacement along the fault even when it is in compression contrary to the "rules" of the tidal walking model. This would result in a prediction of no net slip rather than right or left lateral. We should note that Sarid et al. (2002) did not identify any faults in these regions due to low-resolution imagery (at 270°) and the prevalence of chaotic terrain (at 90°) so the ambiguity in model prediction does not affect our results and can not be assessed by comparison with observation. This case highlights the major shortcoming of the tidal walking model: its lack of a detailed mechanical treatment of slip along the faults.

For this work, applying the tidal walking model was necessary because we are reassessing previous conclusions made using that model in light of the new evidence for non-negligible obliquity. In addition, tidal walking is the only model that has been shown to reproduce the global pattern of strike-slip observations. However, a strike-slip model for Enceladus' tiger stripes has been proposed (Smith-Konter & Pappalardo, 2008), which employs a Coulomb failure criterion to determine if and when faults will slip and a linear elastic relationship between stress and strain to quantify the net slip on faults. Since no evidence of strike-slip displacement has been observed along the tiger stripes, the model has not yet been validated. A useful direction for additional work on Europa's strike-slip faults would be to incorporate a more detailed mechanical treatment of slip along faults, perhaps akin to that of Smith-Konter and Pappalardo (2008), into the tidal walking model. Such a model could be vetted in a similar manner to our current assessment, by testing its ability to generate the observed global pattern of strike-slip faults on Europa. In addition, the magnitude of displacements may also be useful for testing models that include a more mechanical treatment.

Kattenhorn (2004) identified some faults with strike-slip displacement that also display sharp kinks or veers, similar to terrestrial tailcracks in which the veers or kinks form in response to slip on the original fault. By comparing the geometries of the tailcracks to predictions based on linear elastic fracture mechanics, Kattenhorn (2004) concluded that the "ridge-like" strike-slip faults displaying tailcracks formed without a significant dilational component. In other words, the displacements occurred when the fault was in compression, which is contrary to the tidal walking model. "Band-like" strike-slip faults with tailcracks were found to be consistent with tidal walking. As previously discussed, expanding the tidal walking model to allow for slip during compression would be more realistic and could perhaps explain the formation of the "ridge"-like tailcrack faults. In addition, it is certainly plausible that some strike-slip faults on Europa are formed through a different process than tidal walking or even due to regional rather than tidal stresses. Inadvertently including some of these features in our analysis could impede our ability to match fault statistics with our various tidal models. However, given the large number of observed faults (192) compared to the seven "ridge-like" faults with tailcracks identified by Kattenhorn (2004), it is unlikely to have significantly impacted our results.

We find that an obliquity of 1.2°, with longitude migration, can match all the observations in the Sarid et al. (2002) database. However, the obliquity is predicted to change on timescales that are short relative to Europa's surface age (Bills et al., 2009) so the tectonic record likely includes features formed with different obliquity values. Therefore, we consider 1.2° to be the maximum obliquity indicated by strike-slip faults; the average value could be much lower and still account for strike-slip observations. These results are consistent with theoretical expectations (Bills et al., 2009) and results from cycloid modeling (Hurford et al., 2009a; Rhoden et al., 2010). Although we cannot rule out the slow polar wander hypothesis previously invoked to explain observations of strike-slip faults on Europa (Sarid et al., 2002), we find it unnecessary in light of the mounting tectonic evidence in favor of obliquity (Bills et al., 2009; Hurford et al., 2009a; Rhoden et al., 2010).

The implications for physical libration are not obvious. The model that includes both obliquity and physical libration is successful at fitting all but six faults at their

current locations, but adding longitude migration to the obliquity model accounts for all strike-slip observations with fewer free parameters. This implies that, at least statistically, longitude migration is the more robust model. Studies of cycloids, however, support both physical libration and longitude migration due to non-synchronous rotation (e.g. Rhoden et al., 2010). Perhaps, when additional imagery allows for a more extensive survey of strike-slip faults, we can distinguish between these two effects and determine if there is a signal of physical libration in strike-slip patterns. Alternatively, if Europa's physical libration is a large as cycloid modeling indicates (~1°), it may be measurable using Earth-based radar techniques (e.g. Margot et al., 2007)

Our conclusion that the "offsets" in Europa's strike-slip fault patterns are not the result of slow reorientation but rather are the result of obliquity, does not rule out the possibility of other polar wander events throughout Europa's history. Semi-circular depressions and trough systems observed in both hemispheres of Europa are thought to be among the remnants of an ~80° polar wander event (Schenk et al., 2008). These features presumably formed in response to the large stresses incurred by polar wander. These stresses should also have generated extensive strike-slip faulting, but such features have not yet been identified (Schenk et al., 2008) perhaps because they were overprinted by subsequent tectonic activity. Polar wander stress was also proposed to influence the formation of global-scale lineaments, but comparison between observed lineament azimuths and theoretical predictions were not definitive (Leith and McKinnon, 1996). In short, our results are not in conflict with the formation of semi-circular depressions via polar wander.

One of the distinguishing characteristics of the strike-slip observations is that they exhibit a different pattern in one hemisphere than the other: the region of mixed right and left lateral faults extends north of the equator in the trailing hemisphere and south of the equator in the leading hemisphere. That is what led to the polar wander interpretation and our interest in applying obliquity to the predictions. When we sum the predictions over all longitudes, this piece of information is obscured. It appears, from looking at the sum columns in Figure 5.5a-e that, with enough obliquity, almost any pattern of strike-slip motion could be fit once we allow longitude migration. However, we find that only limited longitude shift is required to match the vast majority of the slip directions of faults when obliquity is included in the tidal model. Specifically, using 1.2° of obliquity and a phase of 90°, we accurately predict over 90% of the fault motions with no more than 90° of longitude migration (assuming no NSR stress accumulation). Obliquity produces the hemispheric pattern required to fit most of the observations with limited longitude shift. Summing over all longitudes allows us to also account for the few remaining outliers, which may be older slip events in the record. Lineament sequences have been established in many regions of Europa (e.g. Sarid et al., 2004), which could perhaps be used to test the hypothesis that faults requiring more longitude migration are in fact older.

The existence of the observed hemispheric pattern may also have implications for the amount and rate of NSR reflected in the tectonic record even though we do not incorporate stress from the rotation in our tidal models. The lack of mixed right and left-lateral faults in the south trailing hemisphere, for example, suggests that the most recent tectonic record does not include longitudes at which mixed faults form. However, 180° away from the current longitudes, the obliquity model would produce a mixture of faults

south of the equator. This suggests that the majority of fault motions in the record occurred within the last 180° of NSR (we find <90° is sufficient for most faults), and that the rate of strike-slip displacement was fast compared to the NSR rate. Conversely, if NSR was fast with respect to the formation of these faults, the pattern should be roughly the same at all longitudes: a wider band of mixed faults extending equally far both north and south of the equator.

The implication that only a fraction of a rotation has occurred in recent Europan history is quite different from the results of in-depth analyses of lineaments and cycloids (see also Kattenhorn and Hurford, 2009). Geissler et al. (1998) first suggested that the azimuths of lineaments should change systematically (increasing clockwise in the north and counter-clockwise in the south) as the surface rotates non-synchronously through the stress field. Their initial finding, based on cross-cutting relationships mapped in low-resolution imagery, found evidence of the expected pattern with time and determined that much less than one rotation was reflected in the azimuths. However, subsequent analysis (Sarid et al., 2005), which relied on higher resolution imagery and included many more lineaments and cross-cutting relationships, found that there was no pattern; the lineament azimuths in the region were indistinguishable from a random set. The lineament azimuths may in fact be changing systematically with time, but the lack of NSR signal suggests that lineament formation is slow with respect to the rate of NSR such that too few lineaments form per cycle to display a continuous pattern. If the prescribed pattern were applied, a minimum of one but generally several non-synchronous cycles would be required to account for the lineament azimuths in the regional mapping areas (Figueredo & Greeley, 2000; Sarid et al., 2004; Sarid et al., 2005; Sarid et al., 2006) and the "bright plains" equatorial region (Kattenhorn, 2002). Modeling of cycloids (Hoppa et al., 2001; Hurford et al., 2007a; Rhoden et al., 2010) and the average orientations of cycloids (Groenleer & Kattenhorn, 2008) also suggests greater than one and up to several non-synchronous rotations of the surface. However, cycloids are less numerous than lineaments and often do not have as many useful cross-cutting relationships that can be used to create long time sequences.

Despite the apparent contradiction, the results from studies of strike-slip faults and lineament azimuths may be consistent. The lineaments in a given region may in fact form slowly with respect to NSR such that many rotations of the surface are reflected in their azimuths. Then, subsequent strike-slip motion could occur along the lineaments – a process that could be fast with respect to NSR. The result of these two processes could be a set of lineaments with little signal of NSR but exhibiting strike-slip motion with a very strong signal that reflects activity mainly during the past 90°-180° of rotation. For this idea to be viable, older strike-slip motion would need to be largely erased such that the strike-slip record is constantly being reset. Rapid resurfacing would eliminate the older slip record but would also eliminate the lineaments, which do appear to be preserved over several rotations. Alternatively, strike-slip motion along a fault in one direction could perhaps be erased by subsequent motion in the opposite direction as stresses change due to longitude migration. Developing a mechanical model to explore this hypothesis would be an interesting avenue of future work.

A more complex tidal model will also affect the expected lineament azimuth patterns. Geissler et al. (1998) made their predictions of systematic azimuth change based on non-synchronous rotation through an eccentricity-generated tidal stress field. Perhaps

the azimuths would not follow such a simple pattern if obliquity and/or physical libration were included in the model of tidal stress. In that case, the lineament azimuths could potentially reflect much less rotation than otherwise indicated and be more consistent with the strike-slip record.

The implications for NSR depend mostly on our ability to sample both north and south of the equator. Therefore, sampling bias should not be an issue for the trailing hemisphere where we have the same amount and quality of imagery from about 75N to 75S. The observation that the mixed region is north of the expected location based on the eccentricity model, and the far south has little to no mixing should not be the result of observation bias. In the leading hemisphere, there is extensive chaotic terrain just south of the equator, which did result in gaps in the observations. In Figure 5.2, the empty circles at longitude 90° and latitudes 0° and -15° reflect areas that could not be mapped due to chaos (whereas the additional empty circles represent regions that were not mapped by Sarid et al. (2002) due to a lack of high-resolution imagery). Regardless, even further south where chaos is not an issue, both right and left lateral faults were observed that cannot be explained without obliquity even with longitude migration.

5.5 Conclusions

By incorporating an obliquity of 1.2°, we find that a tidal walking formation model combined with subsequent non-synchronous rotation can correctly predict the sense of slip of all the observed faults. Slow polar wander, invoked by Sarid et al. (2002) to explain the latitudinal mismatch between strike-slip predictions and observations, is no longer necessary once the effects of obliquity are included. Obliquity has also been shown to alleviate mismatches between cycloid formation models and observations, which polar wander would not directly resolve. Slow non-synchronous rotation is indicated within the strike-slip record, but the majority of fault motions require limited rotation. This suggests that the majority of the observed strike-slip occurred in only a fraction of a non-synchronous rotation of the surface, and thus, occurs quickly with respect to NSR. Measuring Europa's current obliquity, spin pole direction, and physical libration would be useful goals of any future mission.

5.A1 Table of fault observations

Table 5.A1: Observed strike-slip faults catalogued by Sarid et al. (2002).

Region	Starting latitude	Starting longitude	Ending latitude	Ending longitude	Azimuth (° CW off N)	Slip direction
Far northern trailing hemisphere (orbit e19)	73.184	226.85	75	221.58	112.42	L
	70.98	221.5	69.07	222.35	100.23	L
	69.24	224.45	68.45	222.35	110.6	L
	68.51	226.01	68.75	225.33	70.87	L
	68.11	220.57	67.61	218.81	105.86	L
	67.55	228.5	67.08	227.24	110.46	L
	67.53	228.16	67.96	227.29	63.71	L
	67.45	213.94	63.02	225.68	69.62	L
	67.22	212.54	66.89	213.49	71	L
	66.36	230.36	67.42	228.16	64.32	L
	64.43	225.6	64.47	224.29	87.93	L
	63.87	227.04	64.04	225.55	83.59	L
	62.62	216.65	62.4	216.46	139.84	L
	62.52	216.78	62.31	216.64	146.67	L
	61.49	222.03	61.47	221.45	92.22	L
	61.41	225.15	61.76	224.2	69.75	L
	60.51	219.6	61.09	217.19	76.52	L
	60.42	228.17	60.15	227.85	128.87	L
	59.61	227.37	59.55	227.26	122.01	R
Northern trailing hemisphere (orbit e15-01)	58.55	221.04	58.68	220.53	76.05	L
	58.29	221.29	58.67	220.51	64.39	R
	56.59	220.45	55.28	219.81	153.95	R
	55.62	224.47	57.10	227.68	28.16	L
	50.57	228.41	51.67	228.10	15.78	L
	47.93	220.91	47.92	220.13	91.326	L
	47.70	220.89	47.73	220.05	88.047	L
	47.62	223.99	47.68	223.61	80.886	L
	47.44	224.94	47.47	224.74	79.709	L
	47.06	215.88	47.12	215.52	80.703	L
	44.79	213.82	44.71	213.67	116.774	R
	43.51	229.43	43.43	229.21	111.351	R
	40.66	227.18	40.60	227.02	110.761	R
	39.92	215.94	40.03	215.84	41.367	R
	39.50	227.08	39.60	226.96	52.44	R
	39.49	228.64	38.54	228.48	70.85	R
	38.94	230.57	39.04	230.31	67.918	R
	37.81	220.28	37.88	219.93	78.565	R
	34.13	215.96	34.06	215.78	110.134	R
	33.92	215.65	33.66	215.29	125.048	R
	31.67	229.09	32.67	228.33	37.228	R
	30.89	230.76	32.77	228.18	53.968	L
	29.78	230.32	29.94	230.12	52.509	R
	29.58	224.74	29.63	224.55	75.652	R
	29.30	217.91	29.46	216.88	81.143	L
	27.91	219.17	27.30	218.29	124.507	L
	25.61	224.41	24.93	224.30	170.116	L
	25.19	221.83	25.41	221.64	40.79	L
	24.07	224.84	23.86	224.63	165.552	L

	23.75	224.66	23.78	224.54	77.615	R
	23.38	220.70	24.31	219.65	47.78	L
	22.90	219.31	23.10	218.60	75.99	R
	22.34	223.45	22.22	223.63	55.448	R
	21.35	223.68	20.55	223.34	156.845	L
	21.11	224.85	21.19	223.91	85.267	L
	21.10	228.56	21.80	228.10	32.59	L
	21.09	225.75	21.20	225.29	75.672	L
	21.02	223.96	20.12	223.72	165.453	L
	21.00	226.57	21.06	226.30	76.566	L
	20.85	227.60	20.99	226.84	63.66	L
	20.55	227.71	20.68	227.46	62.897	L
	20.30	228.09	20.45	227.89	53.655	L
	20.15	228.27	20.04	228.40	49.592	L
Southern trailing hemisphere (orbit e17-01)	16.65	224.16	16.87	224.7	63.2	L
	15.4	225.6	16.1	224.6	55.8	R
	13.73	219.9	16	219	23.2	R
	11.9	221	12.5	219.8	63.17	R
	7.96	219.9	7.8	218	94.5	R
	-3.02	221.3	-4.36	219.9	132.27	L
	-3.7	227.5	-6.7	227.1	171.1	R
	-4.76	221	-4.1	220.5	37.5	R
	-4.89	221	-6.1	219.3	125.63	L
	-7.3	228.4	-8.2	229.8	57.5	R
	-7.65	226.8	-8.2	226.3	137.5	L
	-8.1	226	-8.9	225.3	138.13	R
	-8.3	224.3	-7.5	221.2	75	R
	-9.2	214.2	-9.5	213.8	128.48	R
	-9.2	227.1	-10.9	227.4	9.8	R
	-9.2	216.5	-9.99	215.2	123.66	R
	-9.4	224.8	-9.6	224.4	120.5	L
	-9.7	213.7	-9.9	213.3	119.12	R
	-10.15	231.7	-10.7	230.86	123.5	L
	-10.6	213.3	-10.4	212.5	75.98	R
	-10.7	227.2	-10.85	227.1	148.4	R
	-11.1	221.1	-11.5	220.7	140.95	L
	-11.2	212.8	-11.6	212.1	122.54	R
	-11.3	213.6	-12.3	212.9	143.63	R
	-11.4	225	-12.1	224.1	130.01	R
	-11.6	221.9	-13.6	221.2	158.9	R
	-11.8	220.7	-13.9	220.8	3.4	R
	-12	219.5	-13.1	219.02	156.8	R
	-12.1	214.6	-13.3	213	136.7	R
	-12.2	223.9	-10.8	222.9	36.63	R
	-12.2	226.75	-13.5	227.2	19.1	R
	-12.86	224.8	-12.3	224.3	37.93	R
	-13	212.8	-13.6	213	19.11	R
	-13.5	232.4	-13.9	232.4	0.9	R
	-14	213.9	-13.8	213.1	73.7	R
	-14.1	223.9	-14.7	223.6	151.87	R
	-14.75	232.2	-15.5	231.5	135.9	R
	-14.9	221.2	-15.2	221	140.1	R
	-15.4	224.7	-14.3	223.9	38.7	R

	-15.5	222.02	-15.97	222.8	60	R
	-16	221.4	-16.7	220.4	125.77	R
	-16	220.7	-16.5	220	127.37	R
	-16.2	226.7	-14.6	225.9	25.2	R
	-16.3	343.7	-17.1	228.4	112.5	R
	-16.6	230.4	-17.1	229.7	125.9	R
	-16.8	221.3	-17.5	221.2	176.08	R
	-16.97	219.02	-16.5	218.6	46.6	R
	-17	223.7	-17.3	223.3	118.52	R
	-17.3	224	-17.7	223.6	140.9	R
	-17.6	222.6	-17.5	221.7	81.86	R
	-17.8	219.2	-18.1	217.9	101.85	R
	-18.4	220.9	-17.65	220.3	40.6	R
	-18.7	226.3	-18.6	225.9	48.8	R
	-18.8	226.2	-19.25	225.8	139.3	R
	-19.1	222.6	-19.6	222	130.66	R
	-19.3	223.5	-19	222.8	67.52	R
	-20	229.3	-19.8	228.1	78	R
	-20.1	223.8	-21.4	224.7	34.3	R
	-21.4	226.7	-22	226.3	143	L
	-24.9	226.9	-24	225.2	64.3	R
	-26.7	224.8	-27.1	224.6	159.3	R
	-28	226.6	-28.4	225.9	122	R
	-30.4	225.1	-30	223.9	74.1	R
	-30.7	223.1	-30.25	222.7	35.1	R
	-30.7	224.6	-30.2	223.9	55.9	R
	-31.4	223.8	-32.7	223.35	159	R
	-32.8	217.8	-31.9	217	42.48	R
	-42.4	177.9	-41.5	177.9	4.6	R
	-43.2	225.7	-42.3	223.35	69.7	R
	-44.7	178.9	-45.3	177.4	111.17	R
	-45.1	176.4	-45.9	174.2	109.94	R
	-48.7	211.6	-49.4	210.7	124.98	R
	-50	183.2	-50.6	183.3	6.71	R
	-50.3	180.2	-50.6	181.4	76.98	R
	-50.5	177.1	-50.7	176	101.51	R
	-53.8	185.7	-54.4	184.3	113.42	R
	-54.4	190.2	-53.3	189.6	26.95	R
	-57.6	181.5	-56.8	181.8	159.14	R
	-60.9	200.9	-59.7	199.8	41.63	R
	-61.5	200.5	-61.8	199.3	100.24	R
	-63.2	208.9	-63.4	207.8	99.22	R
	-64.1	211.5	-64	208.7	88.87	R
	-67	193.8	-64.6	193.9	176.9	R
	-68.1	209.7	-66.97	208.1	55.12	R
Northern leading hemisphere (orbit e15-02)	56.85	79.8	58.5	75.3	165.43	L
	40.87	74.95	41.26	73.67	73	L
	36.51	86.77	36.32	86.2	107.67	R
	27.25	75.68	27.66	75.4	32.5	L
	26.26	79.73	26.49	79.53	40.15	R
	25.98	77.5	26.7	77.05	30.6	L
	23.1	76.85	22.2	75.6	125.75	L
	21.65	79.25	21.88	78.95	52.1	L
	19.1	83.7	18.6	82.5	112.8	R

	19.1	82.96	19.37	82.28	66.1	R
	14.6	83.8	14.2	83.4	139.3	L
	14.24	84.3	13.9	83.6	118.6	L
	13.7	84.95	12.3	84.3	155.2	L
Southern leading hemisphere (orbits e17-02 & 03)	-33.41	73.42	-33.33	72.96	80.343	R
	-33.54	74.54	-33.66	74.02	103.03	R
	-33.71	75.58	-33.47	74.95	68.953	R
	-36.14	85.55	-36.23	85.48	140.456	R
	-36.70	85.45	-37.01	85.02	125.976	L
	-39.63	86.32	-39.70	86.19	118.726	R
	-39.79	84.51	-39.76	84.40	72.802	L
	-39.96	81.23	-40.05	81.20	160.08	L
	-40.23	81.55	-40.35	81.51	158.841	L
	-40.25	73.10	-41.23	72.51	148.83	L
	-40.46	86.42	-40.66	86.12	122.713	R
	-40.84	88.53	-41.16	86.83	100.753	R
	-41.02	85.44	-41.47	84.20	109.864	R
	-41.74	84.44	-42.13	82.92	104.484	R
	-41.94	84.07	-42.27	83.22	111.08	R
	-42.20	81.31	-42.40	80.81	111.835	R
	-42.42	82.34	-42.89	81.26	113.66	R
	-43.96	75.32	-43.96	75.33	91.552	L
	-44.24	84.69	-44.16	83.76	85.412	L
	-44.76	85.83	-44.96	85.04	103.569	R
	-45.07	83.07	-45.16	82.65	102.89	R
	-46.70	85.71	-46.80	85.67	160.265	L
	-47.06	80.88	-48.88	77.88	121.262	R
	-47.84	74.26	-47.74	72.61	86.646	R
	-48.65	73.71	-49.63	72.24	123.443	L
	-49.01	77.79	-54.86	74.76	152.485	R
	-49.42	93.72	-49.59	93.27	110.213	R
	-55.07	88.48	-54.92	87.94	73.695	R
	-57.85	97.92	-58.35	97.99	6.25	L
	-58.23	92.52	-59.27	91.00	124.607	R
	-58.36	100.84	-58.43	99.63	93.428	L
	-59.34	90.99	-61.52	83.83	106.844	R
	-71.46	97.25	-73.39	92.10	110.403	R

5.A2 Revised eccentricity predictions

In Figure 5.4, we show revised predictions for slip direction without obliquity on a finer grid than was presented in Hoppa et al. (1999c, 2000) and using our criteria for determining slip direction. For more direct comparison, we show the predictions at the same grid points and using the original criteria in Figure 5.A1. Note that here we follow the convention of Hoppa et al. (1999c, 2000), using white rather than light grey to represent right lateral faults. The difference between our predictions and the Hoppa predictions is most obvious in the pinwheel character seen at 10°S and 10°N, which was apparently an artifact of applying vector decomposition to the total stress tensor when determining the normal and shear components relative to a fault. In addition, comparison with Figure 5.4 shows that there is no significant difference between the two methods for predicting slip direction.

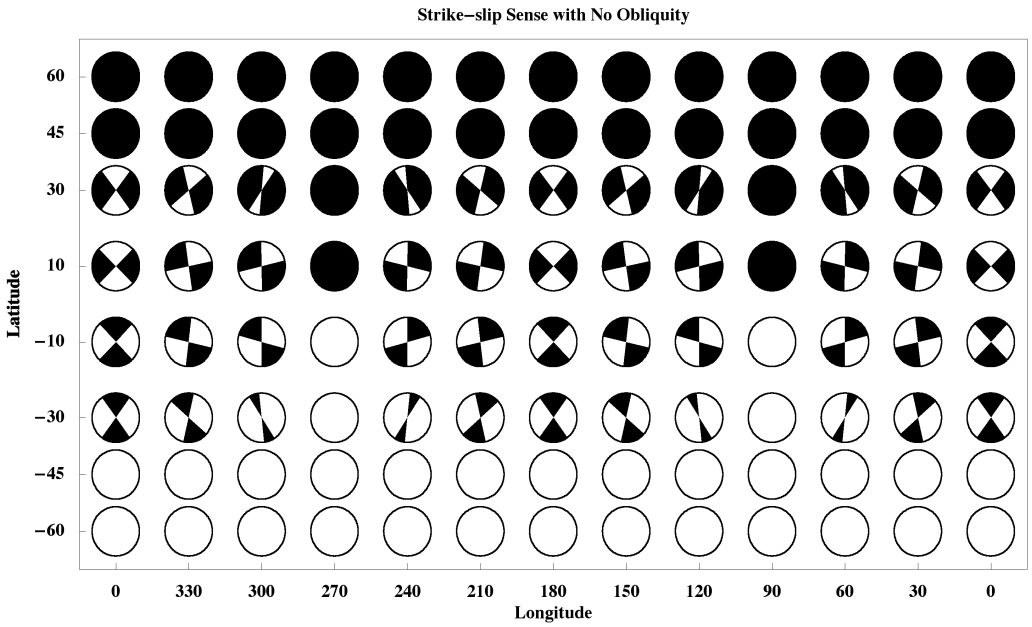

Figure 5.A1: Predictions with zero obliquity using the same latitude/longitude grid, prediction method, and color scheme as Hoppa et al. (1999c, 2000). Here, black is left lateral, but white is right lateral. Our revised predictions do not display the pinwheel character seen in the original Hoppa predictions. Comparison with Figure 5.3 confirms that the different prediction methods have little influence on the predictions.

5.A3 Global predictions using an obliquity of 0.5°

Figure 5.A2: a-e. Predictions with 0.5° obliquity at spin pole directions of 0° (a), 90° (b), 180° (c), 270° (d), and with SPDs at every 30° combined (e). In each plot, the last column shows the predictions at all longitudes combined. Black represents fault azimuths that will exhibit left lateral displacement, and light grey represents right lateral faults; dark grey indicates that either type of fault can form, and white shows cases where we do not predict any net slip.

a.

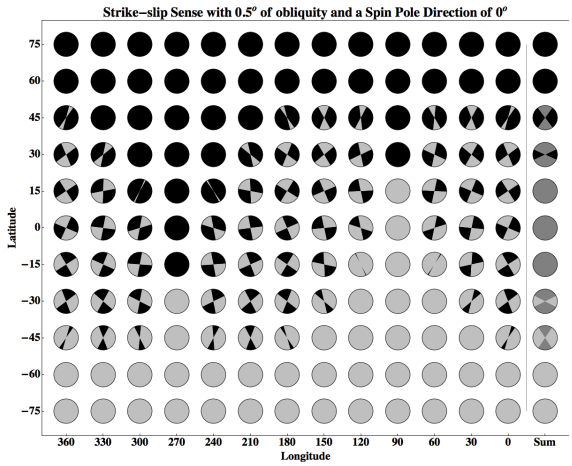

b.

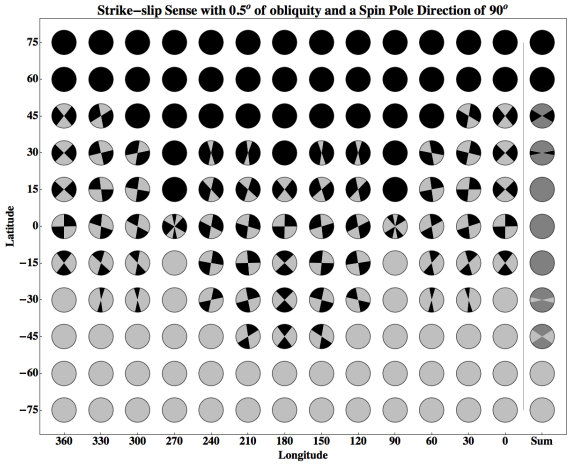

c.

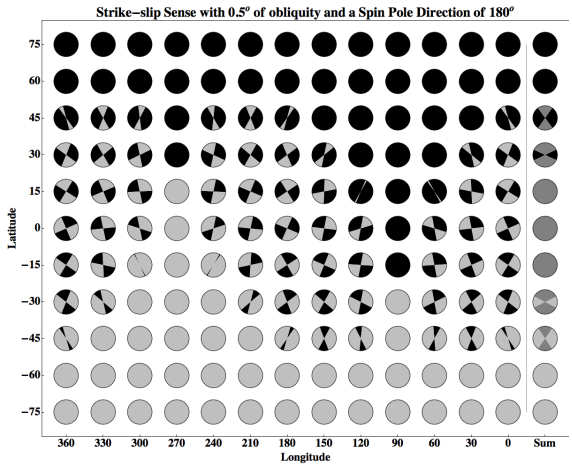
Strike−slip Sense with 0.5° of obliquity and a Spin Pole Direction of 180°
Latitude
75
60
45
30
15
0
−15
−30
−45
−60
−75
360 330 300 270 240 210 180 150 120 90 60 30 0 Sum
Longitude

d.

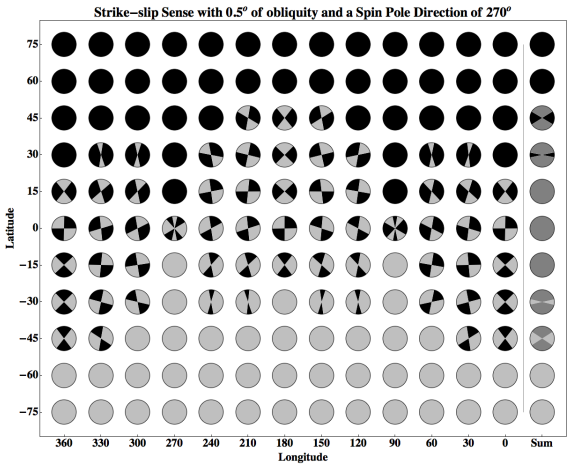
Strike−slip Sense with 0.5° of obliquity and a Spin Pole Direction of 270°
Latitude
75
60
45
30
15
0
−15
−30
−45
−60
−75
360 330 300 270 240 210 180 150 120 90 60 30 0 Sum
Longitude

e.

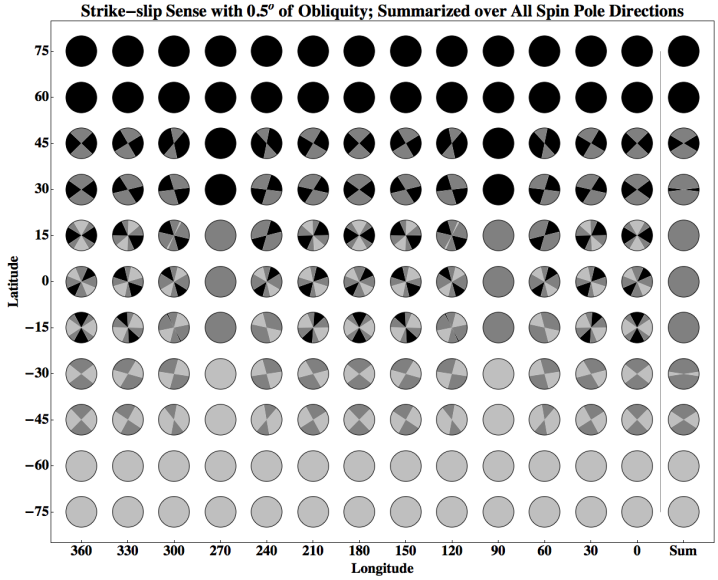
Strike−slip Sense with 0.5° of Obliquity; Summarized over All Spin Pole Directions
Latitude
75
60
45
30
15
0
−15
−30
−45
−60
−75
360 330 300 270 240 210 180 150 120 90 60 30 0 Sum
Longitude

Chapter 6: Understanding strike-slip formation on Europa

6.1 Introduction

Strike-slip offsets are common along Europan lineaments of varying length and type (Schenk and McKinnon, 1989; Tufts et al. 1999; Hoppa et al., 2000; Figueredo & Greeley, 2000; Sarid et al., 2002; Kattenhorn, 2002; Riley et al., 2006; Kattenhorn and Hurford, 2009a). A comprehensive survey of strike-slip faults in the Galileo regional mapping data set identified almost 200 strike-slip faults (Sarid et al., 2002; Table 5.A1). In Figure 5.1, we show the azimuths and locations of the left lateral (red) and right lateral (blue) faults that were identified. The survey revealed that, on a large-scale, the sense of motion along faults is not random. The distribution of faults is generally left lateral (LL) in the far north and right lateral (RL) in the far south, with a mixture of both fault types in between. The ratio of LL to RL faults in the mixed region decreases with latitude and trends differently between the leading and trailing hemispheres. Fault statistics from the survey (Sarid et al., 2002) are shown in more detail in Table 6.1.

As shown in Chapter 2, the tidal stress due to orbital eccentricity and obliquity can be decomposed into normal and shear components along a fault of given azimuth and location. Depending on the fault response model adopted, the changes in stress throughout an orbit can be analyzed to determine the likely net offset direction along the fault. We present a new mechanical model for the formation of these tidally-driven strike-slip faults (Sections 6.2 and 6.3). Our "shell tectonics" model combines tidal stress and an elastic rebound seismic model for slip and stress release on faults, in which accumulated shear stress on the fault is released when the fault slips. Our model successfully reproduces the observed global pattern of strike-slip faults on Europa. When obliquity is also incorporated, we can generate variations in the global pattern that are consistent with the observed differences in the leading and trailing hemisphere strike-slip fault populations. In contrast, we find that a model neglecting the release of stress due to slip is less effective at matching the global pattern of strike-slip (Section 6.4). We also discuss implications of these results on relative offset accumulation rates along faults and the depth to which strike-slip motion may occur (Section 6.5). In addition to advancing our understanding of tidally-driven tectonics on Europa, the shell tectonics model may also be relevant for Enceladus. Strike-slip motion and subsequent heat generation along the Tiger Stripe fractures has been linked to tides (Nimmo et al., 2007; Smith-Konter & Pappalardo, 2008), and tidally-driven opening and closing of the fractures has been proposed as a mechanism for controlling plume eruptions (Hurford et al., 2007b).

6.2 Models of tidally-controlled strike-slip

6.2.1 Previous models

As Europa moves through its eccentric orbit, a pre-existing fault will experience diurnally-varying normal and shear stresses that may drive tectonics. Hoppa et al. (1999c, 2000) introduced the tidal walking model, which assumes that faults slip freely while in tension, but that slip is prohibited during compression. Once failure initiates, slip on the fault accumulates until the magnitude of the tidal shear stress reaches a maximum. Then, because the ice shell is assumed to behave elastically over short (i.e. diurnal) timescales,

slip on the fault is reduced back toward zero as the shear stress decreases. Therefore, if the shear stress crosses zero during the tension phase, it is assumed that any accumulated slip up to that point has been recovered, and there is no net offset on the fault. When the normal stress becomes compressive, the fault is clamped; an offset on the fault reflects the amount of accumulated slip since the last time the shear stress crossed zero. In order to maintain this offset over subsequent orbits, elastic stresses in the shell must relax while the fault is clamped so that, when the normal stress again becomes tensile, the fault will not slip back to its initial configuration.

Hoppa et al. (1999c, 2000) used the tidal walking model to create global predictions of slip direction, which generally match the observed global pattern on Europa. Rhoden et al. (2011) made a correction to the predictions (see also, Section 5.A2), but this did not affect the resulting global pattern of only left lateral (LL) faults poleward of 35°N, only right lateral (RL) faults poleward of 35°S, and between these regions, either right or left lateral faults with the slip-direction depending on the longitude and the azimuth of the crack. Initially, observed differences in the strike-slip statistics of the leading and trailing hemispheres were attributed to non-synchronous rotation and true polar wander (Sarid et al., 2002). However, Rhoden et al. (2011) investigated the effects of obliquity on the predictions and concluded that an obliquity of ~1° could lead to offsets of the regions of mixed right and left lateral faults that are more consistent with the observations than polar wander (see also, Chapter 5).

Table 1: Strike-slip statistics from Sarid et al. (2002)

	Trailing hemisphere			Leading hemisphere		
	LL	RL	% LL	LL	RL	% LL
60N+	18	0	100	-	-	-
40-60N	8	6	57	2	0	100
20-40N	17	13	57	4	1	80
0-20N	1	4	20	3	2	60
20S*-0	7	47	13	-	-	-
40S-20S	0	8	0	3	5	38
60S-40S	0	11	0	8	16	33
60S-	0	7	0	0	1	0

* - The southernmost LL fault in the trailing hemisphere is located at 21.4°S; we included it in the 0-20S bin.

Its ability to reproduce the observed global pattern of strike-slip displacement is a strong indication that the tidal walking model captures a fundamental attribute of the fault slip process on Europa. However, the mechanics of the model are simplified. Neither stress release due to slip nor stress relaxation with time are explicitly included in the tidal walking model. In fact, predictions of slip direction are based solely on the sign of the shear stress when the normal stress becomes compressive (see Rhoden et al., 2011). Furthermore, failure is only allowed when the fault experiences tensile normal stress so the model is only applicable in the upper tens of meters of Europa's surface. Deeper within the shell, the compressive overburden stress would exceed the tidal stress and

clamp the fault throughout the entire orbit.

Preblich et al. (2007) investigated the ability of the tidal walking model to create offsets using a finite element code called Tekton (Melosh and Raefsky, 1981). They created 2D out-of-plane displacement simulations in which the boundaries were driven cyclically to mimic the tidal stresses. They adopted a power-law viscoelastic rheology and tested ice shell depths of both 1 km (their Cases 1, 5, and 6) and 10 km (Cases 2-4). In Case 1, it was assumed that the crack penetrated to the underlying water layer and water flowing into the crack offset the compressive overburden stress. In Case 2, overburden stress was again neglected, although they acknowledged that this would be unrealistic for a 10 km ice shell with a crack that penetrates only 2 km. In both of these cases, a net offset was produced in the manner described by the tidal walking model.

Tidal walking assumes that faults can only slip in net tension. In addition, Tekton does not have a friction law, so applying Coulomb failure was not an option. Rather, Preblich et al. (2007) tested cases in which some portion of the fault responded only to tidal stresses and the rest was locked throughout the entire orbit, presumably due to overburden. However, when realistic overburden stress was included, net offsets could not be produced because too much of the fault was locked. If the locking depth was made arbitrarily deep within the shell, net offsets could again be produced. This corresponds to an assumption of an additional component to the tidal stresses, such as uniform extensional stresses caused by cooling of the ice shell (e.g. Nimmo, 2004). In all cases for which the tidal walking model produced net offsets, over many 10s of orbits, the amount of additional net slip accrued during each subsequent orbit decreased. The results of Preblich et al. (2007) imply that faults in a viscoelastic shell would behave as the tidal walking model assumes. However, the model has limited success at producing net offsets under realistic stress conditions because faults were only allowed to slip in tension.

A model for strike-slip displacement due to tidal stress has also been proposed for Enceladus (Smith-Konter and Pappalardo, 2008) and should be equally applicable to Europa. In this model, which we will refer to as the SKP model, the fault can slip whenever the tidal shear stress exceeds the Coulomb failure criterion. Slip on the fault accumulates via a large event when the shear stress exceeds the Coulomb failure threshold and subsequent small, creeping events that continue as long as the tidal shear stress remains above the failure threshold. Summing the accumulated slip over one orbit yields a prediction of slip direction. Comparison between model predictions and the observed tiger stripe fractures on Enceladus is inconclusive (Smith-Konter and Pappalardo, 2008), and the model has not yet been tested against the global pattern of strike-slip faults on Europa.

A major difference between the tidal walking model and the SKP model is in the determination of slip direction throughout an orbit. In the tidal walking model, it is assumed that the shell, being elastic over short timescales, will act to restore the fault to its initial configuration. Hence, slip depends on the change in shear stress with time. In the SKP model, fault slip is determined by the value of the tidal shear stress regardless of whether it is increasing or decreasing. One way to visualize the difference is to think of the SKP model as describing the behavior along a boundary between two unconnected plates. Whereas, in the tidal waking model, the plates are connected in the far field by a spring. It is unclear *a priori*, which model best represents the behavior of faults on Europa and Enceladus.

To further investigate the mechanism of strike-slip fault formation on Europa, we take a dual approach. First, we develop a model based on the assumption of elastic rebound over short time scales, in the spirit of the tidal walking model, but that also includes a more quantitative and physical treatment of stress accumulation and slip on a fault. We also create a simplified version of the SKP model, adopting the rules for stress accumulation and slip outlined by Smith-Konter and Pappalardo (2008) and developed with their guidance (Smith-Konter, *personal comm*., 2010). We then test the underlying fault slip assumptions of each model by creating predictions of fault slip direction and comparing the predictions against the observations in the strike-slip survey by Sarid et al. (2002).

6.2.2 Shell tectonics

In the shell tectonics model, slip occurs when the accumulated shear stress on the fault exceeds the Coulomb failure threshold. When a fault is in tension, we set the failure criterion to zero (no cohesion). This results in continuous slip while the fault is in tension and large discrete events in compression. As with the SKP model for Enceladus (Smith-Konter and Pappalardo, 2008), allowing slip while the fault is under compression allows the shell tectonics model to operate deeper in the ice shell than the tidal walking model.

When the failure threshold is exceeded, the amount of resulting slip is assumed to be proportional to the accumulated shear stress on the fault at that time. We explicitly include the release of accumulated shear stress due to slip by resetting the shear stress on the fault to zero after every slip event. Hence, the tidal shear stress has to increase in magnitude for the fault to continue slipping in the same direction. If the shear stress instead decreases, the fault will begin to slip back toward its initial configuration. Thus, release of accumulated stress accounts for the elastic response of the shell. This is in contrast to the SKP model in which the fault continues to creep after the failure threshold is reached, and the direction of creep is always in the same direction as the initial slip event. To account for the long-term viscous behavior of Europa's ice shell, we also allow a small amount stress of relaxation when on the fault, which we find to be critical to producing net offsets. To make a prediction of slip direction, we determine the long-term trend of motion on the fault by calculating the difference in the net offset over many orbits. Additional details of these calculations are given in Section 6.3.2.

Use of accumulated shear stress rather than tidal shear stress when determining failure is a keystone of the shell tectonics model. Figure 6.1 is a schematic showing the tidal deformation of an unslipped region and a fault's response to that deformation at certain points in the orbit. The direction of the most compressive principal stress is also shown. Throughout the schematic, there is a regional left lateral (LL) tidal shear stress, which is increasing in magnitude at A and B but decreasing thereafter. We also assume that the regional tidal normal stress has just entered a period of compression. Previously, the fault was free to slip in response to the left lateral tidal deformation because it was in tension.

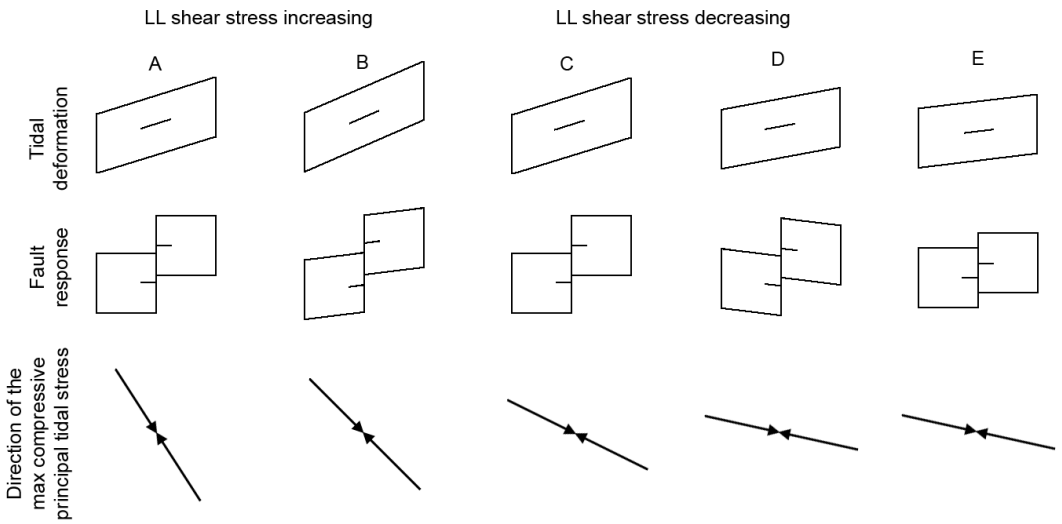

Figure 6.1: A schematic of tidal deformation and fault response with changing tidal shear stress. The direction of the most compressive principal stress is also shown. In A and B, the shear stress is increasing generating left lateral slip on the fault and reducing the accumulated shear stress on the fault. In C – E, the shear stress is decreasing. Because stress has already been relieved by slip, the fault begins to accumulate right lateral shear stress and ultimately slips in that direction, thereby reducing the net offset on the fault.

At A, the fault has a LL offset and zero accumulated shear stress. At B, the tidal deformation in the region has become increasingly left lateral. Based solely on the regional deformation, the fault would accumulate another LL offset, even larger than at A. However, if we only consider the accumulated stress on the fault, we get a much different answer. Because, the fault has already responded to the deformation at A, it accumulates a small amount of additional shear stress due to the incremental increase in deformation, but it is not enough to reach the failure threshold. At C, the tidal shear stress has decreased and is now identical to A. Thus, the accumulated shear stress on the fault returns to zero. At D, the regional deformation has decreased further. If the fault had never slipped, we would expect the deformation to induce left-lateral slip on the fault as long as the tidal stress exceeded the failure criterion. However, the fault has already slipped to accommodate the deformation at C, which is now more LL slip than would be generated at D. Hence, at D, the fault actually accumulates right lateral shear stress. At E, the deformation has decreased so much that the accumulated shear stress on the fault generates right lateral slip even though the regional tidal shear stress is still left lateral. The shell tectonics model would thus predict left lateral slip at A and right lateral slip at E. In the SKP model, the fault would undergo a large LL slip at A, continue creeping in a LL sense until C, and not slip again in this time period because the tidal shear stress is lower than the failure threshold. In the tidal walking model, no slip would have occurred during this entire time period because the fault was in compression.

6.3 Generating global predictions

6.3.1 Calculating tidal stress

Our formation model is based on the hypothesis that tidal deformation is the driver of strike-slip displacement on Europa. The daily changes in tidal stress thus control the ability of pre-existing faults to slip and the direction of net shear displacement along the faults. We neglect stress from non-synchronous rotation or overburden pressure (see also, section 6.5.3). We assume that Europa has long-since adopted its primary tidal shape, which is based on the average distance and angle between Europa and Jupiter. It is deviations away from that shape that generate stress. To calculate tidal stress, we use the thin shell equations given in Chapter 2, which incorporate the effects of obliquity. To determine the slip direction along a fault, we first specify the latitude and longitude of the fault, the fault azimuth, and the prescribed amount of obliquity and spin pole direction. Using these parameters, we calculate the stress throughout an orbit.

The equations for tidal stress presented in Chapter 2 assume an elastic rather than viscoelastic shell. Wahr et al. (2009) present equations for tidal stress in a viscoelastic shell. However, the Wahr et al. (2009) model does not include obliquity, an important parameter in our work. In addition, the predictions made with the tidal walking model relied on the formulation we present here (Hoppa et al., 1999c, 2000; Rhoden et al., 2011; Chapter 5), so it is useful for consistency to test shell tectonics against the same stresses. Smith-Konter and Pappalardo (2008) did use the Wahr et al. (2009) model, so it is important to consider how the two approaches differ in their calculations of tidal stress.

A major result of Wahr et al. (2009) is that stresses caused by non-synchronous rotation in a viscoelastic shell are phase-shifted from those in an elastic shell. For diurnal stresses, the amplitudes can differ by 0.1 – 3% between the elastic and viscoelastic cases, depending on the viscosity assumed for the ice shell. Because we neglect the effects of NSR stress, the differences between the diurnal stresses we calculate here and those used by Smith-Konter and Pappalardo (2008) should be small – indeed, no larger than 3%. Our main goal is to test whether observations are best explained with the assumption that – quite generally – slip on a fault is reduced when the shear stress decreases (shell tectonics) or that slip continues to increase even if the shear stress decreases (SKP). The exact amplitude of the tidal stress will not significantly affect this determination.

6.3.2 Applying shell tectonics

We use the shell tectonics model to fit the global strike-slip pattern on Europa by generating predictions on a global scale. We determine net offsets for faults with azimuths from 0 – 180° in 1° increments, at longitudes from 0 – 360° every 30°, and from latitude 75° to -75° in increments of 15°. We apply shell tectonics to tidal stress fields with and without 1° of obliquity and test two end-member values of the friction coefficient: 0.6 and 0.2. The higher friction value is appropriate for rock and may be applicable to very cold ice (Beeman et al., 1988); the lower value was used by Smith-Konter and Pappalardo (2008). We use it here for consistency.

To calculate the accumulated stress on the fault, we solve the following differential equation in which σ_{tidal} is the stress tensor and stress relaxes on an e-folding timescale of $1/\eta$:

$$(6.1)\quad d\sigma_{acc}/dt = (d\sigma_{tidal}/dt) - \eta\sigma_{acc}$$

The relaxation rate is a depth-averaged value that accounts for the decrease in ice

viscosity with depth. Our solution is restricted to values of η for which $\eta t_{orbit} << 1$. Without relaxation, we find that no net slip accumulates over time.

There is no release of accumulated normal stress in this model. Rather, we assume that the accumulated normal stress on the fault reflects the long-term behavior of daily-varying stresses that are slowly relaxed. We analytically solve Eq. 6.1 to determine the initial values of the accumulated normal stress components such that the transient part of the solution is minimized for each component. We also advance in the orbit to a time when the fault is in tension so the initial value of the accumulated shear stress can be set to zero. At each subsequent time step, we first add $\Delta\sigma_{tidal}$ and calculate the normal and shear components of the accumulated stress (using Eq. 2.4a,b). If the accumulated normal stress on the fault is positive (in tension), it will slip for any non-zero value of accumulated shear stress. In compression ($\sigma_{acc} < 0$), the accumulated shear stress must exceed the Coulomb failure threshold.

$$(6.2)\ \tau_{acc} = -f\sigma_{acc}$$

where f is the friction coefficient. If slip occurs, the cumulative slip is increased by the amount of accumulated stress on the fault and the accumulated shear stress is set to zero. Finally, we reduce the deviatoric component of any remaining accumulated stress, σ_{acc}, according to Eq. 6.1 to account for the long-term viscoelastic behavior of the shell. We compute the accumulated stress and cumulative slip at 8500 time steps per orbit and run each simulation over 1000 orbits to ensure that the solution has converged.

To predict the slip direction on the fault over time, we calculate the difference in slip at the same point in two successive orbits to determine the net offset. We then average the net offset over 1000 orbits to determine the long-term behavior on the fault. To reduce numerical noise, we repeat the simulation 20 times with a random number (between 0 and 1) added to the longitude, and average the net offset values over the 20 simulations. If the average net offset is positive, we predict left-lateral displacement on the fault; a negative average net offset yields a right-lateral prediction. If the net offset averages to zero, we predict no net slip on the fault.

6.3.3 Applying an SKP-type model

Because the observed global pattern is such a useful metric for testing tidal-tectonic models, we also generate predictions using a model based on Smith-Konter and Pappalardo (2008). In that model, there is a large slip event when the fault first reaches the failure criterion. Then, small slips occur as long as the tidal stress on the fault exceeds the Coulomb failure threshold. The amount of slip from the large events is proportional to the tidal shear stress on the fault at the time of failure. For the creeping events, Smith-Konter and Pappalardo (2008) assume a constant, time-averaged, strain rate to which the amount of accumulated slip is proportional. Unlike tidal walking or shell tectonics, the direction of slip in the SKP model is always the same as the tidal shear stress direction. The actual model presented in Smith-Konter and Pappalardo (2008) is more sophisticated than what we are using here. However, our interest is in testing the determination of when and how fault slip will occur in the SKP model versus the shell tectonics model. To accomplish this, we have adopted a set of rules for stress accumulation and fault slip that

capture these fundamental assumptions.

To compute a prediction of direction using our SKP-type model, we keep a running sum of LL (positive) and RL (negative) slip throughout an orbit. When the tidal stress on a fault first reaches the failure criterion for one slip direction, there is a large slip event in which all of the tidal stress on the fault is relieved. Hence, the amount of slip is proportional to the amount of shear stress. Subsequently, we calculate the incremental change in stress at each time step within the slip window; the rate of change of the stress is proportional to the slip rate and can thus be used to determine additional slip. Eventually, the shear stress becomes lower than the failure threshold and no slip occurs on the fault. Later, the fault may slip in the opposite direction reducing the total offset on the fault. After one orbit, positive cumulative slip would mean a LL prediction for the fault, negative would be RL, and zero net slip implies no offset on the fault. In practice, we find that the failure stress in each slip direction is similar so the prediction is most dependent on the length of the slip window in each direction. Only in cases in which the fault spends equal time in LL and RL slip does the amount of initial slip play a role. This result is consistent with the results of Smith-Konter and Pappalardo (2008).

6.4 Results

The shell tectonics global predictions accounting for only eccentricity are shown in Figure 6.2. The predictions using tidal stresses that include a 1° obliquity and spin pole direction of 220° are shown in Figure 6.3. Both sets of predictions use the lower friction value of 0.2; predictions using the higher friction value are shown in Section 6.A1. In these plots, black represents fault azimuths that undergo left lateral slip, and light grey represents right lateral slip. The net slip goes to zero at transitions between left and right lateral regions. In the last column of each plot, we show a combination of the predictions made at each latitude over all longitudes. Here, dark grey indicates that both right and left lateral faults form within the span of longitudes tested for a given crack azimuth. To generate the predictions shown in Fig. 6.2 and 6.3, we use a relaxation rate of $1x10^{-10}$ s^{-1}, which is comparable to the Maxwell time of ice at ~130K. The relaxation rate will determine the magnitude of the accumulated offset per orbit. However, our predictions of slip direction and relative offset accumulation are insensitive to the relaxation rate over several orders of magnitude (see Section 6.A2 for an example).

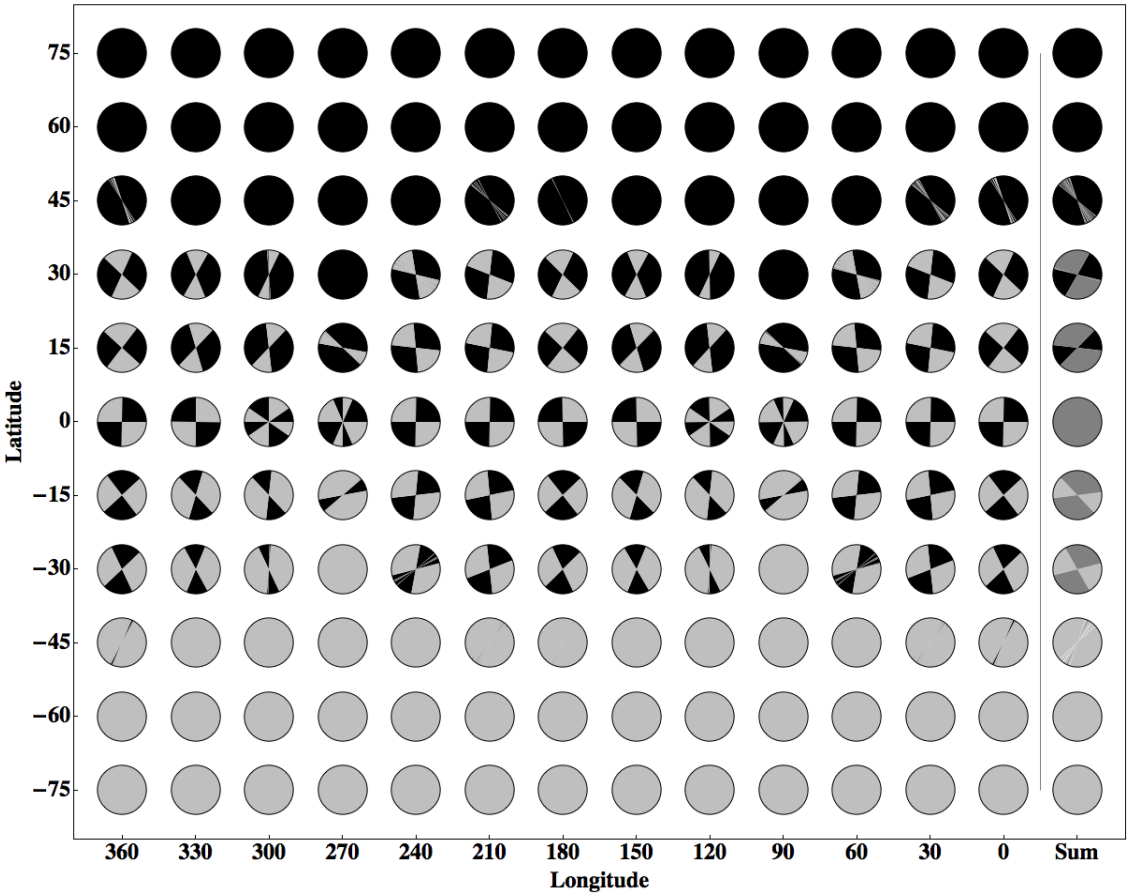

Figure 6.2: Shell tectonics predictions of slip direction with zero obliquity. Within each circle, black regions indicate crack azimuths along which we predict left lateral displacement; light grey represents right lateral fault azimuths. We predict no net slip at the boundaries between left and right regions. The last column shows the predictions summed over all longitudes, in which dark grey represents azimuths that could have right or left lateral displacement depending on their longitude at the time the displacement occurred. The pattern of slip direction generated using the shell tectonics model fits with the global observed pattern, in which left-lateral faults dominate in the far north, right lateral faults dominate in the far south, and there is a mixture of right and left lateral faults in between.

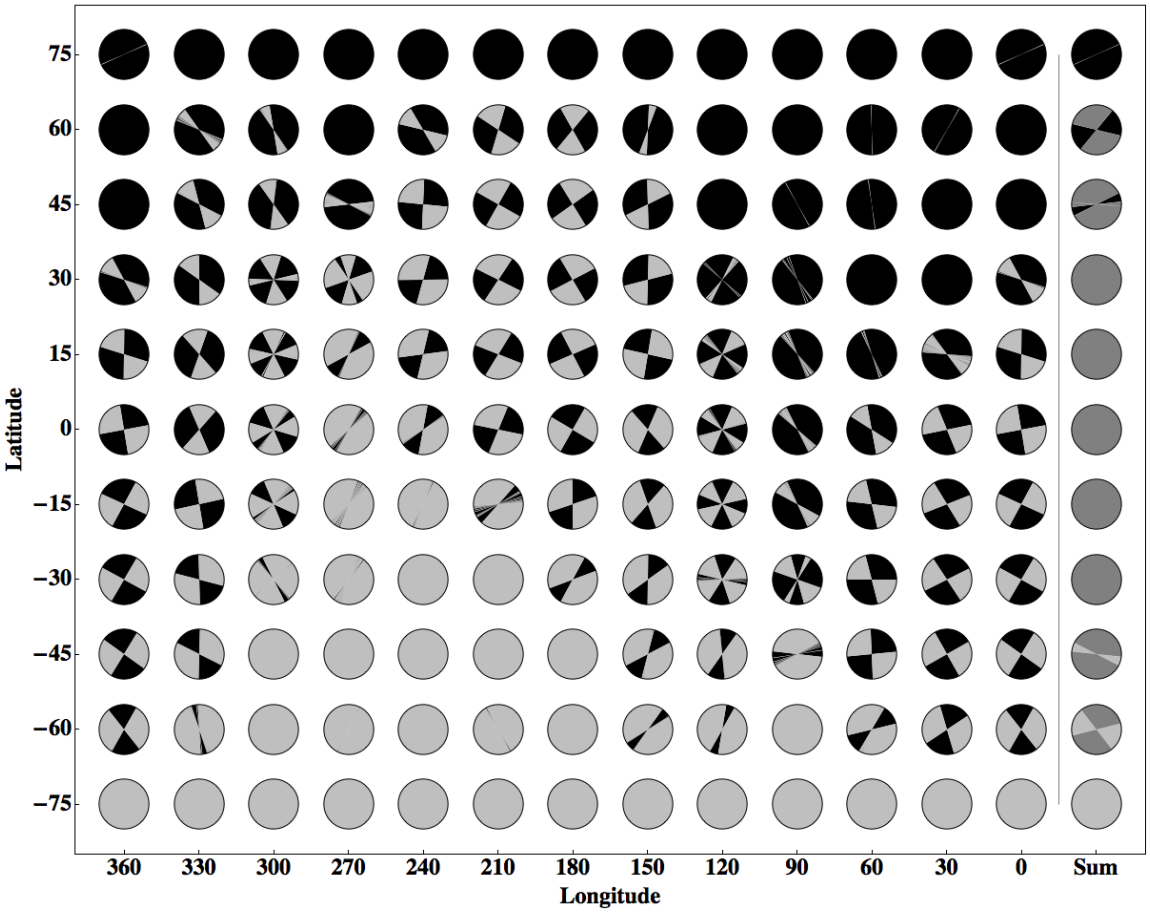

Figure 6.3: Shell tectonics predictions of slip direction with 1.0° obliquity at a spin pole direction of 220°. Black represents fault azimuths that will exhibit left lateral displacement, and light grey represents right lateral faults. The last column shows the predictions at all longitudes combined, in which dark grey indicates that either type of fault can form over the span of longitudes at which we calculated predictions. Obliquity breaks the longitudinal symmetry in the pattern of predicted slip direction, which is consistent with the observed differences in the observed fault populations of the leading and trailing hemispheres.

Without obliquity (Fig. 6.2), the shell tectonics model predicts regions with only left lateral faults at latitudes 60° and 75°, and right lateral faults at -60° and -75. Latitudes 45° and -45° are nearly exclusive, but there are a few longitudes with very narrow azimuth ranges that predict the opposite slip direction. At longitude 90°W and 270°W, on the other hand, the regions of exclusivity extend toward the equator to include +/-30°. At all other latitudes, there is a mixture of RL and LL faults predicted at every longitude. Using the higher friction value (0.6) produces very similar global predictions for this case, as shown in Section 6.A1.

With obliquity, a distinct hemispheric pattern emerges, as shown in Figure 6.3 (for $\varphi = 220°$). In the trailing hemisphere, around longitude 210°W, exclusively LL regions are predicted farther north than without obliquity while exclusively RL regions

are predicted closer to the equator. In the leading hemisphere (lon 90°W), the opposite occurs: LL-only regions begin farther south, and mixed regions extend into lower latitudes than without obliquity. With the higher friction value (see Section 6.A1), there are similar trends, but fewer locations are predicted to have exclusively LL or RL faults for all azimuths. The spin pole direction determines the longitudes at which the asymmetries in predictions would occur. Qualitatively, the pattern of offsets produced by obliquity appears consistent with the hemispheric differences in the observed strike-slip populations.

The predictions using the SKP-type model (without obliquity) are shown in Figure 6.4. In all regions, both left and right lateral faults are predicted to form with the slip direction depending on fault azimuth. Given a population of faults with random azimuths, this model should produce equal numbers of LL and RL faults at all latitudes and longitudes on Europa.

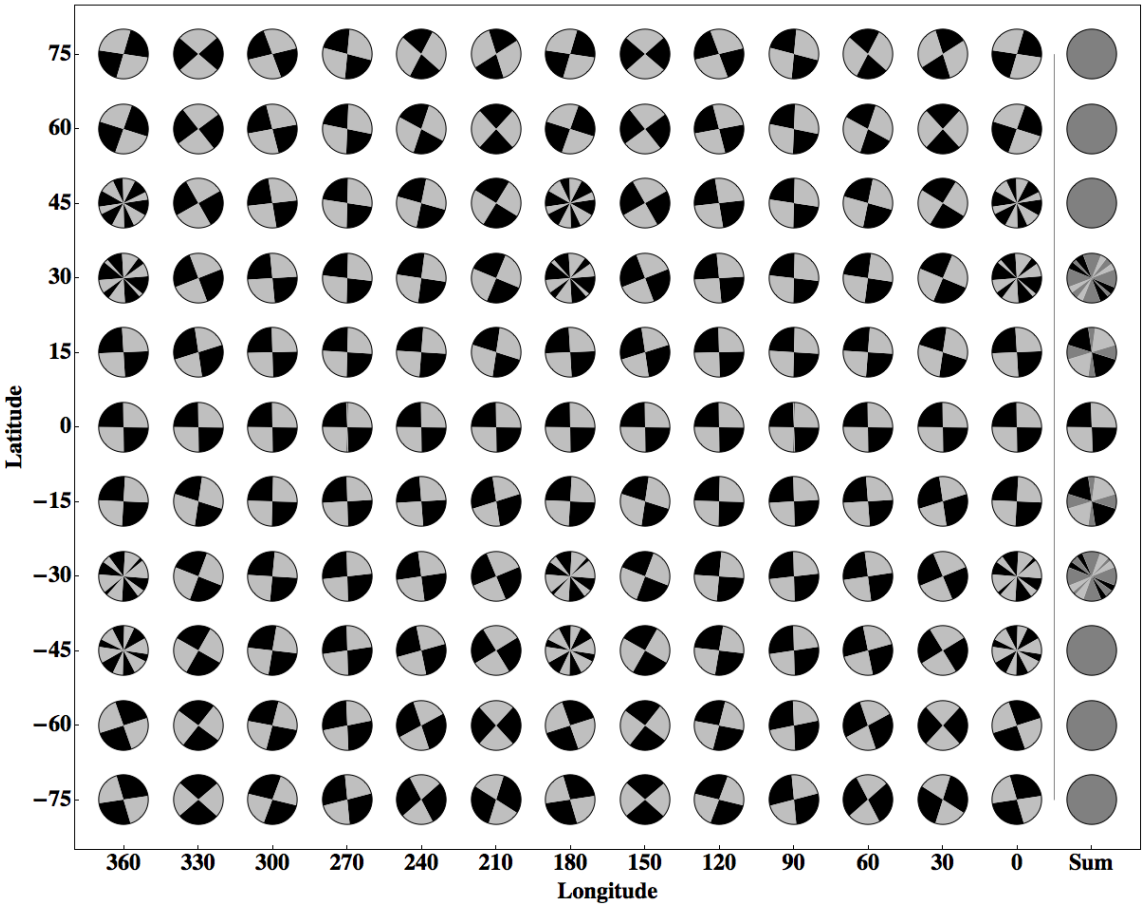

Figure 6.4: Model predictions of slip direction with zero obliquity using the SKP-type model. Black represents fault azimuths that will exhibit left lateral displacement, and light grey represents right lateral faults. The last column shows the predictions at all longitudes combined, in which dark grey indicates that either type of fault can form over the span of longitudes at which we calculated predictions. This model predicts roughly equal numbers of right and left lateral faults at any location given a random distribution of fault azimuths.

6.5 Discussion

6.5.1 Matching the slip directions of observed faults

To quantify the goodness of fit between the shell tectonics predictions and the observed faults, we made predictions of slip direction at the actual latitude, longitude, and azimuth of each observed fault (as reported in Rhoden et al., 2011 and in Chapter 5). As shown in Figures 6.2 and 6.3, the hemispheric differences in the observed fault population are better matched when obliquity is included in the tidal stress calculations. By testing predictions made with different spin pole directions against the individual observed faults, we find that an SPD of 220° produces a pattern that is most consistent with the observed leading-trailing asymmetry. Using high friction, the slip directions of 70% of faults in the survey by Sarid et al. (2002) are correctly predicted at their current longitudes. Using the lower friction value, our fit improves to 75%. Rhoden et al. (2011) tested the tidal walking model predictions against the same survey of faults. They found that an obliquity of 1° and SPD of 270° could account for the slip directions of 69% of faults - their best fit without appealing to longitude migration. The underlying assumptions concerning fault slip are similar between the shell tectonics model and the tidal walking model. However, Rhoden et al. (2011) only tested every 90° of SPD whereas we tested at every 10°; that may account for the difference in optimal spin pole direction. The SKP-type model correctly predicts the slip directions of only 46% and 50% of the observed faults with eccentricity-only and with 1° of obliquity ($\varphi = 220°$), respectively. Because the SKP-type model does not produce a hemispheric asymmetry, the value of the spin pole direction does not significantly influence the goodness of fit to the observations.

In Figure 6.5, we show the regions included in the strike-slip survey by Sarid et al. (2002), with different colors representing the percentage of fault slip directions accurately predicted with the shell tectonics and SKP-type models. The total number of faults in each region is also listed on shell tectonics model graphic. The numbers are the same for the SKP-type model. The shell tectonics model performs well in most regions but has trouble in some areas of mixed LL and RL faults. The SKP-type model predicts mixed faults in all regions, so it performs best in mixed regions and worst in regions where one slip direction is observed more than the other.

6.5.2 Matching the azimuth distribution of observed faults

Using shell tectonics, we calculate the net fault offsets that are predicted to accumulate during each orbit. Although the absolute magnitudes of these offsets depend on model parameters, we can compare the relative accumulation rates along faults. We find that, within a given region, faults with certain azimuths are predicted to develop larger offsets per orbit than others. Faults at these azimuths should be easier to identify as having strike-slip displacement. The shell tectonics model thus predicts differences in observed fault azimuth distributions in different regions based on the relative accumulation rates. Some regions within the strike-slip survey do imply a preferred direction, such as the left lateral faults at 75°N that trend mostly east-west (Figure 5.2). However, fault at most azimuths are observed in the equatorial regions at longitude 210°.

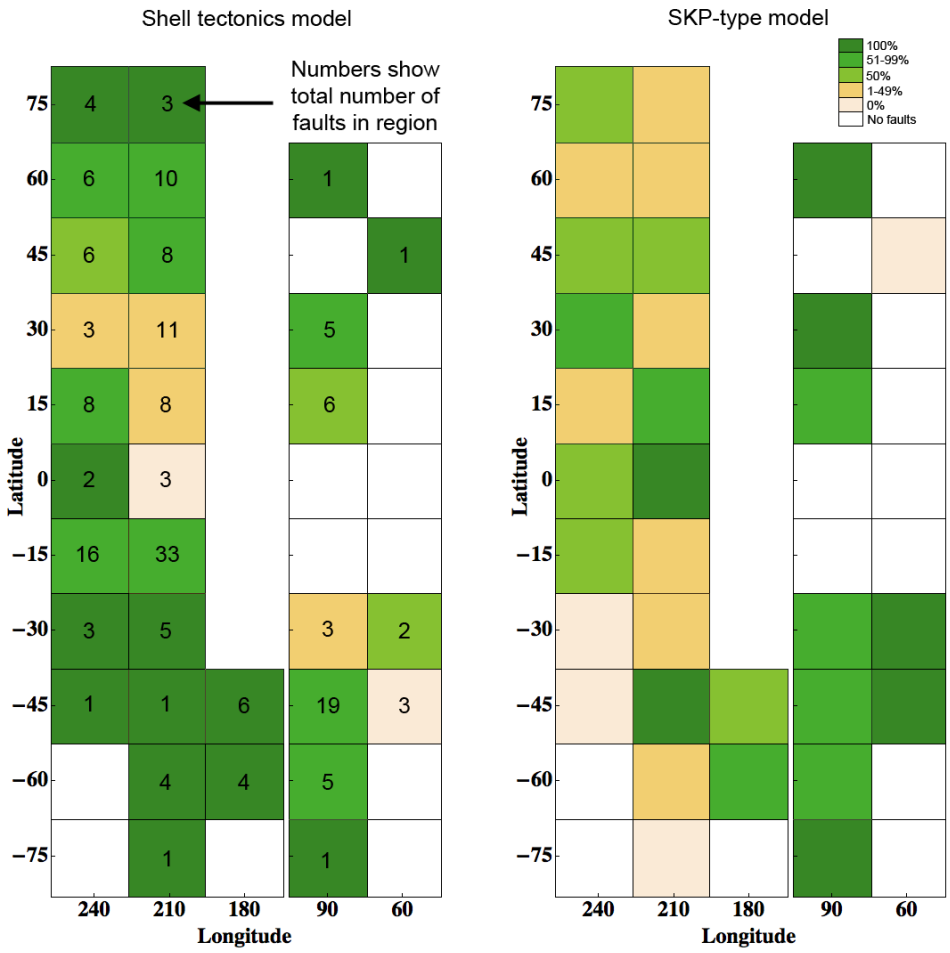

Figure 6.5: The regional accuracy of the predictions of fault slip direction using the shell tectonics model (left) and SKP-type model (right) with an obliquity of 1.0° and a spin pole direction of 220°. The shading represents the percentage of faults with slip directions that were accurately predicted with each model. The number of faults in each region is shown in the shell tectonics model graphic; the numbers are the same for the SKP-type model. Regions that are not shaded contain no observed faults.

We apply a statistical test to determine the extent to which the shell tectonics model can account for the azimuth distribution of the observed strike-slip fault population. In Figure 6.6, we show the observed fault azimuths from Figure 5.2 embedded within an outer annulus that displays the relative offset accumulation rate in the region from the shell tectonics model. Red represents the fastest (or largest) accumulation of LL slip, blue shows the fastest (or largest) accumulation of RL slip, and white regions may produce either LL or RL faults (as shown in Figure 6.3) but at a reduced rate compared to other azimuths. These rates were calculated using the parameter values that provide the best fit to the global pattern ($\varepsilon = 1°$, $\varphi = 220°$, $f = 0.2$).

Figure 6.6 shows that in some regions there should be preferred orientations at which offsets grow more rapidly. We can calculate the probability of producing the observed distribution of fault azimuths with the model shown in Figure 6.6, as follows.

For a given region (one circle in Figure 6.6), we can construct a curve of the offset accumulation rate with azimuth. Normalizing the curve converts the rates to probabilities. Figure 6.7 shows the probability curve for latitude 75°N and longitude 210°W as an example. In this region, faults of all azimuths are predicted to accumulate LL offsets; the peak in probability from ~80° to ~135° yields a prediction that more faults will be observed at these azimuths. Following this approach, it is straightforward to calculate the probability of forming each fault in the observed strike-slip population based on its binned latitude and longitude and its azimuth, rounded to the nearest degree. To compute a probability for all the faults in the survey, the probabilities for each fault are multiplied. The SKP-type model also yields net offsets along faults, so we use the same approach to test the probability of that model producing the observed fault population.

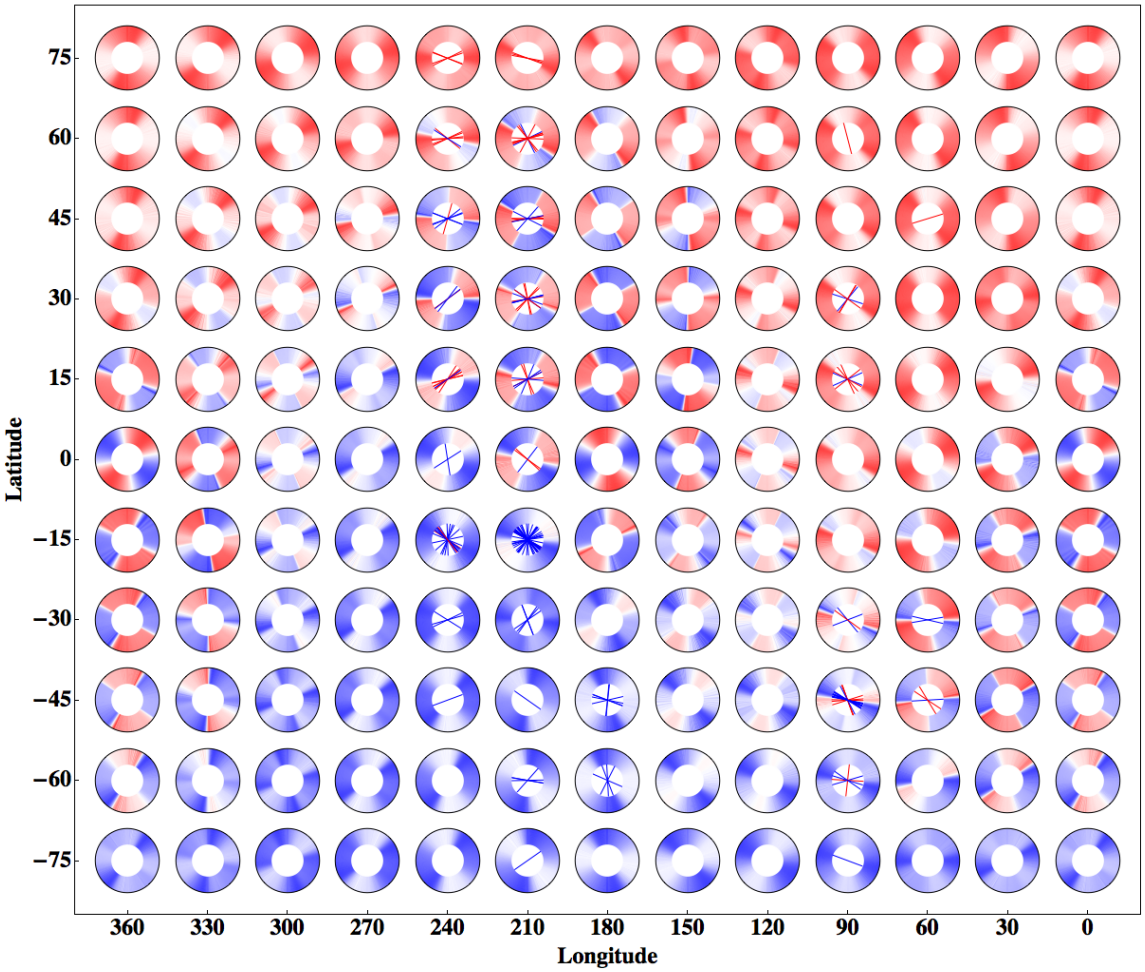

Figure 6.6: Relative rates of offset accumulation for a given region using the shell tectonics model (Obliquity 1°, SPD 220°) are shown in an annulus surrounding the observations from Figure 1. The gradient of rates goes from fast accumulation of left lateral slip (bright red) to fast accumulation of right lateral slip (bright blue). White can represent slip in either direction but at a reduced pace compared to other azimuths. The differences in accumulation rate may give rise to an observation bias within the fault population. Faults that accumulate slip faster than neighboring faults should be easier to identify.

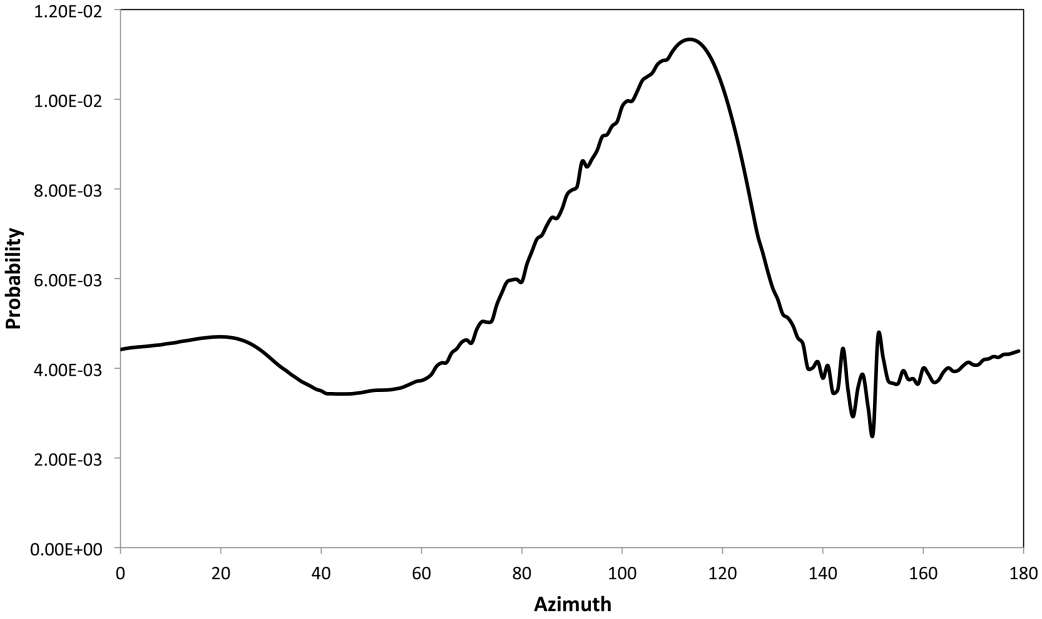

Figure 6.7: The probability versus azimuth curve for 75°N, 210°W based on the relative offset accumulation rates predicted with the shell tectonics model for an obliquity of 1.0° and a spin pole direction of 220°.

Neither the shell tectonics model nor the SKP-type model correctly predicts the slip directions of all of the observed faults. A fault with a slip direction that is not accurately predicted has a zero probability of forming with the model. Because we take the product of the individual fault probabilities to compute the probability of the model producing all of the observations, we must either exclude the faults with slip directions that are not accurately predicted or include a population of faults that formed with random orientations. If a fault had an equal likelihood of forming at any azimuth and either slip direction, the probability of generating that fault would be (1/360). The probability of generating a set of faults would be $(1/360)^n$, where n is the total number of faults.

We first test the probability of forming the observed population with a two-component model, in which some faults formed via the shell tectonics or SKP-type model and some formed at random orientations through some other process. The probability of forming each observed fault, P_{obs}, is:

$$P_{obs} = f_r/360 + (1 - f_r)*P_{model} \quad (6.3)$$

where f_r is the fraction of faults that formed at random orientations and P_{model} is the probability of forming the fault with the model (either shell tectonics or SKP-type) using the offset accumulation rates described above. As shown in Figure 6.8, the two-component model with the highest probability of forming the observed fault population is one in which half the faults were created via shell tectonics and half were created at random azimuths. The SKP-type model performs best when 75% of the faults are part of the random set; the probability of this model creating the observed fault population is lower than the best overall model by a factor of 10^{20}.

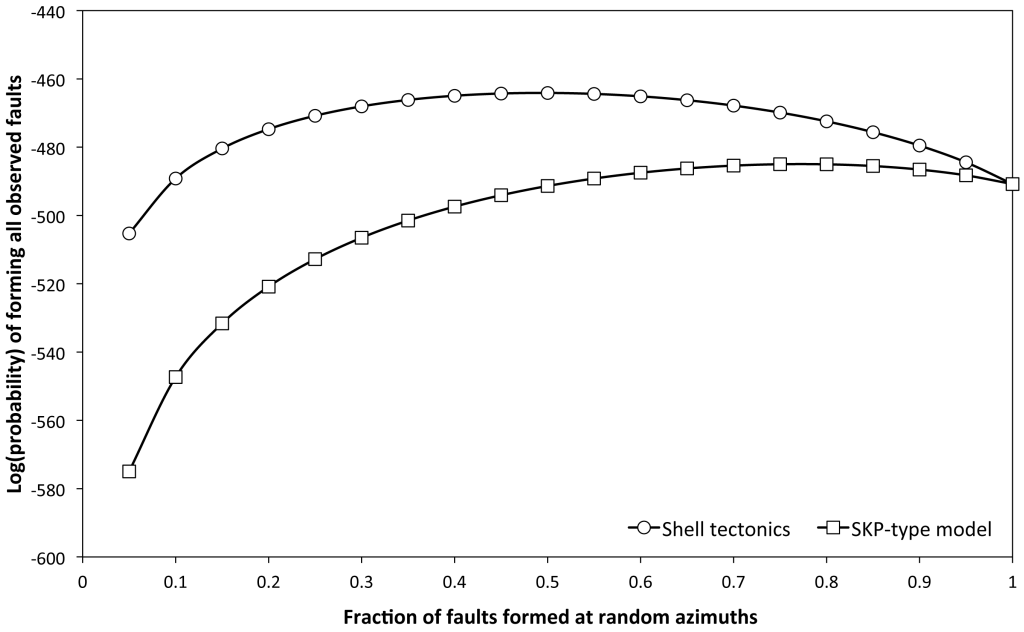

Figure 6.8: The probabilities of forming the observed fault population using a two-component model for the shell tectonics (circles) and SKP (squares) models. In the two-component test, we assume that the slip directions and azimuths at which some offsets form are determined by the shell tectonics or SKP-type model while others are formed with random slip directions and azimuths. In the highest probability model, half the observed faults are formed via shell tectonics and half are formed randomly. The highest probability model that uses the SKP-type model requires that 75% of the observed faults formed at random orientations.

With both models, as the fraction of randomly-oriented faults approaches zero, the probability of either model forming the observed population decreases because the faults with the wrong predicted slip direction can no longer be accounted for. The population of randomly-oriented faults may reflect a population of faults that have migrated in longitude since their formation. In addition, a region may contain faults with different ages. An older fault could have built up enough offset over time to appear more prominent than a young fault even if the young fault could develop a net offset more quickly. With enough sequence information, perhaps a history of offset development and longitude migration could be pieced together. This would inform us as to the rate of non-synchronous rotation of the surface and the rate of growth and destruction of strike-slip offsets. Unfortunately, limited imagery makes sequencing a difficult task. Many areas simply do not have enough unambiguous cross-cutting relationships to fully constrain the formation sequence in a given region (e.g. Sarid et al., 2006). If additional imagery of at least the ~250 m/pix resolution of the regional mapping imagery were obtained, more complete sequencing may be possible.

The two-component analysis reflects the ability of the model to predict both the correct slip directions along faults and to generate the azimuth distribution of the faults. However, we would like to specifically investigate the potential of shell tectonics to produce the observed azimuth distribution. To do this, we include only those faults with

slip directions that are accurately predicted at their current locations. We compute the probabilities of forming the observed azimuth distributions in each of the latitude/longitude bins from Figure 5.2, using the offset accumulation rates predicted by shell tectonics. To compute a reference probability, we again use a model that assumes exclusively randomly-oriented faults. To determine the regional probability, we multiply the probabilities for each observed fault based on the offset accumulation curves, as described in section 6.5.1. The random model probability is $(1/360)^n$, but now n is different for each region. This approach allows us to determine regions in which the shell tectonics model performs especially well or especially poorly.

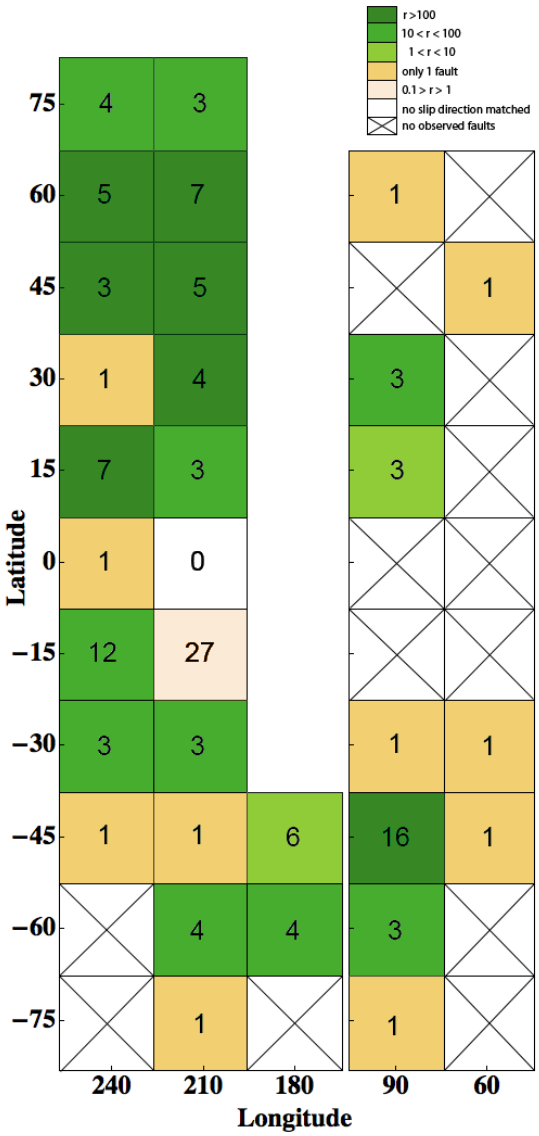

Figure 6.9: The regional ratios of the probability of forming the observed faults using the shell tectonics model to that of a model that assumes random orientations and slip directions. This analysis includes only those faults with slip directions that were accurately predicted with the shell tectonics model; the number displayed within each region is the number of correctly predicted faults. Regions in shades of green represent regions in which the shell tectonics model outperforms the random model. Regions in yellow contain only one fault, so their usefulness is limited. The area shown in red is the one region that has more than one fault and is better explained by the random model than the shell tectonics model.

In Figure 6.9, we show the regions in which faults were mapped by Sarid et al. (2002) with a color bar that indicates the ratio of the shell tectonics probability to the random model probability. A value greater than 1 means that the observed azimuth distribution can be better reproduced by the shell tectonics model than by a random model. In this figure, the number of correctly predicted faults is listed in each region.

There is only one region in which there is more than one fault and the observations support the random model over the shell tectonics model: longitude 210°W, latitude 15°S. Based on the relative offset accumulation rates in this region, we would not expect to observe offsets along faults with azimuths between 20° and 80°. However, 12 out of the 27 faults included in the analysis of this region have azimuths in this range. The region is shown in Figure 6.10a. Faults with slip directions and azimuths that are well-explained by the shell tectonics model are marked in white; faults with black dots have azimuths that are much less likely to be observed according to the model (mapping based on Sarid et al., 2002).

This region is complex; geologic mapping and reconstructions indicate that both extension and compression have contributed to the formation of bands in this area (Sarid et al., 2002; Patterson et al., 2006). It is possible, therefore, that some faults in this region were not formed as a direct result of tidal shear stress. For example, in Figure 6.10b, we show one of the faults in more detail. This fault connects with a dilational band shown in white. As the band opened along the east-west portion (as indicated by the arrows in Fig. 6.10b), it would have led to right-lateral slip along the north-south portion. It appears that this fault was created as a by-product of extension, and our model correctly indicated that it was unlikely to have been produced by tidal shear stress. More in depth examination of this region may reveal that many of these faults were similarly formed. This would enhance our understanding of the complex tectonic evolution of this region and allow more accurate testing of tidally-driven strike-slip fault models.

6.5.3 Additional implications

Using the shell tectonics model and either value of the friction coefficient, we are able to generate predictions that fit the observed pattern of strike-slip faults on Europa. With obliquity ($\varepsilon = 1°$), the differences in the leading and trailing populations can also be explained. Thus, consistent with the findings of Rhoden et al. (2011), polar wander is not necessary to explain strike-slip fault observations when the effects of obliquity are included in calculations of the stress field. Also consistent with Rhoden et al. (2011), we find that the formation timescale of strike-slip must be fast relative to the NSR timescale in order for the differences in the leading and trailing hemispheres to be preserved. As shown in the "Sum" column of Figure 6.3, rapid NSR should smear out the longitudinal variations in slip direction leading to mixed LL and RL faults at most latitudes and all longitudes.

Tidal stresses that include obliquity are typically about 100 kPa. If faults are only allowed to slip when in tension (such as in the tidal walking model) the compressive stress generated by the overlying ice would exceed this value below about 100 m, and faults would be clamped throughout the entire orbit. In the shell tectonics model, as well as the SKP model, a fault can slip in both tension and compression as long as the accumulated shear stress is larger than the Coulomb failure threshold. Using our best-fit shell tectonics model ($\varepsilon = 1°$, $\varphi = 220°$, f = 0.2), faults could still slip with a compressive overburden stress corresponding to a depth of 400-500m depending on location. Hence, based on the assumptions in the shell tectonics model, we can only really assess the behavior of this uppermost portion of the ice shell. To expand our analysis to the whole ice shell, we would need to integrate the effects of overburden stress and depth-dependent rheology into calculations of the timing and amount of slip with depth.

The statistical analyses presented in sections 6.5.1 and 6.5.2 indicate that the shell tectonics model can better reproduce the slip directions and azimuth distributions of the observed fault population on Europa than the SKP-type model. However, it is important to point out that we have used a simplified parameterization of the model presented by Smith-Konter and Pappalardo (2008). Our work tested the underlying assumptions of how fault slip is generated, which are different between the shell tectonics model and the model presented by Smith-Konter and Pappalardo (2008). Due to these simplifications, we cannot fully assess the potential of the model presented by Smith-Konter and Pappalardo (2008) to produce offsets on Enceladus or Europa. We can only conclude that a model that includes the fault slip behavior they assumed is less likely to generate the observed fault population on Europa than one that includes the fault slip assumptions in the shell tectonics model.

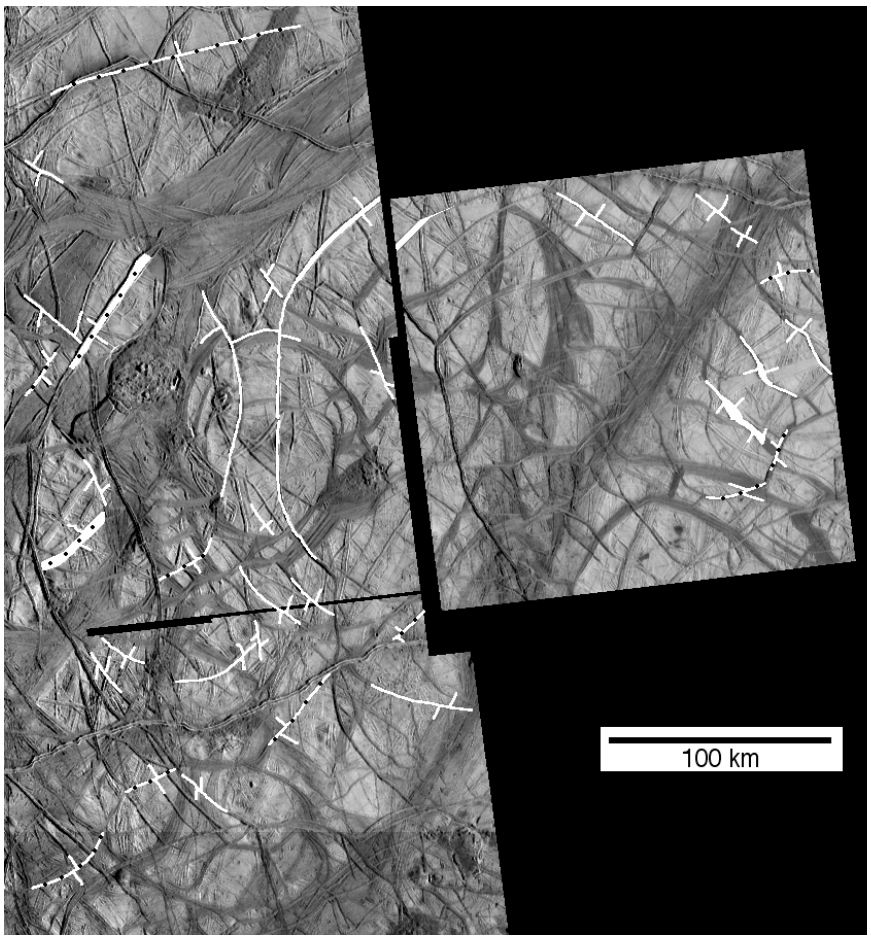

Figure 6.10: (a) A complex tectonic region in which the azimuth distribution is better explained by a model that assumes random orientations than by the relative offset accumulation rates predicted by the shell tectonics model. The shell tectonics model predicts that faults with azimuths of 30-80° would form offsets at a reduced rate compared with faults at other azimuths, perhaps leading to these azimuths being under-represented in the observations. It is possible that these faults formed in a different location or from a process other than tidal shear stress. Faults with slip directions and azimuths that are well-explained by the shell tectonics model are shown in white; faults with black dots have azimuths that are much less likely to be observed according to the model.

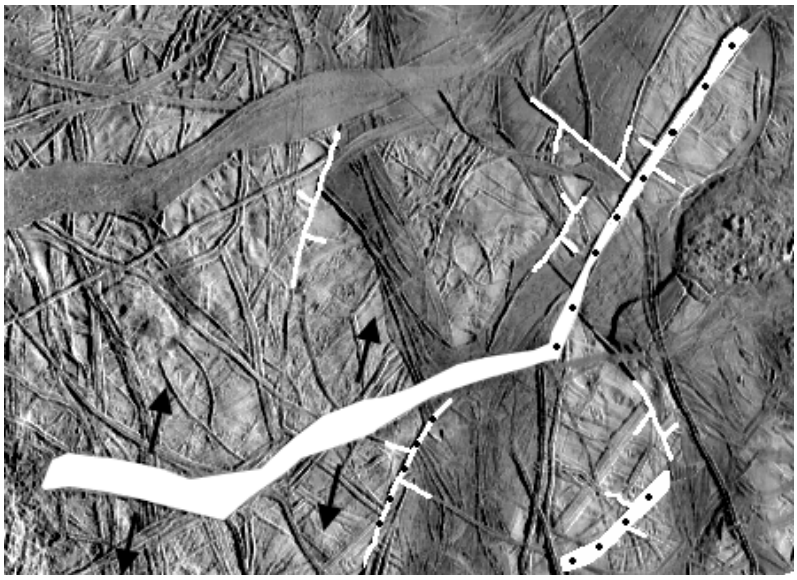

Figure 6.10: (b) A fault with an azimuth that is inconsistent with the shell tectonics model. The fault is connected to a dilational band and likely formed as a result of extension along the east-west trending portion (to the left in this image, as marked by the black arrows), rather than tidal shear stress.

6.6 Conclusions

Shell tectonics provides a mechanical framework to evaluate the response of faults within an elastic shell to periodic tidal stress. Shell tectonics explicitly accounts for the release of accumulated stress due to slip on the fault when computing subsequent fault stress and slip. Stress relaxation in the shell is also included explicitly. Shell tectonics includes a more physical treatment of fault mechanics than the tidal waking model (Hoppa et al., 1999c) and can operate much deeper into the shell because it uses a Coulomb failure criterion to determine when and if failure occurs. However, both the shell tectonics and tidal walking models assume that, in general, slip on a fault will increase as shear stress increases and will decrease as the shear stress decreases. The model of Smith-Konter and Pappalardo (2008) relies on a different assumption when evaluating fault slip. To test this fundamental difference in assumptions, we developed a simplified version of the SKP model and tested both the shell tectonics and SKP-type models against the population of observed faults on Europa from Sarid et al. (2002).

When applied to Europa, both the tidal walking (Rhoden et al., 2011) and shell tectonics models can produce global predictions of slip direction that display the same pattern as observed strike-slip faults. Consistent with previous work (Rhoden et al., 2011), we find that an obliquity of order 1° can alter tidal stress such as to reproduce the differences in strike-slip populations observed in the leading and trailing hemispheres. The shell tectonics model accurately predicts the slip directions on 75% of the observed faults from the survey by Sarid et al. (2002). In comparison, the SKP-type model can fit the slip directions of 50% of observed faults.

Using the predictions of relative accumulation rates from the two models allows us to determine whether the azimuth distribution of the observed faults can be explained in addition to their slip directions. This analysis shows that both models require a population of faults that formed at random orientations (50% for the shell tectonics model and 75% for the SKP-type model) in order to explain the slip directions and azimuth distribution of the observed faults. The probability of forming the observed fault population is always higher with the shell tectonics model than the SKP-type model.

We also determine the regional probabilities of forming the observed fault population in accordance with the relative accumulation rates as predicted by shell tectonics and a model in which all faults form at random azimuths. Comparison with the azimuths of observed faults strongly suggests that the differences in relative accumulation rates have led to preferred orientations within the strike-slip survey because faults with larger offsets are easier to identify. Of the 32 regions containing strike-slip faults, the shell tectonics model outperforms the random model in all regions containing more than one fault, with the exception of a complex tectonic region in which many faults may have formed through extension and compression. Further examination of this region as well as investigation of the role of overburden and other depth-dependencies on fault slip would likely improve our understanding of strike-slip fault formation on Europa. Shell tectonics may also be applicable to the formation of, and motion along, the Tiger Stripe fractures on Enceladus with implications for heating and plume generation, as these processes have already been linked to tidal stress (Nimmo et al., 2007; Smith-Konter & Pappalardo; Hurford et al., 2007b).

6.A1 Global predictions with higher friction

Figure 6.A1: Shell tectonics predictions of slip direction using the higher friction value of 0.6 with (a) only eccentricity and (b) an obliquity of 1° and SPD of 220°. Within each circle, black regions indicate crack azimuths along which we predict left lateral displacement; light grey represents right lateral fault azimuths. The net slip goes to zero at the boundaries between left and right regions. The last column shows the predictions summed over all longitudes for each latitude. Dark grey represents azimuths that could have right or left lateral displacement depending on their longitude at the time the displacement occurred. The spatial pattern of predicted slip direction is consistent with the global observed pattern of faults on Europa. With obliquity (b), the differences in the populations of the leading and trailing hemispheres can also be reproduced. Using high friction and obliquity, the shell tectonics model accurately predicts the slip directions of 70% of observed faults in the survey by Sarid et al. (2002).

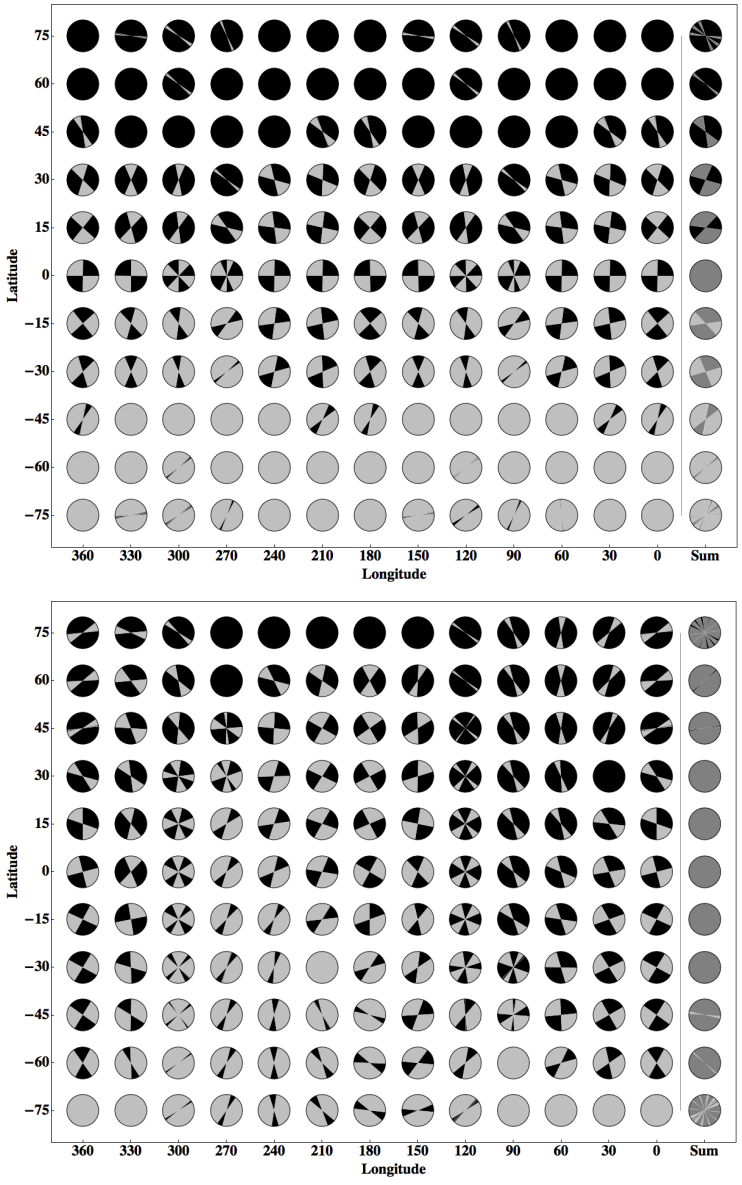

6.A2 The effects of the decay rate

Figure 6.A2: Probability versus azimuth curves for several values of the decay rate. As the decay rate is lowered, numerical noise increases. However, the effect is small. The decay rate controls the absolute magnitude of the offsets accumulated along faults during each orbit. It does not alter the predictions of slip direction or significantly affect the relative accumulation rates used in the statistical tests described in sections 6.5.2 and 6.5.3. The method by which this type of plot is generated is described in detail in section 6.5.2, and Figure 6.7 is the same curve shown here with the decay rate of $1x10^{-10}$.

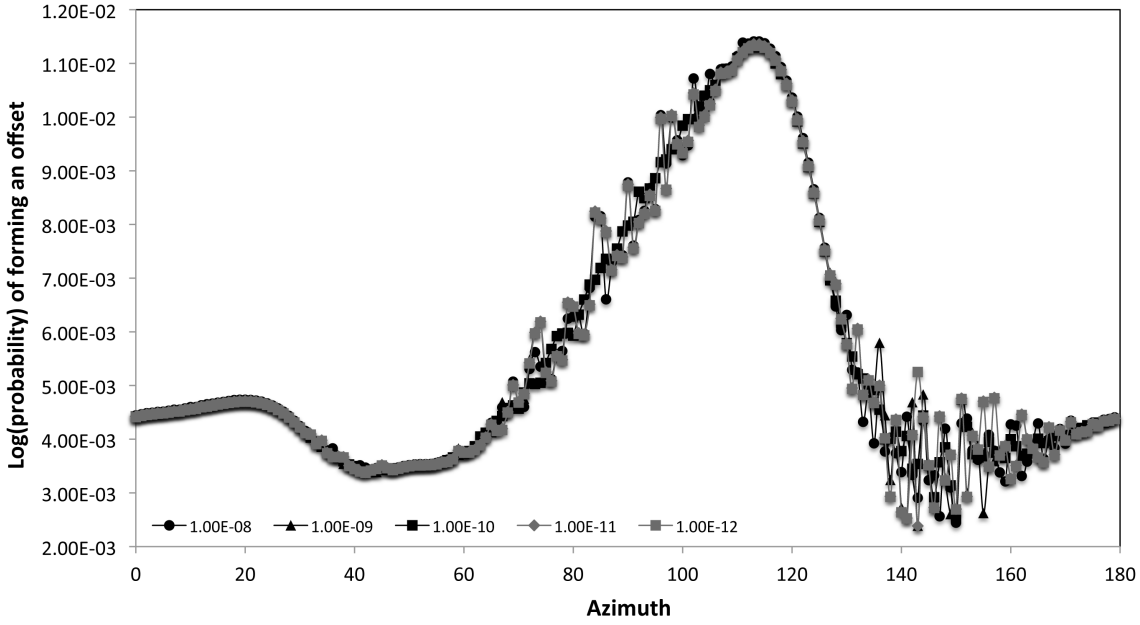

Chapter 7: The rotation and fracture history of Europa

7.1 Implications for Europa's rotation

The results of the studies described in the preceding chapters indicate that, at the time the observed cycloids and strike-slip faults formed, Europa had an obliquity of ~1°. The cycloid modeling work presented in Chapter 3 shows vastly improved fits to observed cycloids in the southern hemisphere and to equatorial cycloids when a small obliquity is included in the tidal stress calculations. Both the tidal walking model (Chapter 5) and the shell tectonics model (Chapter 6) can reproduce the global pattern of observed strike-slip faults using tidal stresses with an obliquity of 1°. Patterns of boxy cycloids (Hurford et al., 2007a) and chaos features (Riley et al., 2006) also display hemispheric asymmetry consistent with obliquity. True polar wander is not required to reconcile predictions with strike-slip observations when obliquity is included in the tidal model. In fact, the predicted locations of boxy cycloids would be farther from the location of observed boxy cycloids if the polar wander event invoked by Sarid et al. (2002) to explain strike-slip fault patterns had occurred (Hurford et al., 2007).

Each cycloid fit shown in Chapter 3 requires a different value of obliquity, which is consistent with the prediction of Bills et al. (2009) that the amplitude of the obliquity is time-variable. Using the best tidal model, as indicated by our statistical analysis, the obliquity values are 0.32°, 0.48°, 0.62°, 0.73°, 0.93°, and 1.35°, The strike-slip analysis presented in Chapter 5, using the tidal walking model, also shows that predictions improve if the obliquity value has varied from 1.0° to 1.2° throughout the formation of the observed fault population. In Chapter 6, using the shell tectonics model of strike-slip fault formation and an obliquity of 1.0°, we find that half the observed faults were likely to have formed by an alternative process or under different tidal stress conditions. A change in the value of the obliquity would alter the tidal stresses, perhaps accounting for these faults.

Europa's spin pole direction is also expected to change with time. Precession is supported by cycloid fits because each fit requires a different spin pole direction. However, individual cycloid paths do not appear to record a change in spin pole direction, so the rate of precession must be slow compared to the formation time scale of a cycloid. The spin pole direction also determines the longitudinal phase of the asymmetry in strike-slip fault predictions caused by obliquity, using either the tidal walking or shell tectonics models. Because hemispheric differences in the observed strike-slip fault population persist, the precession rate must also be slower than the formation time scale of strike-slip faults. When testing the shell tectonics model, we do not consider the effects of a precessing spin pole on the strike-slip fault predictions. As with the amplitude of the obliquity, however, a change in spin pole direction over the lifetime of the observed fault population would alter the stresses used to predict slip direction and relative accumulation rate.

Cycloid fits indicate a time-variable physical libration that is larger than expected by theory (c.f. Bills et al., 2009). A transient increase in physical libration could be caused by a large impact, for example, which could also lead to larger variations in the amplitude of the obliquity although this possibility has not been investigated in detail. The effects of a physical libration on strike-slip faults were examined in Chapter 5 using the tidal walking model, but the results are inconclusive. We do not assess the influence

of physical libration on the predictions made with shell tectonics model. The phase of the physical libration does not appear to change significantly with time as all cycloids reflect similar values; the physical libration indicated by cycloid fits is in phase with the eccentricity libration.

Good fits to observed cycloids require that the cycloids have migrated in longitude since their formation. Non-synchronous rotation of the ice shell, caused by Europa's eccentric orbit (Greenberg and Weidenschilling, 1984), is the presumed mechanism for this migration (e.g. Hoppa et al., 2001). However, stress from non-synchronous rotation is not indicated in cycloid fits. Four out of the six cycloids discussed in Chapter 3 require a minimum longitude translation between 64° and 76°; another requires at least 144°, and only one has a formation longitude near its observed longitude. Fitting all six cycloids would thus require a minimum of 144° of longitude migration. However, given the degeneracies in the stress field, we cannot differentiate between a cycloid formed at a given longitude, 180° of rotation away from that longitude (assuming also a 180° change in SPD), or any multiple of 360° away. Hence, these cycloids could have formed over many non-synchronous rotations of the surface.

In contrast, the differences in the observed strike-slip fault populations in the leading and trailing hemispheres require that non-synchronous rotation be slow compared to the formation time scale of strike-slip faults. Otherwise, the accumulation of faults formed at different locations would obscure the hemispheric pattern created by obliquity. The slip directions of observed strike-slip faults are better predicted using the tidal walking model if longitude migration is allowed. As described in Chapter 5, the slip directions of 90% of observed strike-slip faults would be correctly predicted if the faults formed over the last 90° of longitude migration and with an obliquity of 1.2°. This result is consistent with the idea that only a small amount of rotation has occurred during the development of these faults. Using the shell tectonics model, the slip directions of more faults can be fit at their current locations – 75% versus 68% with tidal walking – using an obliquity of only 1°. The additional constraints provided by the shell tectonics model calculations indicate that the slip directions and azimuths of half the observed faults are well-explained by the model. The remaining faults may have formed at other longitudes. Indeed, all but five faults have slip directions that would be accurately predicted using the shell tectonics model if an arbitrary amount of longitude migration is allowed.

The improvement in strike-slip fault predictions with either formation model is not proof of non-synchronous rotation however. Changes in obliquity and/or spin pole direction, physical libration, or local tectonic processes could all affect the way strike-slip faults form on Europa. Using the type of predictions we described in Chapters 5 and 6, there is not enough information to distinguish between a population of faults formed with a time-varying obliquity, for example, or longitude migration. The patterns of fault predictions are too similar. One way to determine which process is best supported by the observations would be to create a time sequence of the observed strike-slip faults. If non-synchronous rotation did move the faults over time, the oldest faults should require the most longitude migration while the youngest faults should require the least. If, instead, the fault patterns were created by a time-varying obliquity, the time sequence of faults should fit a cyclic pattern of obliquity variation. Lastly, if spin pole precession is altering the pattern of strike-slip fault formation, the spin pole direction should increase with fault age. Unfortunately, there are too few cross-cutting relationships between the faults in the

Sarid et al. (2002) survey to fully constrain their formation sequence (Sarid et al., 2006; 2007; 2006). It is not possible with the present data set to determine if strike-slip faults record a signal of non-synchronous rotation or time-varying obliquity, as do cycloids. Better spatial coverage with high resolution imagery is needed.

Although modeling of cycloids and strike-slip faults yield consistent results for obliquity, they appear to record different rotation histories. Cycloids indicate large amounts of longitude migration, perhaps even many rotations of the surface, while strike-slip fault patterns require much less than one rotation. As discussed in Section 5.4, lineament azimuths also imply many rotations (e.g. Sarid et al., 2005) although those results have not been evaluated with a stress field that includes obliquity. There are several possible ways of reconciling the results from cycloids and strike-slip faults:

1) Individual cycloid paths are very sensitive to the spatial and temporal changes in tidal stress. There are few locations at which a given cycloid could have formed. In contrast, most observed strike-slip faults could be fit over a wide range of longitudes. If the population of strike-slip faults actually formed more uniformly over ~90° of rotation, then the results would be more consistent with the cycloid results: most of the cycloids and strike-slip faults formed within the most recent 90° of non-synchronous rotation, and there are a few older features preserved in the tectonic record. However, this assumes the minimum longitude translation indicated by cycloid fits.

2) The longitude translations required to achieve good fits to cycloids may be the result of a missing component of the tidal stresses. Again, cycloids are more sensitive to the patterns of tidal stress than strike-slip faults, so the incompleteness of the tidal model would impact cycloids more. However, 50% of observed strike-slip faults have slip directions and azimuths that are not well-supported by the shell tectonics model, so even strike-slip faults may contain a signal of this extra component of stress. In Chapter 4, we assess the influence of Io-raised tides on Europa, which do not significantly alter cycloid paths. However, Ganymede is larger than Io and orbits exterior to Europa. Hence, the tidal bulges raised by Ganymede circulate in longitude. Unlike the tidal stresses from Io and Jupiter, there is no primary tide in the case of Ganymede. In that case, the tidal stresses generated by Ganymede could be much larger than those raised by Io. An avenue of future research would be to assess the influence of Ganymede-driven tidal stresses on cycloid formation on Europa. In addition, the ice shell is likely thinner at the equator than at the poles (Ojakangas and Stevenson, 1989b), which could alter the paths of cycloids and, thus, their most likely formation longitudes. Incorporating the effects of shell thickness variations into calculations of tidal stress would be a useful addition to cycloid modeling and may provide insight into the character of the ice shell at the time of cycloid formation.

3) The time scales for the formation and destruction of cycloids and strike-slip faults may be quite different, although this is difficult to assess. All the cycloids discussed in Chapter 3 have double ridges, which require either 10 years or ~10^4 years to develop depending of the formation mechanism invoked (Kattenhorn and

Hurford, 2007). The minimum non-synchronous rotation period is 12,000 years (Hoppa et al., 1999b). If ridges form in only 10 years, their presence does not provide an added constraint on the rotation cycloids have undergone since their formation. However, if ridges form slowly (~10^4 yrs), it would imply that the cycloids have experienced at least half a rotation since formation. That means cycloid EQ2, which requires only 3° of longitude translation to achieve the best fit ($\chi^2 = 24.72$), more likely formed 183° away from its present location and has migrated while developing its ridges. According to the shell tectonics and tidal walking models, strike-slip offsets increase each Europan day. More than 50% of strike-slip faults in the survey by Sarid et al. (2002) have offsets of a less than 3 km. We cannot determine the absolute rate of offset accumulation along faults, but it is conceivable that these offsets could have developed over a much shorter timescale than cycloids. Hence, cycloids may be older than the majority of strike-slip faults. Sequencing could again be useful to test this hypothesis. Another characteristic of strike-slip faults is that their behavior may change during migration. If a fault moved from a region in which it would develop a right-lateral offset to a location in which it would develop a left-lateral offset, the fault could perhaps be reactivated and change their direction of slip. Could the original offset then be erased through subsequent slip? In that case, faults may always preserve the most recent stress conditions even if they are much older and have undergone rotation.

Both cycloids and strike-slip faults suggest that Europa has more complex rotational dynamics than was previously thought. Large and time-varying obliquity and physical libration would both enhance tidal heating within Europa and could thus affect the interior structure and the state of the ice shell (Tyler, 2008; Hurford, 2009b). The biggest conundrum is the role of non-synchronous rotation on Europa. Does it actually move features in longitude, or is it a convenient way of making up for a missing element in our characterization of tidal stress? Incorporating Io-raised tides in the calculations of tidal stress did not improve fits or reduce the amount of longitude translation indicated by the fits, but stress from Ganymede may be more significant. Additional imagery of at least 250 m/pixel would enhance our ability to create time sequences, which help distinguish between the non-synchronous rotation, time-variable obliquity, and spin pole precession in the tectonic record. The large and variable values we find for obliquity and libration are best explained by the presence of an ocean at the time of cycloid formation, consistent with a large independent body of evidence for an ocean existing at present.

7.2 Cycloid and strike-slip fault formation on Europa

Obliquity allows cycloids to propagate across the equator without traveling perpendicular to the equator or having a boxy shape. It also allows breaks the symmetry that linked concavity with propagation direction (Hoppa et al. 2001). This likely has important implications for the interpretations of cycloid characteristics such as the multiple branches or splays observed along some cycloids (Sarid et al. 2004; Marshall and Kattenhorn 2005).

In the cycloid modeling work presented in Chapter 3, we use only one set of mechanical parameters for each cycloid in contrast to previous work. Although the

average values of the propagation speed, initiation threshold, and propagation threshold are similar to the results from past work (Hoppa et al. 2001; Hurford et al. 2007a), our results vary for each cycloid. It is possible that shell thickness variations lead to these differences. Changes in tidal stress with time could also alter the mechanical process of cycloid propagation. If the obliquity varies with time, for example, the amount of tidal heating would also change, perhaps causing the ice shell to thin or thicken with time. If cycloids are separated in age, they may reflect these changes.

In Chapter 6, we described a new model for strike-slip fault formation on Europa that uses the same underlying assumptions of fault slip direction as the tidal walking model (Hoppa et al., 1999c, 2000) but includes a Coulomb failure criterion, a quantitative assessment of slip and stress release on faults, and viscous relaxation. Use of the CFC makes the shell tectonics model applicable deeper within the shell where overburden stresses would restrict the fault to net compression throughout the orbit. Using the observed faults from the survey by Sarid et al. (2002), we test our new model, called shell tectonics, and a model based on Smith-Konter and Pappalardo (2008).

The predictions of slip direction using the shell tectonics model are similar to those of the tidal walking model because the underlying assumptions of fault slip direction are the same in both models. However, the shell tectonics model is better at reproducing the slip directions of the observed strike-slip faults at their current locations, correctly predicting the slip directions of 75% of observed faults with an obliquity of 1°. Using the SKP-type model an equal number of right and left lateral faults would be predicted to form in any region of Europa. This is contrary to the observed global pattern in which slip direction is strongly linked to formation location. Only 50% of faults have slip directions that are correctly predicted at their current locations using the SKP-type model and an obliquity of 1°.

Both the shell tectonics model and the SKP-type model predict relative offset accumulation rates for faults with different azimuths and locations. Based on these predictions, we find that both models require a population of faults that formed at random orientations to explain the slip directions and azimuth distribution of the observed faults. As shown in Chapter 6, the probability of forming the observed fault population is always higher with the shell tectonics model than the SKP-type model. Using shell tectonics, 50% of observed strike-slip faults have slip directions and azimuths that are well-explained. Using the SKP-type model, only 25% of the observed faults are well-explained; 75% must have formed by some other mechanism. Because obliquity and slip pole direction only weakly affect the predictions with the SKP-type model, differences in tidal stress with time are less likely to be able to account for faults that are not fit well by the model. The shell tectonics model outperforms the SKP-type model in reproducing the characteristics of the observed fault population, which strongly supports the underlying assumptions of the shell tectonics model and its predecessor, the tidal walking model.

There is one region in which there are many observed faults with azimuths that are not predicted to form with the shell tectonic model: longitude 210°W and 15°S. This is a region dominated by extension and compression (Sarid et al., 2002; Patterson et al., 2006); many of the observed strike-slip faults are associated with bands linked to these processes. Although the local tectonic activity in this region may perhaps explain the mismatch between predictions and observations, it is interesting to consider why this region in particular exhibits different behavior than elsewhere on Europa. It does lie on

the western edge of the so-called Wedges region of boxy cycloids, which often display band structure. Perhaps it is the proximity to the Wedges region that affects strike-slip fault formation here. Boxy cycloids are predicted to form as a result of tidal stresses; the location of observed boxy cycloids corresponds to tidal stresses that include obliquity (Hurford et al., 2009a). A second region of boxy cycloids is predicted to form just above the equator, centered at 30°W. However, this is an area that was not imaged at high enough resolution for mapping of strike-slip faults. If future missions enabled additional imagery at 250 m/pixel or better, this would be a useful target. We could then assess whether strike-slip fault formation near regions of boxy cycloids in, in fact, different from faulting in other areas. In the leading hemisphere, the entirety of regional mapping images between 15°N and 15°S show such a high prevalence of chaotic terrain that no other features can be mapped. Hence, we cannot compare fault behavior between the leading and trailing hemispheres either.

7.3 Expanding to other worlds

Modeling of cycloids and strike-slip faults on Europa has shown that the formation of these tectonic features depends sensitively on Europa's rotation state. This work is likely applicable to faults on other outer planet satellites such as Enceladus, Dione, Triton, and Miranda, and the dwarf planet Pluto, as all are thought to have ice-covered oceans (Hussman et al., 2006). Enceladus is a particularly interesting case. The present day heat flux, concentrated at the south pole, is at least 15GW (Spencer et al., 2010). Given its size and likely composition, the source of Enceladus' heat must be tidal, but neither the current eccentricity nor any orbital evolution model yet proposed can explain 15GW of heat (Meyer and Wisdom, 2008). Also at the south pole are four fractures, dubbed Tiger Stripes, that are anomalously warm even compared to the surrounding south polar terrain (Spencer et al., 2006; Spitale and Porco, 2007) and have been identified as the source regions of the plumes (Spitale and Porco, 2007). Daily-varying tidal stress, caused by Enceladus' eccentricity, is thought to have formed the Tiger Stripes and is the proposed mechanism for both heat and plume generation along them (Hurford et al., 2007b; Hurford et al., 2009b; Nimmo et al., 2007).

Because tides appear to be an integral part of Enceladus' thermal and geologic activity, it is important that the tidal stress field being used to calculate tidal heating, interpret tectonic features, and predict motion along tidally-driven fractures is correct and complete. For example, observations of the extent of plume activity did not always correspond to whether the Tiger Stripes would be experiencing tensile or compressive tidal stress (Hansen et al., 2008). This suggests that initial calculations of Enceladus' tidal stress field were too simplistic. In addition, eccentricity alone cannot account for the observed heat flow, producing a mere 0.12GW of tidal heat if Enceladus acts as a solid body (Porco et al., 2006; Yoder, 1979) and up to about 8GW if there is a global ocean (Hurford et al., 2009b).

The dynamical arguments supporting Europa's non-negligible obliquity (Bills, 2005; Bills et al., 2009) are also applicable to Enceladus, and physical libration of Enceladus has been predicted due to its shape and possible spin-orbit resonance (Wisdom, 2004). Cassini observations set the upper bound on the libration at 1.5° (Porco et al., 2006). If Enceladus acts as a solid body, theoretical arguments suggest the libration

may be an order of magnitude lower (Rambaux et al., 2010). Both obliquity and physical libration would alter the tidal stress that led to the formation of the Tiger Stripes and the subsequent stresses imposed on them throughout each orbit. Hence, the times during which the Tiger Stripes would experience tension and compression, and the corresponding predictions of plume activity, would change (Hurford et al., 2009b). These rotational effects also contribute significantly to tidal heating. For example, a libration amplitude at the 1.5° upper limit could generate ~40GW of tidal heat (Hurford et al., 2009b).

Observations of the north and south poles show an interesting dichotomy: old, heavily cratered terrain dominates in the north versus the warm and active south. Tectonic structures have also been observed in the leading and trailing hemispheres, centered near the sub-Saturn and anti-Saturn points (Crow-Willard and Pappalardo, 2010). Geologic mapping has shown that the leading hemisphere structures are younger than those in the trailing hemisphere, but both regions predate the south polar terrain (Crow-Willard and Pappalardo, 2010). A potential explanation for the difference in north and south polar activity is a disparity in shell thickness; these observations may even indicate a change in ice shell thickness variations over time.

Formation of the Tiger Stripes as tidally-driven tensile fractures and subsequent shear heating both require the ice shell to be relatively thin and overlie an ocean that is either global or local to the south pole (Hurford et al., 2007b; Hurford et al., 2009b; Nimmo et al., 2007). In addition, the south polar terrain is topographically depressed relative to Enceladus' mean elevation and displays a complex tectonic history that has been interpreted as evidence of subsidence due to melting (Collins and Goodman, 2007) or possibly polar wander (Matsuyama and Nimmo, 2008). If the south pole does have a locally thin ice shell overlying liquid water, then the Tiger Stripes may perhaps be penetrating all the way to the water reservoir and releasing the contents through the plumes; the Tiger Stripes can likely penetrate ice shells less than 25km and possibly as thick as 35km (Rudolph and Manga, 2009; Spencer et al., 2009). Estimates of the ice shell thickness at the south pole of Enceladus are as low as 5km (Roberts and Nimmo, 2008a).

These observations have led to several broad hypotheses about Enceladus' thermal evolution, tectonic history, and current interior structure (for a review, see Spencer et al., 2009). One possibility is that Enceladus began with a global ocean underlying an ice shell of uniform thickness. As Enceladus cooled, the ocean began freezing out in an asymmetric pattern. As with many models of Enceladus, this asymmetry is an ad hoc assumption based on the obvious observed dichotomy between the north and south poles. As the ocean thinned in the north, tidal stresses decreased there while both stress and tidal dissipation increased elsewhere (Tobie et al., 2008). Fracture systems observed in the leading and trailing hemispheres may have formed during this period, in which tidal heating and stress were enhanced but not enough to generate activity to the extent currently seen in the south polar region. As cooling continued, heat and stress became ever more concentrated at the south pole, perhaps even leading to local melting within the ice shell, subsidence of the south polar terrain, and the formation of the Tiger Stripe fractures due to tidally-induced tensile failure. Subsequent shear heating along the Tiger Stripes due to cyclic tidal stresses (Roberts and Nimmo, 2008b) or dissipation in the ocean (Tyler, 2008) could perhaps generate enough heat to prevent

freezing of the ocean at the south pole.

If the Tiger Stripes are tidally-driven fractures, modeling their formation can reveal the most likely stress field governing tectonic activity on Enceladus. There are two contributions to tidal stress that must be considered: rotation state and shell thickness variations. As we have shown for Europa, physical libration and obliquity contribute to tidal stress and affect the formation of tidally-driven fractures on ice-covered ocean moons (Hurford et al., 2009a; Hurford et al., 2009b; Rhoden et al., 2010; Chapter 3). Variations in ice shell thickness may also influence tidal stress patterns.

One approach would be to use the methodology I developed for Europa's cycloids (Chapter 3) to constrain the rotation state of Enceladus by modeling the Tiger Stripes as tidally-driven fractures. This approach could also be expanded to include the effects of a non-uniform ice shell thickness, which would be useful for future work on Europa as well. Constraining Enceladus' rotation state and ice shell thickness variations will allow a more precise determination of tidal stresses on Enceladus, which can be used to generate predictions of plume eruption timings along the Tiger Stripes, calculate the contribution of Enceladus' rotation state to its tidal heating, and determine the past and present structure of the ice shell that could account for both the Tiger Stripes and the tectonic structures observed elsewhere on Enceladus. This work would enhance our understanding of Enceladus' rotation, heating, and tidal-tectonic processes, and constrain Enceladus' interior structure and evolution, plume dynamics, and astrobiological potential.

References:

Anderson, J.D., Schubert, G., Jacobson, R.A., Lau, E.L., Moore, W.B., Sjogren, W.L., 1998. Europa's Differentiated Internal Structure: Inferences from Four Galileo Encounters. Science 281, 2019-2022.

Bassis, J.N., Coleman, R., Fricker, H.A., Minster, J.B., 2005. Episodic propagation of a rift on the Amery Ice Shelf, East Antarctica. Geophys. Res. Lett. 32, DOI: 10.1029/2004GL022048.

Beeman, M., Durham, W.B., Kirby, S.H., 1988. Friction of Ice. J. Geophys. Res. 93, 7625-7633.

Bills, B.G., 2005. Free and forced obliquities of the Galilean satellites of Jupiter. Icarus 175, 233-247.

Bills, B.G., Nimmo, F., Karatekin, O., Van Hoolst, T., Rambaux, N., Levrard, B., Laskar, J., 2009. Europa Rotational Dynamics of Europa. In: W. McKinnon (Ed.), Europa.

Carr, M.H. and 21 colleagues, 1998. Evidence for a subsurface ocean on Europa. Nature 391, 363-365.

Collins, G.C. and J.C. Goodman, 2007. Enceladus' south polar sea. Icarus 189, 72-82.

Crow-Willard, E.N. and R.T. Pappalardo, 2010. Global geological mapping of Enceladus. LPSC #41, Abs. #2715.

Dennis, J.E. and R.B. Schnabel, 1983. Numerical methods for unconstrained optimization and non linear equations. Prentice Hall, Englewood Cliffs, NJ.

Fagents, S.A., Greeley, R., Sullivan, R.J., Pappalardo, R.T., Prockter, L.M., and The Galileo SSI Team, 2000. Cryomagmatic Mechanisms for the Formation of Rhadamanthys Linea, Triple Band Margins, and Other Low-Albedo Features on Europa. Icarus 144, 54-88.

Figueredo, P.H. and Greeley, R., 2000. Geologic mapping of the northern leading hemisphere of Europa from Galileo solid-state imaging data. J. Geophys. Res. 105, 22629-22646.

Freund, L.B., 1990. Dynamic Fracture Mechanics. Cambridge University Press, New York.

Gammond, P.H., Klefte, H., and Clouter, M.J., 1983. Elastic Constants of Ice Samples by Brillouin Spectroscopy. J. Phys. Chem. 87, 4025-4029.

Geissler, P.E. and 16 colleagues, 1998. Evolution of Lineaments on Europa: Clues from

Galileo Multispectral Imaging Observations. Icarus 135, 107-126.

Goldsby, D.L. and D.L. Kohlstedt, 2001. Superplastic deformation of ice: Experimental observations. J. Geophys. Res. 106, 11017-11030.

Goldreich, P.M. and J.L. Mitchell, 2010. Elastic shells of synchronously rotating moons: Implications for cracks on Europa and non-synchronous rotation on Titan. Icarus 209, 631-638.

Greenberg, R., 1982. Orbital evolution of the Galilean satellites. In: Morrisson, D. (Ed.), The Satellites of Jupiter, Univ. of Arizona Press, Tucson, AZ.

Greenberg, R. and Weidenschilling, S.J., 1984. How Fast Do Galilean Satellites Spin? Icarus 58, 186-196.

Greenberg, R. and 9 colleagues, 1998. Tectonic processes on Europa – Tidal stresses, mechanical response, and visible features. Icarus 135, 64-78.

Greenberg, R., Leake, M.A., Hoppa, G.V., Tufts, B.R., 2003. Pits and uplifts on Europa. Icarus 161, 102-126.

Groenleer, J. and S.A. Kattenhorn, 2008. Cycloid crack sequences on Europa: Relationship to stress history and constraints on growth mechanics based on cusp angles. Icarus 193, 158-181.

Hansen, C.J., Esposito, L.W., Stewart, A.I.F, Meinke, B., Wallis, B., Colwell, J.E., Hendrix, A.R., Larsen, K., Pryor, W., Tian, F., 2008. Water vapour jets inside the plume of gas leaving Enceladus. Nature 456, 477-479.

Hastings, W.K., 1970. Monte Carlo sampling methods using Markov chains and their applications. Biometika 57, 97-109.

Head, J.W., Pappalardo, R.T., and Sullivan, R., 1999. Europa: Morphological characteristics of ridges and triple bands from Galileo data (E4 and E6) and assessment of a linear diapir model. J. Geophys. Res. – Planets, 104, 24223-24236.

Hoppa, G.V., Tufts, B.R., Greenberg, R., Geissler, P.E. 1999a. Formation of Cycloidal Features on Europa. Science 285, 1899-1902.

Hoppa, G., Greenberg, R., Geissler, P., Tufts, B.R., Plassmann, J., Durda, D, 1999b. Rotation of Europa: Constraints from Terminator and Limb Positions. Icarus 137, 341-347.

Hoppa, G.V., Tufts, B.R., Greenberg, R., Geissler, P, 1999c. Strike-slip faults on Europa: Global shear patterns driven by tidal stress. Icarus 141, 287-298.

Hoppa, G., Greenberg, R., Tufts, B.R., Geissler, P., Phillips, C., Milazzo, M., 2000. Distribution of strike-slip faults on Europa. J. Geophys. Res. 105, 22617-22627.

Hoppa, G.V., Tufts, B.R., Greenberg, R., Hurford, T.A., O'Brien, D.P., Geissler, P.E., 2001. Europa's rate of rotation derived from the tectonic sequence in the Astypalaea region, Icarus 153, 208-213.

Hurford, T.A., Sarid, A.R., Greenberg, R., 2007a. Cycloidal cracks on Europa: Improved modeling and non-synchronous rotation implications. Icarus 186, 218-233.

Hurford, T.A., Helfenstein, P., Hoppa, G.V., Greenberg, R., Bills, B.G., 2007b. Eruptions arising from tidally controlled periodic openings of rifts on Enceladus. Nature 447, 292-294.

Hurford, T.A., Sarid, A.R., Greenberg, R., Bills, B.G., 2009a. The Influence of Obliquity on Europan Cycloid Formation. Icarus 202, 197-215.

Hurford, T.A., Bills, B.G., Helfenstein, P., Greenberg, R., Hoppa, G.V., Hamilton, D.P., 2009b. Geological implications of a physical libration on Enceladus. Icarus 203, 541-552.

Hussman, H., Sohl, F., Spohn, T., 2006. Subsurface oceans and deep interiors of medium-sized outer planet satellites and large trans-neptunian objects. Icarus 185, 258-273.

Jacobs, D.A.H. (Ed.), 1977. The state of the art in numerical analysis. Academic Press, London.

Kattenhorn, S.A., 2002. Nonsynchronous rotation evidence and fracture history in the Bright Plains region, Europa. Icarus 157, 490-506.

Kattenhorn, S.A., 2004. Strike-slip fault evolution on Europa: evidence from tailcrack geometries. Icarus 172, 582-602.

Kattenhorn, S.A., and Hurford, T., 2009. Tectonics on Europa. In: R. Pappalardo, W. McKinnon, and K. Khurana (Eds.), Europa, Univ. Arizona Press, Tucson, pp. 199-236.

Kivelson, M.G., Khurana, K.K., Russell, C.T., Volwerk, M., Walker, R.J., Zimmer, C., 1981. Galileo magnetometer measurements: A stronger case for a subsurface ocean at Europa. Science 289, 1340-1343.

Lee, S., Pappalardo, R.T., and Makris, N.C., 2005. Mechanics of tidally driven fractures in Europa's ice shell. Icarus 177, 367-379.

Leith, A.C. and W.B. McKinnon, 1996. Is there evidence for polar wander on Europa. Icarus 120, 387-398.

Marshall, S.T. and S.A. Kattenhorn, 2005. A revised model for cycloid growth mechanics on Europa: Evidence from surface morphologies and geometries. Icarus 177, 341-366.

Margot, J.L., Peale, S.J., Jurgens, R.F., Slade, M.A., Holin, I.V., 2007. Large longitude libration of Mercury reveals a molten core. Science 316, 710-714.

Matsuyama, I. and F. Nimmo, 2008. Tectonic patterns on reoriented and despun planetary bodies. Icarus 195, 459-473.

McEwen, A.S., 1986 Tidal reorientation and the fracturing of Jupiter's moon Europa. Nature 321, 49-51.

McKinnon, W.B., 1999. Convective instability in Europa's floating ice shell. Geophys. Res. Lett. 26, 951-954.

Melosh, H.J., 1977. Global tectonics of a despun planet. Icarus 31, 221-243.

Melosh, H.J., 1980. Tectonic patterns on a tidally distorted planet. Icarus 43, 334-337.

Melosh, H.J. and A. Raefsky, 1980. The dynamical origin of subduction zone topography. Geophysical Journal of the Royal Astronomical Society 60, 333-354.

Meyer, J. and J. Wisdom, 2008. Tidal evolution of Mimas, Enceladus, and Dione. Icarus 193, 213-223.

Murray, C.D. and S.F. Dermott, 1999. Solar System Dynamics. Cambridge University Press, Cambridge.

Nimmo, F., 2004. Stresses generated in cooling viscoelastic ice shells: Application to Europa. J. Geophys. Res. – Planets 109, DOI: 10.1029/2004JE002347.

Nimmo, F. and E. Gaidos, 2002. Strike-slip motion and double ridge formation on Europa. J. Geophys. Res. 107, DOI: 10.1029/2000JE001476.

Nimmo, F. Spencer, J.R., Pappalardo, R.T., Mullen, M.E., 2007. Shear heating as the origin of the plumes and heat flux on Enceladus. Nature 447, 289-291.

Ojakangas, G.W. and D.J. Stevenson, 1989a. Thermal state of an ice shell on Europa. Icarus 81, 220-241.

Ojakangas, G.W. and D.J. Stevenson, 1989b. Polar wander of an ice shell on Europa. Icarus 81, 242-270.

Patterson, G.W., Head, J.W., Pappalardo, R.T., 2006. Plate motion on Europa and nonrigid behavior of the Icy lithosphere: The Castalia Macula region. Journal of

Structural Geology 28, 2237-2258.

Peale, S.J., 1999. Origin and evolution of the natural satellites. Annu. Rev. Astro. Astrophys. 37, 533-602.

Porco, C. and 24 colleagues, 2006. Cassini Observes the Active South Pole of Enceladus. Science 311, 1393-1401.

Preblich, B., Greenberg, R., Riley, J., O'Brien, D., 2007. Tidally driven strike-slip displacement on Europa: Viscoelastic modeling. Planetary and Space Science 55, 1225-1245.

Rambaux, N., Castillo-Rogez, J.C., Williams, J.G., Karatekin, O., 2010. Geophys. Res. Lett. 37, L04202.

Rhoden, A.R., Militzer, B., Huff, E.M., Hurford, T.A., Manga, M., Richards, M., 2010. Constraints on Europa's rotational dynamics from modeling of tidally-driven fractures. Icarus 210, 770-784.

Rhoden, A.R., Hurford, T.A., Manga, M., 2011a. Strike-slip fault patterns on Europa: Obliquity or polar wander? Icarus 211, 636-647.

Rhoden, A.R., Wurman, G., Huff, E.M., Manga, M., Hurford, T.A., 2011b. Shell tectonics: a mechanical model for strike-slip displacement on Europa. Icarus, in review.

Riley, J., Hoppa, G.V, Greenberg, R., Tufts, B.R., Geissler, P., 2006. Distribution of chaotic terrain on Europa. J. Geophys. Res. – Planets 105, 22599-22615.

Roberts, J.H. and F. Nimmo, 2008a. Near-surface heating on Enceladus and the south polar thermal anomaly. Geophys. Res. Lett. 35, L09201.

Roberts, J.H. and F. Nimmo, 2008b. Tidal heating and the long-term stability of a subsurface ocean on Enceladus. Icarus 194, 675-689.

Rudolph, M.L., and Manga, M., 2009. Fracture penetration in planetary ice shells. Icarus 199, 536-541.

Sarid, A.R., Greenberg, R., Hoppa, G.V., Hurford, T.A., Tufts, B.R., Geissler, P., 2002. Polar wander and surface convergence of Europa's ice shell: Evidence from a survey of strike-slip displacement. Icarus 158, 24-41.

Sarid, A.R., Hurford, T.A., and Greenberg, R., 2004. Branched Cusps Along Europan Cycloids. Bull. Am. Astron. Soc. 36, 184.

Sarid, A.R., Greenberg, R., Hoppa, G.V., Geissler, P., Preblich, B., 2004. Crack azimuths on Europa: time sequence in the southern leading face. Icarus 168, 144-157.

Sarid, A.R., Greenberg, R., Hoppa, G.V., Brown, D.M. Jr., Geissler, P., 2005. Crack azimuths on Europa: the G1 lineament sequence revisited. Icarus 173, 469-479.

Sarid, A.R., Greenberg, R., Hurford, T.A., 2006. Crack azimuths on Europa: Sequencing of the northern leading hemisphere. J. Geophys. Res. 111, E08004, doi:10.1029/2005JE002524.

Schenk, P. and W.B. McKinnon, 1989. Fault offsets and lateral crustal movement on Europa: Evidence for a mobile ice shell. Icarus 79, 75-100.

Schenk, P., Matsuyama, I., and Nimmo, F., 2008. True polar wander on Europa from global-scale small-circle depressions. Nature 453, 368-371.

Schulson, E.M., 2001. Brittle failure of ice. Engineering Fracture Mechanics 68, 1839-1887.

Sivia, D., and Skilling, J., 2006. Data Analysis: A Bayesian Tutorial. Oxford University Press, USA.

Smith-Konter, B. and Pappalardo, R.T., 2008. Tidally driven stress accumulation and shear failure of Enceladus' tiger stripes. Icarus 198, 435-451.

Spencer, J.R., Pearl, J.C., Segura, M., Flasar, F.M., Mamoutkine, A., Romain, P., Buratti, B.J., Hendrix, A.R., Spilker, L.J., Lopes, R.M.C., 2006. Science 311, 1401-1405.

Spencer, J.R., Barr, A.G., Esposito, L.W., Helfenstein, P., Ingersoll, A.P., Jaumann, R., McKay, C.P., Nimmo, F., Waite, J.H., 2009. Enceladus: An Active Cryovolcanic Satellite. In: *Saturn from Cassini-Huygens*, Springer.

Spencer, J.R., Howett, C., Pearl, J., Verbiscer, A., Hurford, T., Segura, M., 2010. EGU General Assembly 2010, 12207.

Spitale, J.N. and C.C. Porco, 2007. Association of the jets of Enceladus with the warmest regions on its south-polar fractures. Nature 449, 695-697.

Squyers, S.W., Reynolds, R.T., Cassen, P.M., and Peale, S.J., 1983. Liquid water and active resurfacing on Europa. Nature 301, 225-226.

Tobie, G., Choblet, G., Sotin, C., 2003. Tidally heated convection: Constraints on Europa's ice shell thickness. J. Geophys. Res. 108, doi: 10.1029/2003JE002099.

Tobie, G., Cadek, O., Sotin, C., 2008. Solid tidal friction above a liquid water reservoir as the origin of the south pole hotspot on Enceladus. Icarus 196, 642-652.

Tufts, B.R., Greenberg, R., Hoppa, G.V., Geissler, P., 1999. Astypalaea Linea: A San

Andreas-sized strike-slip fault on Europa. Icarus 141, 53-64.

Tyler, R.H., 2008. Strong ocean tidal flow and heating on moons of the outer planets. Nature 456, 770-772.

van Hoolst, T., Rambaux, N., Karatekin, O., Dehant, V., Rivoldini, A., 2008. The librations, shape, and ice shell of Europa. Icarus 195, 386-399.

Wahr, J., Selvans, Z.A., Mullen, M.E., Barr, A.C., Collins, G.C., Selvans, M.M., Pappalardo, R.T., 2009. Modeling stresses on satellites due to nonsynchronous rotation and orbital eccentricity using gravitational potential theory. Icarus, 200, 188-206.

Wisdom, J., 2004. Spin-Orbit Secondary Resonance Dynamics of Enceladus. Astron. J. 128, 484-491.

Yoder, C.F. 1979. How tidal heating in Io drives the Galilean orbital resonance locks. Nature 279, 767-770.